Controlling the quantum state of trapped ions

Dissertation

zur Erlangung des Doktorgrades an der
naturwissenschaftlichen Fakultät
der Leopold-Franzens-Universität Innsbruck

vorgelegt von

Christian Felix Roos

durchgeführt am Institut für Experimentalphysik
unter der Leitung von
o. Univ. Prof. Dr. R. Blatt

Innsbruck
Februar 2000

Abstract

This thesis reports on the setup of a new ion trap apparatus suitable for storing single or a few calcium ions. Calcium ions are trapped in a spherical Paul trap and cooled by laser light. By monitoring their fluorescence with a photo-multiplier tube and a CCD camera, the ions' internal states are detected with high efficiency.

The aim of the experiments is to explore the feasibility of coherent control of an ion's quantum state as a first step towards realising simple quantum logic gates utilising a string of Ca ions. For this purpose, several requirements have to be met. Firstly, the ions have to be prepared in a pure quantum state. Secondly, manipulations of the internal and motional state have to be carried out coherently. Furthermore, an efficient method for state detection is required.

By using a single trapped ion, the necessary experimental techniques are investigated. For both quantum state preparation and manipulation, the narrow optical quadrupole transition connecting the $S_{1/2}$ ground state to the metastable $D_{5/2}$ state is employed.

The ion is prepared in a pure state of motion by cooling its motion to the lowest quantum state of the confining potential. The cooling is performed by a two-stage process. In the first step, Doppler cooling on a dipole transition is used to prepare the ion in the Lamb-Dicke regime. In a second cooling step, sideband cooling on the $S_{1/2} \leftrightarrow D_{5/2}$ quadrupole transition enables the transfer of the ion's motional state into the ground state with up to 99.9 % probability. Different aspects of the cooling process are investigated. In particular, a measurement of the length of time that the ion spends on average in the final state after switching off the cooling lasers (heating time) is made. In contrast to prior experiments, this time is found to be orders of magnitude longer than the time required to manipulate the ion's quantum state.

By coherently exciting the ion after preparing it in Fock states of motion, the coherence time is probed and found to be on the order of a millisecond, thus allowing the realisation of a few quantum gates. Coherence-limiting processes have been investigated, as well as first steps towards extending the experiments to the case of two trapped ions.

In addition to the experiments mentioned above, the possibility of performing cavity-QED experiments with trapped ions is explored. How to efficiently couple the quadrupole transition of a Ca ion to a mode of a high-finesse resonator is studied theoretically. A first experiment exhibited a number of technical problems which should be overcome with a better design. A new experiment is currently being set up.

Zusammenfassung

In der vorliegenden Arbeit wird über den Aufbau einer Ionenfalle berichtet, die dazu geeignet ist, ein einzelnes Kalzium-Ion, bzw. wenige Kalzium-Ionen, zu speichern. Diese werden in einer sphärischen Paul-Falle gefangen und durch Laserstrahlung gekühlt. Die internen Zustände der Ionen können mit hoher Effizienz detektiert werden, indem man ihre Fluoreszenz mit einem Photomultiplier und einer CCD-Kamera nachweist.

Ziel der Arbeit ist es zu untersuchen, wie gut sich der Quantenzustand eines Ions unter Erhaltung seiner Kohärenz kontrolliert verändern läßt, in Hinblick auf Experimente, bei denen einfache quantenlogische Gatter mittels einer Kette von Kalzium-Ionen implementiert werden. Dazu müssen eine Reihe von Voraussetzungen erfüllt sein: Es ist erforderlich, die Ionen in einem quantenmechanisch reinen Zustand zu präparieren. Weiterhin muß es möglich sein, den internen wie auch den Bewegungszustand der Ionen kohärent verändern zu können. Außerdem wird eine effiziente Methode der Zustandsdetektion benötigt.

Die erforderlichen experimentellen Techniken werden in Experimenten an einem einzelnen gespeicherten Ion getestet. Der den $S_{1/2}$ - Grundzustand mit dem metastabilen $D_{5/2}$ - Zustand verbindende schmalbandige, optische Quadrupol-Übergang wird sowohl für die Quanten-Zustandspräparation als auch für die Manipulation des Zustandes verwendet.

Das Ion wird in einem reinen Zustand der Bewegung präpariert, indem man es mittels Laserkühlung in den untersten Quantenzustand des Fallenpotentials bringt. Die Kühlung erfolgt in einem zweistufigen Prozeß. In ersten Schritt wird das Ion durch Doppler-Kühlung auf einem Dipol-Übergang in den Bereich des Lamb-Dicke Regimes gekühlt. In einem zweiten Schritt ist es dann möglich, mittels Seitenband-Kühlung auf dem $S_{1/2} \leftrightarrow D_{5/2}$ - Übergang den Bewegungszustand des Ions mit einer Wahrscheinlichkeit von bis zu 99,9 % in den Grundzustand zu überführen. Verschiedene Aspekte des Kühlungsprozesses werden untersucht. Insbesondere wird die mittlere Zeitdauer bestimmt, die das Ion nach Ausschalten der Laserkühlung im niedrigsten Fallenzustand verweilt. Es stellt sich heraus, daß – im Gegensatz zu früheren Experimenten – diese Aufheiz-Zeit um Größenordnungen kleiner ist als die zur kohärenten Manipulation des Quantenzustandes des Ions erforderliche Zeit.

Indem man das Ion in Bewegungs-Fockzuständen präpariert und anschließend kohärent anregt, kann man die Kohärenzzeit untersuchen. Die nachgewiesene Kohärenzzeit von etwa einer Millisekunde ist hinreichend lang, um einige Quantengatter verwirklichen zu können. Prozesse, die die Kohärenzzeit begrenzen, werden untersucht. Zudem werden erste Schritte unternommen, um die Experimente von einem auf zwei Ionen auszudehnen.

Zusätzlich zu den oben beschriebenen Experimenten wird die Möglichkeit abgeschätzt, Experimente im Bereich der Hohlraum-Quantenelektrodynamik (cavity-QED) mit gespeicherten Ionen durchzuführen. Dazu wird theoretisch untersucht, wie man den Quadrupol-Übergang eines Kalzium-Ions effizient an eine Mode eines Hochfinesse-Resonators ankoppelt. Ein erstes Experiment zeigte eine Reihe von technischen Schwierigkeiten auf, die sich aber durch einen verbesserten Aufbau überwinden lassen sollten. Ein neues Experiment befindet sich derzeit im Aufbau.

Contents

1. Introduction

Simple systems have always been employed to elucidate the properties of physical theories. This applies especially to quantum theory where the discussion of thought experiments led to a deeper comprehension of the underlying theory [1], although the imagined experiments were far from being realisable at that time. Despite their conceptual simplicity, the difficulty of experimentally implementing these quantum-mechanical models originates from several reasons, all related to the microscopic size of the objects to be investigated: Firstly, measuring with high efficiency a quantum state, e. g. of an atom or of an electro-magnetic field mode, is a formidable task. Secondly, preparing and manipulating the quantum state requires even more sophisticated tools. In addition, the quantum state of the system has to be protected from uncontrolled interaction with its environment which would lead to an irretrievable loss of coherence.

Only in recent years has it become possible to realise experimentally close approximations to the highly idealised systems envisioned in textbooks of quantum mechanics. Examples include the preparation and measurement of quantum states of the electro-magnetic field [2, 3], and the control of the quantum state of atoms [4], and simple solid state systems [5]. These experiments may be viewed as tentative steps towards the emerging field of *quantum state control and engineering* [6].

Special attention has been devoted to the experimental realisation and study of entangled quantum states similar to the famous EPR state already discussed by Einstein, Podolsky, Rosen and Bohr in 1935 [7, 8]. In an entangled state of a composite quantum system, the state of one sub-system is inextricably interlinked with the state of another sub-system. Even though the composite system can be in a definite quantum state, neither of its parts are when examined individually[1]. The requirements for generating such states in an experiment are very stringent. Entangled states are even more sensitive to coupling to their environment. However, one can take advantage of this property by using them to study decoherence.

So far, entangled states of particles have been created only in a few experiments: Entangled pairs of photons were generated by down-conversion of photons [9] in non-linear crystals. Two [10] and four ions [11] trapped in a Paul trap were entangled via their Coulomb interaction and additional laser pulses. Rydberg atoms were placed in an entangled state via interaction with a microwave resonator [12]. Besides decoherence studies [13–15], the scope of entanglement-generating experiments includes tests of quantum mechanics [16–18] and spectroscopic measurements aiming at the ultimate limit of precision [19, 20], which could lead to improved frequency standards.

Parallel to these experiments, the subject of *quantum computation* emerged out of classical

[1] i. e., it is not possible to represent the quantum state of the whole system as a tensor product of states of the sub-systems.

information theory and quantum physics (for a review, see [21]). In a *quantum computer*, information is stored in a register consisting of a number of *qubits*, which are two-state systems such as two-level atoms or spin-$\frac{1}{2}$ particles. Information processing is performed by unitary transformations acting on the register. The power of quantum computation is due to the fact that – in contrast to a classical computer – the register of a quantum computer can be prepared in a superposition of states which are then processed in parallel. A number of algorithms have been discovered that allow for the solution of certain problems more efficiently by a quantum computer than by any classical computer. The factorisation of large numbers [22], and the search of unsorted data-bases [23] are probably the most well known examples. All of these algorithms are based on unitary transformations of the quantum register. The transformations can be decomposed into a sequence of single-qubit operations and simple building blocks (called *quantum gates*) which are unitary operations acting on different combinations of only a few qubits. It was found that there exist quantum gates enabling the generation of arbitrary unitary transformations in combination with single-qubit operations[2] [24–28].

The pre-requisites for an experimental realisation of a quantum computer are similar to those for quantum state engineering, because the generation of entangled states seems to be an essential feature of quantum computation (however, see [29, 30]). The state of a quantum computer has to be prevented from interacting with its environment, which would invariably lead to a decay of the pure quantum state into a statistical mixture of states, causing errors in the computation. Since no quantum system is completely isolated, it might appear that decoherence renders impossible the practical realisation of the concept of quantum computing. However, quantum error correcting codes have been devised that are capable of coping with a certain level of errors caused by decoherence [21].

It seems to be a reasonable approach to encode qubits in long-lived atomic states. In principle, photons could also be used, however, to store them and to make them interact with each other is more difficult. On the other hand, photons are naturally used in quantum communication [31] as carriers of quantum information. For *entanglement distribution*, schemes have been devised that exploit the complementary aspects of atoms and photons by mapping the state of an (atomic) qubit onto a photon wave-packet, thereby transmitting it to a distant place where the quantum information is again inscribed in an atomic state [32, 33].

Up to now, only a few quantum gates have been demonstrated experimentally. The external and internal degrees of freedom of an ion confined in an ion trap have been used to realise a two-bit gate [34]. In the context of cavity quantum electrodynamics, dispersive interactions between an atom and a mode of the electro-magnetic field have been used to generate quantum phase gates [35, 36]. Also, nuclear magnetic resonance (NMR) has been employed for a demonstration of a number of quantum gates[3].

Among the first proposals for the experimental realisation of a quantum computer was a

[2] These gates are called *universal*. For example, the *controlled-NOT gate* (a quantum version of the XOR gate) is a universal gate.

[3] NMR experiments differ from the experiments mentioned earlier in several respects. Because it is not possible to detect the state of single nuclear spins which are used as qubits, the experiments are performed on macroscopic samples and average spin states are measured, which amounts to doing many quantum computation experiments in parallel and averaging over the outcome. Because the macroscopic sample is in a thermal state, the quantum computer is not initialised in a pure state. Instead, *pseudo-pure states* [37, 38] are utilised which behave like pure states. Also, all states generated in NMR experiments so far are still separable [39, 40], i. e. there is no entanglement involved.

suggestion made by I. Cirac and P. Zoller [41]. They proposed to utilise ions confined in a linear ion trap [42] as an implementation of a quantum computer. In a linear ion trap, ions arrange themselves under the influence of the trapping potential and their mutual Coulomb repulsion in a linear chain with inter-ion distances of the order of several micrometers, the individual ions being localised on a sub-μm scale. The ions, each having two long-lived states $|g\rangle$ and $|e\rangle$ serve to encode the qubits. Single qubit operations are realised by manipulating the internal state of one of the ions by means of a tightly focussed laser beam. Due to the Coulomb interaction, one ion's motion in the trap is coupled to the motion of the other ions. The ion string exhibits normal modes of motion which are the equivalent of phonons in the case of a solid. Because the motional modes can be excited by a laser interacting with a particular ion, it is possible to entangle the internal state of that ion with a motional mode of the string. In the paper, Cirac and Zoller give a sequence of laser pulses that entangle the internal states of any two ions without affecting the final state of the motional modes. The main appeal of that scheme is its scalability. Contrary to the implementations of quantum computers mentioned above, there is no principle limit to the number of ions (qubits) to be used in the quantum register.
The proposal requires the ability to prepare at least one motional mode in its lowest quantum state, to coherently manipulate the ion's quantum states with a laser, and to address ions individually with a laser beam (i.e. to excite a particular ion without affecting the internal state of neighbouring ions). The first two conditions have first been met in experiments conducted in the group of D. Wineland [10, 43], and are easier to satisfy in strongly confining traps for reasons to be discussed in chapter 3, while, on the other hand, individual addressing of ions as demonstrated by the Innsbruck group [44] is less difficult to implement in weakly confining traps due to the increased inter-ion distances. The experiments in D. Wineland's group were performed with Be^+ ions, using two hyperfine states to implement a qubit and Raman transitions for state manipulation. Alternatively, a qubit can be implemented in an atom without hyperfine structure, using the atom's ground state and a long-lived metastable state. This is the approach adopted in this thesis.

Instead of mediating the ion–ion interaction via phononic excitation of a normal mode of the ion string, it can also be provided by a mode of the electro-magnetic field which is strongly coupled to the ions [45]. This would require the construction of an optical resonator with highly reflective mirrors around the ion string so that one of the resonator's modes could be coupled to an atomic transition. The same system, ion trap plus resonator, has also been suggested for the purpose of entanglement distribution as outlined above.

The subject of this work is to evaluate the feasibility of realising quantum gates following the Cirac–Zoller proposal. For this purpose, a spherical ion trap, suitable for storing single or few Ca^+ ions, has been set up. Cooling of one and two ions to the motional ground state has been studied as well as coherent manipulation of the ion's quantum state. In the comparable experiments [10, 43] conducted in D. Wineland's group, the coherence time for these manipulations was found to be limited by an unexpectedly strong heating of the motional modes, presumably owing to a coupling between the (charged) ions and noise voltages in the electrodes. Therefore, in the experiment described below, special attention was given to measurements of heating rates which turned out to be orders of magnitude smaller than in [10, 43].

So far, no working ion–cavity system exists in practice. The last part of this work is,

therefore, concerned with an investigation of the problems encountered when constructing a resonator around an ion trap.

The thesis is structured as follows: Chapters 2 and 3 are dedicated to the basic theoretical foundations necessary for the understanding of the experiments. In chapter 2, the function of the electrodynamic *Paul trap* used in the experiments is explained. Laser–ion interactions are described in chapter 3. Emphasis is given to the coherent interactions between trapped atoms and lasers, and to the cooling techniques relevant for the experiments. The last section of chapter 3 is devoted to the special case of trapped Ca^+ ions. An account of the experimental setup is given in chapter 4. Chapter 5 is concerned with the basic experimental techniques required for trapping ions, as well as exciting and detecting them. The main experimental results of the thesis are presented in chapter 6. First, spectroscopy of the $S_{1/2} \leftrightarrow D_{5/2}$ quadrupole transition is discussed, which is at the heart of all subsequent experiments. Then, Doppler cooling is investigated, followed by sideband cooling experiments that transfer a trapped ion into the lowest quantum state of motion. Heating rate measurements show that the ion constitutes a quantum system that is well isolated from its environment. Simple quantum state manipulation experiments are described as well as the first steps to extend the experiments to two ions. Chapter 7 deals with the issue of how to couple a transition between two internal states of an ion to the mode of a high-finesse resonator, and it describes an experimental setup that will eventually allow the increase of the spontaneous decay rate of a metastable atomic state. While improvements of the experimental setup are already discussed in chapters 6 and 7, the summary indicates future prospects of the experiment.

2. Paul traps

The Coulomb interaction between charged particles and electro-magnetic fields opens up the possibility to trap ions in a small region of space over long times. In 1953, Wolfgang Paul realized that ions could be mass-selected by means of radio-frequency (RF) fields [46]. A modification of his original experimental setup has become known as the *Paul trap* and allows the confinement of charged particles in three dimensions [47, 48]. Since then, Paul traps have found widespread use in mass spectrometry, but have also been used in atomic physics for studying the properties of single or few ions well isolated from their environment under ultra-high vacuum conditions [49].

The first section of this chapter explains the function of an ideal Paul trap. The following sections focus on issues associated with the special purpose of trapping single ions.

2.1. Principle of operation

In Paul traps, electric quadrupole potentials

$$\Phi(\mathbf{r}) = \Phi_0 \sum_i \alpha_i (r_i/\tilde{r})^2 \quad , \quad \text{i} = \text{x,y,z}$$

are used to confine charged particles at the centre of the potential. In a static potential, the point $\mathbf{r} = 0$ is an unstable fixed point because the Laplace equation $\Delta\Phi = 0$ requires at least one of the coefficients $\alpha_x, \alpha_y, \alpha_z$ to be negative. However, the position of equilibrium can be dynamically stabilised by making the potential Φ time dependent:

$$\Phi_0(t) = U + V\cos(\Omega_{RF} t) \; .$$

The equations of motion of a particle carrying a charge Q and having a mass m are then given by

$$\ddot{r}_i + \frac{2\alpha_i Q}{m\tilde{r}^2}\left(U + V\cos\left(\Omega_{RF} t\right)\right) r_i = 0 \tag{2.1}$$

and they take the canonical form of the Mathieu equation

$$\frac{d^2 u}{d\zeta^2} + \left(a - 2q\cos\left(2\zeta\right)\right) u = 0 \; , \tag{2.2}$$

with the substitutions

$$a_i = -\frac{8\alpha_i Q U}{m\tilde{r}^2 {\Omega_{RF}}^2} \tag{2.3}$$

$$q_i = \frac{4\alpha_i Q V}{m\tilde{r}^2 {\Omega_{RF}}^2} \tag{2.4}$$

and $\zeta = \frac{1}{2}\Omega_{RF}t$. Stable solutions of the Mathieu equation can be expressed as [50]

$$u(\zeta) = A\sum_{n\in\mathbb{Z}} C_{2n}\cos((2n+\beta)\zeta) + B\sum_{n\in\mathbb{Z}} C_{2n}\sin((2n+\beta)\zeta)\ ,$$

where the coefficients c_{2n} satisfy a certain recursion relation and β is a real number that depends on the values of a and q. Figure 2.1 shows the stability diagram of the Mathieu equation.

Stable trapping of charged particles is possible if the trajectories of the ions are bounded

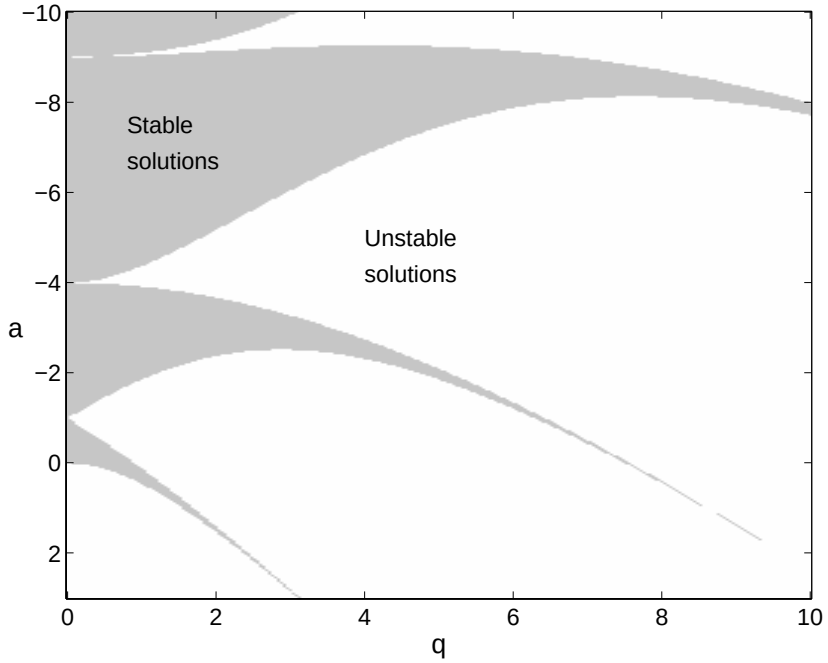

Figure 2.1.: Stability diagram of the Mathieu equation (2.2). Shaded areas indicate parameter values leading to stable solutions, corresponding to real values of β. For unstable solutions, β is purely imaginary.

in all directions. The region of stable trapping parameters is obtained by superimposing the stability diagrams for motion in all three directions. If the quadrupole potential is rotationally invariant about the z axis, the stability parameters a_i, q_i are given by

$$a_x = a_y = -\frac{8QU}{m({r_0}^2 + 2{z_0}^2){\Omega_{RF}}^2} \qquad a_z = -2a_x$$
$$q_x = q_y = \frac{4QV}{m({r_0}^2 + 2{z_0}^2){\Omega_{RF}}^2} \qquad q_z = -2q_x\ ,$$

where $\alpha_x = \alpha_y = 1, \alpha_z = -2$ and $\tilde{r}^2 = {r_0}^2 + 2{z_0}^2$. This choice ensures that $\Phi(r_0, 0, 0, t) - \Phi(0, 0, z, t) = U + V\cos(\Omega_{RF}t)$. Figure 2.2 shows a part of the stability diagram of a trap with rotational symmetry. In the limit that $a_i \ll q_i \ll 1$ solutions to the equations (2.1) exist

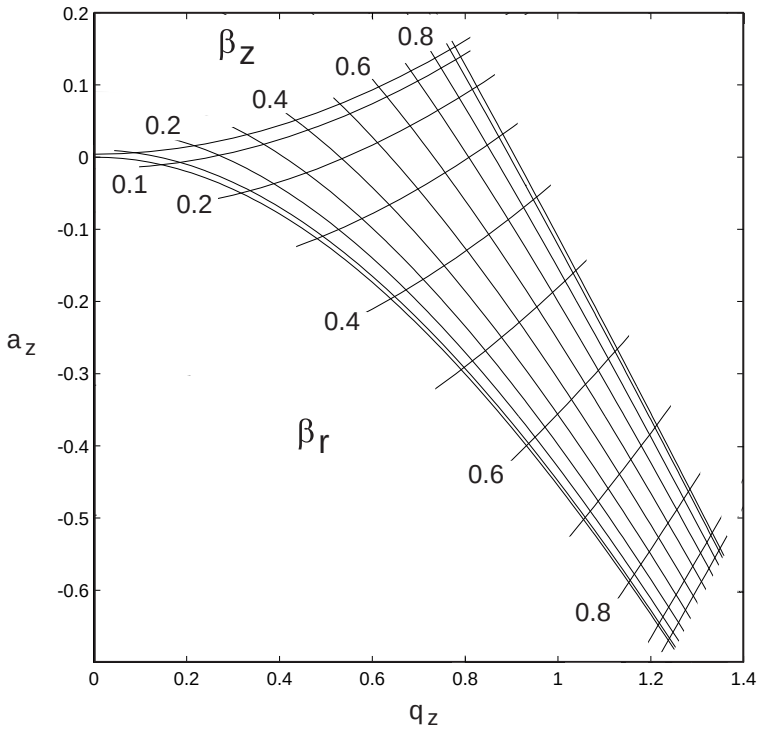

Figure 2.2.: The lowest stability zone in a Paul trap with rotational symmetry. The contour lines give the values of ω_r and ω_z in units of $\Omega_{RF}/2$.

and can be approximated by

$$r_i(t) = r_i^0 \cos(\omega_i t + \phi_i) \left(1 + \frac{q_i}{2} \cos(\Omega_{RF} t)\right) \ , \tag{2.5}$$

where ω_i is given by

$$\omega_i = \beta_i \frac{\Omega_{RF}}{2} \quad \text{and} \quad \beta_i = \sqrt{a_i + \frac{{q_i}^2}{2}} \ . \tag{2.6}$$

The motion of a confined particle can be decomposed into a harmonic motion with frequency ω_i called *secular motion*, and an amplitude modulated fast driven motion with frequency Ω_{RF} called *micromotion*. The amplitude of the micromotion is proportional to the distance of the ion from the centre of the trap. The *secular approximation* entails neglecting the micromotion and interpreting the secular motion as generated by a harmonic potential

$$Q\Psi = \tfrac{1}{2} \sum_i m_i {\omega_i}^2 {r_i}^2 \ , \ i \in \{x, y, z\} \ . \tag{2.7}$$

The potential Ψ is often called *pseudo-potential* in the literature in order to distinguish it from the generating potential Φ. Note that the oscillation frequency ω_i depends, via the factor β,

on the mass of the particle (see eq. (2.6)). The depth of the pseudopotential well in the radial and axial directions is given by

$$\bar{D}_i = \frac{m}{2}{\omega_i}^2{R_i}^2 \ ,$$

where R_i is the distance of the electrode from the centre of the trap. Well depths of a few eV are easily achieved. Therefore, it is possible to load the trap from a thermal beam of atoms[1] ionised inside the trap volume.

The kinetic energy of trapped ions can be reduced by laser cooling as will be explained in the next chapter. If their kinetic energy becomes comparable to $\hbar\omega$, the motion of the ion in the potential has to be quantised[2]. By defining the usual creation and annihilation operators

$$a_i{}^\dagger = \sqrt{\frac{m\omega_i}{2\hbar}}r_i + \frac{i}{\sqrt{2m\hbar\omega_i}}p_i \tag{2.8}$$

$$a_i = \sqrt{\frac{m\omega_i}{2\hbar}}r_i - \frac{i}{\sqrt{2m\hbar\omega_i}}p_i \ , \tag{2.9}$$

the Hamiltonian

$$H = \sum_i \frac{p_i^2}{2m} + \frac{1}{2}m{\omega_i}^2{r_i}^2$$

can be cast into the standard form

$$H = \sum_i \hbar\omega_i \left(a_i{}^\dagger a_i + \frac{1}{2} \right) \ .$$

The spread of the zero-point wave function is then given by $\langle 0|{r_i}^2|0\rangle^{1/2} = \sqrt{\hbar/2m\omega_i}$. For example, a $^{40}Ca^+$ ion cooled to the ground state of a trap with $\omega = (2\pi)\,1$ MHz is localised within 11 nm.

2.2. Single ion traps

Traps that are designed for trapping single ions differ from conventional Paul traps in certain respects. While the latter aim at generating pure quadrupole fields over large regions of space by means of hyperbolically shaped trap electrodes, single ion traps use open electrode structures that allow efficient collection of the weak fluorescence of the trapped ion. Field imperfections are of much less concern because the trajectory of the trapped ion is small compared with the length scale of the electrode structure. Multipole terms of higher order do not significantly modify the potential experienced by the ion. For example, an approximate quadrupole potential can be generated by the electrode configuration indicated in fig. 2.3.

Many single ion experiments require the trap frequencies to be quite high for several reasons (cf. chapter 3). Typically, trap frequencies are in the range of 500 kHz to 20 MHz. This can be

[1] The thermal energy (≈ 0.05 eV) of a Ca atom is small compared with the potential energy that the atom aquires at the moment of its ionisation in the trap.

[2] The quantisation can also be performed while maintaining the full time dependent potential $\Phi(t)$ [51, 52].

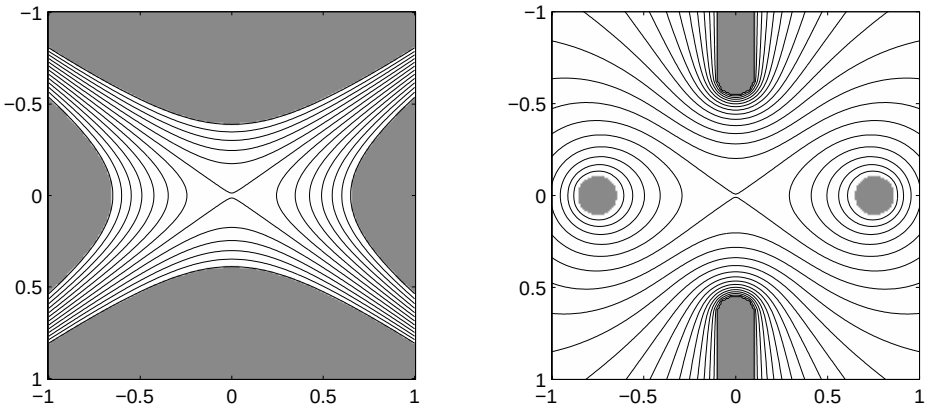

Figure 2.3.: Equipotential lines of a quadrupole potential (left plot) and an approximate quadrupole potential (right). Both potentials have a cylindrical symmetry. The horizontal axis corresponds to the radial direction, the vertical axis is the symmetry axis. The electrode structure shown in the right plot is the one used for the experiments if length is measured in millimeters. It is composed of a ring electrode and two cylindrical electrodes with hemispheric endcaps. For a three-dimensional representation of this electrode configuration, see figs. 4.2 and 4.4.

achieved by applying high voltages at radio-frequencies to small ion traps, as can be inferred from eqs. (2.4) and (2.6).

In practice, the ion is not trapped at the node of the RF-potential due to the presence of additional static electric fields that shift the ion out of the origin of the RF-potential. Those fields can arise from charges on isolators close to the trap or from potential variations on the electrode surfaces. They can be taken into account by adding an additional force term to the equations (2.1):

$$\ddot{r}_i + \frac{2\alpha_i Q}{m\tilde{r}^2}\left(U + V\cos\left(\Omega_{RF}t\right)\right) r_i = \frac{QE_i}{m} \tag{2.10}$$

Solutions to these equations are easily found in the pseudopotential approximation. They exhibit additional micromotion:

$$r_i(t) = \left(r_i^e + r_i^0\cos(\omega_i t + \phi_i)\right)\left(1 + \frac{q_i}{2}\cos(\Omega_{RF}t)\right) \ .$$

Static stray field of that kind can be compensated for by applying a suitable combination of voltages to a set of compensation electrodes. Another source of additional micromotion is phase differences in the RF-voltages at different trap electrodes, adding a dipole term to the potential. In this case, there is no point where the electric field vanishes at all times. However, all but one of the electrodes of the trap used for the experiments described in this thesis are grounded with respect to RF-voltages. Therefore, this source of micromotion can be neglected.

2.3. Compensation of micromotion

Many experiments performed with single ions are compromised by the presence of micromotion. That is why one tries to minimise its influence by moving the ion to the zero-point of the quadrupole field. The magnitude of stray electric fields usually changes slightly from day to day, so the micromotion has to be compensated every time the experiment is run.

This section describes a general strategy that can be employed to compensate stray electric fields in all three dimensions, if the micromotion amplitude of the ion along three non-collinear directions can be detected. The ion oscillates under the influence of the time dependent potential $\Phi(t)$ about an equilibrium position determined by the restoring force $\mathbf{F}_{pot} = A_{pot}\mathbf{r}$, $A_{pot} \in \mathbb{R}^3 \times \mathbb{R}^3$, the stray field force $\mathbf{F}_S$ and the additional force $\mathbf{F}_K$ exerted by the compensation voltages :

$$\mathbf{F}_{pot} + \mathbf{F}_S + \mathbf{F}_K = 0 \tag{2.11}$$

Under the additional assumptions that

1. the stray field $\mathbf{F}_S(\mathbf{r}) = \mathbf{F}_S$ is homogeneous over the trapping volume and
2. the compensation force $\mathbf{F}_K$ depends linearly on the compensation voltages $\mathbf{u} = (u_1, u_2, u_3)$ and is also position-independent, i.e. $\mathbf{F}_K(\mathbf{r}, \mathbf{u}) = B\mathbf{u}$, $B \in \mathbb{R}^3 \times \mathbb{R}^3$,

eq. (2.11) is transformed into

$$\mathbf{r} = -A_{pot}^{-1}\left(B\mathbf{u} + \mathbf{F}_S\right) \ . \tag{2.12}$$

The ion's velocity component $\mathbf{v}_0$ oscillating at the drive frequency Ω_{RF} is proportional to the electric quadrupole field (at the ion's position $\mathbf{r}$) which itself is a linear function of $\mathbf{r}$:

$$\mathbf{v}_0 \propto \mathbf{E}_{quad} = A_{quad}\mathbf{r} \ , \ A_{quad} \in \mathbb{R}^3 \times \mathbb{R}^3$$

Therefore, all points with no micromotion, i.e. no velocity component, in the direction $\boldsymbol{\lambda}$,$\boldsymbol{\lambda} \in \mathbb{R}^3$, lie in a plane

$$\boldsymbol{\lambda}^t\,\mathbf{v}_0 = 0 \iff \left(\boldsymbol{\lambda}^t\,A_{quad}\right)\mathbf{r} = 0 =: \mathbf{n}_\lambda^t\,\mathbf{r} \ , \tag{2.13}$$

where $\mathbf{n}_\lambda$ defines its normal vector. By multiplying eq. (2.12) with $\mathbf{n}_\lambda^t$, we get

$$0 = \mathbf{n}_\lambda^t\mathbf{r} = (\mathbf{n}_\lambda^t A_{pot}^{-1}B)\mathbf{u} + \mathbf{n}_\lambda^t A_{pot}^{-1}\mathbf{F}_S \ . \tag{2.14}$$

This equation defines a plane in the vector space of compensation voltages with normal vector $\hat{\mathbf{n}}_\lambda = B^t A_{pot}^{-1}\mathbf{n}_\lambda$. $\hat{\mathbf{n}}_\lambda$ does not depend on the stray fields which only displace the plane with respect to the origin. The compensation voltages that are necessary to shift the ion to the zero-point of the quadrupole field can now be uniquely determined by intersecting three planes corresponding to three non-collinear directions $\boldsymbol{\lambda}_{1,2,3}$.

After determining the normal vectors $\hat{\mathbf{n}}_{\lambda_1}, \hat{\mathbf{n}}_{\lambda_2}, \hat{\mathbf{n}}_{\lambda_3}$, it is sufficient to find a single point $\mathbf{u}^i$ on every plane in order to be able to compute the desired compensation voltages u_1, u_2, u_3 that shift the ion to the centre of the trap. Alternatively, this task can be accomplished by compensating the micromotion in the three directions iteratively. Knowledge of the normal

vectors $\hat{\mathbf{n}}_{\lambda_i}$ allows the choice of a procedure that converges rapidly. A number of methods have been devised to detect excess micromotion [53]. The presence of electric stray fields can be detected visually by monitoring the position of the ion with a CCD camera under changes of the trapping RF-field strength. Other methods detect micromotion by its influence on spectral lineshapes or by measuring correlation functions between the atomic velocity and the phase of the radiofrequency field (see section 5.3).

2.4. Ion crystals

Small numbers of ions trapped in a Paul trap form ordered structures, named *ion crystals*, when their kinetic energy becomes small compared to the Coulomb energy [54–56]. In that case, the ions undergo small oscillations around the equilibrium position and the Coulomb interaction can be linearised about this point. The equations, describing the motions of the ions in the x-, y- and z-directions, respectively, are still separable: the ions' motions are described by three sets of normal modes, corresponding to the three directions, which can be quantised in the same manner as the motional modes of a single trapped ion. A detailed treatment of this problem is given in [57]. Micromotion cannot be avoided in the case of ion crystals as the time varying potential vanishes only at the centre of the trap, but not at the equilibrium positions of the ions. *Linear traps* circumvent this problem by a suitable combination of ac and dc fields: The radial confinement is provided by a two-dimensional quadrupole field while a static field prevents the ions from escaping along the axial direction.

For the special case of a two-ion crystal, normal mode frequencies and equilibrium positions can be calculated analytically: The distance between the equilibrium positions of two singly charged ions of masses m_1 and m_2 is given by

$$d = |x_1^0 - x_2^0| = \left(\frac{e^2}{4\pi\epsilon_0}\right)^{\frac{1}{3}} \left(\frac{m_1\omega_{1x}{}^2 + m_2\omega_{2x}{}^2}{(m_1\omega_{1x}{}^2)(m_2\omega_{2x}{}^2)}\right)^{\frac{1}{3}} . \tag{2.15}$$

where ω_{nx} denotes the oscillation frequency of ion n along the weakest axis (x) of the trap. Let q_{ni}, $n = 1, 2$, be the displacement of the ion from its equilibrium position along the direction i, i=x,y,z. The potential energy can be written as $\Psi = \sum_i \Psi_i(q_i)$ with $q_i = (q_{1i}, q_{2i})$ and

$$\Psi_i(q) = \frac{1}{2}q^t \left\{ \begin{pmatrix} m_{1i}\omega_{1i}^2 & 0 \\ 0 & m_{2i}\omega_{2i}^2 \end{pmatrix} + \frac{e^2}{2\pi\epsilon_0|x_1^0 - x_2^0|^3} \begin{pmatrix} 1 & -1 \\ -1 & 1 \end{pmatrix} \right\} q =: \frac{1}{2}q^t A_i q \, .$$

The equations of motion then are

$$\ddot{q}_i + M^{-1}A_i q_i = 0 \quad \text{with} \quad M = \begin{pmatrix} m_1 & 0 \\ 0 & m_2 \end{pmatrix} \tag{2.16}$$

and the normal mode frequencies $\tilde{\omega}$ can be calculated from the eigenvalues of the matrices $M^{-1}A_i$

$$\{\tilde{\omega}_j\} = \left\{\lambda \geq 0 | \det(M^{-1}A_i - \lambda^2 I) = 0\right\} , \tag{2.17}$$

where I is the identity matrix. In the special case that $m_1 = m_2$ the normal mode frequencies are ω_x, ω_y, ω_z, $\sqrt{3}\omega_x$, $\sqrt{\omega_y{}^2 - \omega_x{}^2}$ and $\sqrt{\omega_z{}^2 - \omega_x{}^2}$.

3. Laser–ion interactions

In the experiments described in this thesis, lasers are used for several reasons. They are indispensable tools for detecting single trapped ions, cooling them, and manipulating and analyzing their quantum state.

The only practicable method to detect the presence of a single ion in a Paul trap is to detect its resonance fluorescence with a photomultiplier or a CCD camera. When the ion is strongly excited on a dipole transition, it scatters up to a few ten million photons per second. A count rate of 10 kHz can be easily achieved even if the overall detection efficiency is not much higher than 10^{-4}. Accordingly, the ion can be detected within a millisecond.

The high spectral density of laser light opens up the possibility to exert immense forces on single atoms that accelerate them by as much as 10^5 g. How to use these forces for the purpose of laser cooling is described in section 3.2, followed by a section focussing on the manipulation and analysis of the ion's quantum state. The last part is devoted to the special case of experiments with Ca^+ ions. First however, the basic interactions between a trapped ion and a laser are discussed.

3.1. Basic interactions

A harmonically trapped ion, interacting with the travelling wave of a single mode laser tuned close to a transition that forms an effective two-level system, is described by the Hamiltonian [58]

$$H = H_0 + H_1 \tag{3.1}$$

$$H_0 = \frac{p^2}{2m} + \tfrac{1}{2}m\omega^2 x^2 + \tfrac{1}{2}\hbar\nu\sigma_z \tag{3.2}$$

$$H_1 = \tfrac{1}{2}\hbar\Omega(\sigma^+ + \sigma^-)\left(e^{i(kx-\nu_L t+\phi)} + e^{-i(kx-\nu_L t+\phi)}\right) , \tag{3.3}$$

where σ_z, σ^+, σ^- are the Pauli spin matrices, k the wave number and ν_L is the frequency of the laser. The part H_0 of the Hamiltonian describes the state of the ion while the laser–ion interaction is contained in H_1, its strength being given by the coupling constant Ω. Here, it has been assumed that only a single transition (ν being the transition frequency) is close to resonance and that the laser is directed along the x-axis to the ion. The Pauli operators act on the internal atomic states, called $|S\rangle$ and $|D\rangle$. Defining the Lamb-Dicke parameter[1]

$$\eta = k\sqrt{\frac{\hbar}{2m\omega}} ,$$

[1] If the laser is at an angle ϕ to the oscillation axis, the definition has to be replaced by $\eta = k\cos\phi\sqrt{\hbar/2m\omega}$.

the laser–ion interaction can be expressed in terms of creation and annihilation operators as

$$H_0 = \hbar\omega(a^\dagger a + \tfrac{1}{2}) + \tfrac{1}{2}\hbar\nu\sigma_z \tag{3.4}$$

$$H_1 = \tfrac{1}{2}\hbar\Omega\left(e^{i\eta(a+a^\dagger)}\sigma^+ e^{-i\nu_L t} + e^{-i\eta(a+a^\dagger)}\sigma^- e^{i\nu_L t}\right) . \tag{3.5}$$

Here, the rotating wave approximation [59] has been made. In the interaction picture defined by $U = e^{iH_0 t/\hbar}$ the Hamiltonian $H_I = U^\dagger H U$ takes the form

$$H_I = \tfrac{1}{2}\hbar\Omega\left(e^{i\eta(\hat{a}+\hat{a}^\dagger)}\sigma^+ e^{-i\Delta t} + e^{-i\eta(\hat{a}+\hat{a}^\dagger)}\sigma^- e^{i\Delta t}\right) , \tag{3.6}$$

with $\hat{a} = ae^{i\omega t}$ and $\Delta = \nu_L - \nu$. The laser couples the state $|S,n\rangle$, where n is the vibrational quantum number, to all states $|D,n'\rangle$. This coupling is due to the oscillatory motion of the ion in the trapping potential. In the ion's rest frame, the laser is frequency-modulated with the trap frequency. Absorption or emission processes on a sideband of the electronic transition comply with the principle of energy conservation, because the energy difference $\hbar(\nu_L - \nu)$ can be transferred to the kinetic energy of the particle in the trap, thereby increasing or decreasing the vibrational quantum number. If the laser is tuned close to resonance of the $|S,n\rangle \leftrightarrow |D,n+m\rangle$ transition, that is $(\nu_L - \nu) \approx m\omega$, coupling to other levels can be neglected, provided the laser intensity is sufficiently low ($\Omega \ll \omega$). In that case, the laser induces a pairwise coupling between the levels $|S,n\rangle$ and $|D,n+m\rangle$. The time evolution of the state $\Psi(t) = \sum_n (c_n(t)|S,n\rangle + d_n(t)|D,n\rangle)$ is governed by the Schrödinger equation $i\hbar\partial_t\Psi = H\Psi$ which is equivalent to the set of coupled equations

$$\dot{c}_n = -i^{(1-|m|)}e^{i\delta t}\,(\Omega_{n+m,n}/2)\,d_{n+m} \tag{3.7}$$

$$\dot{d}_{n+m} = -i^{(1+|m|)}e^{-i\delta t}\,(\Omega_{n+m,n}/2)\,c_n . \tag{3.8}$$

$\delta = \Delta - m\omega$ accounts for a detuning of the laser from the transition, the constant

$$\Omega_{n+m,n} := \Omega\langle n+m|e^{i\eta(\hat{a}+\hat{a}^\dagger)}|n\rangle \tag{3.9}$$

is called Rabi frequency. Solutions to these equations show an oscillatory exchange of population between the coupled levels that can be interpreted as a sequence of stimulated absorption and emission processes. On resonance, this oscillation takes place with a frequency equal to the Rabi frequency:[2]

$$\begin{pmatrix} c_n(t) \\ d_{n+m}(t) \end{pmatrix} = \begin{pmatrix} \cos(\Omega_{n+m,n}t/2) & -ie^{i\frac{\pi}{2}|m|}\sin(\Omega_{n+m,n}t/2) \\ -ie^{-i\frac{\pi}{2}|m|}\sin(\Omega_{n+m,n}t/2) & \cos(\Omega_{n+m,n}t/2) \end{pmatrix} \begin{pmatrix} c_n(0) \\ d_{n+m}(0) \end{pmatrix} \tag{3.10}$$

When the laser is detuned from resonance, the population transfer is no longer complete, yet it takes place at a higher frequency:

$$\begin{pmatrix} c_n(t) \\ d_{n+m}(t) \end{pmatrix} = T_n \begin{pmatrix} c_n(0) \\ d_{n+m}(0) \end{pmatrix} ,$$

[2] Note that the definition of the coupling strength Ω given here differs from the definition used by the Boulder group (see for example [60]) by a factor of two : $\Omega = 2\Omega_{Boulder}$

where

$$T_n = \begin{pmatrix} e^{-i\frac{\delta}{2}t}\left(\cos(f_n^m t/2) + i\frac{\delta}{f_n^m}\sin(f_n^m t/2)\right) & -2i\frac{\Omega_{n+m,n}}{f_n^m}e^{i(-\frac{\delta}{2}t+\frac{\pi}{2}|m|)}\sin(f_n^m t/2) \\ -2i\frac{\Omega_{n+m,n}}{f_n^m}e^{-i(-\frac{\delta}{2}t+\frac{\pi}{2}|m|)}\sin(f_n^m t/2) & e^{i\frac{\delta}{2}t}\left(\cos(f_n^m t/2) - i\frac{\delta}{f_n^m}\sin(f_n^m t/2)\right) \end{pmatrix}$$

and $f_n^m = \sqrt{\delta^2 + \Omega_{n+m,n}^2}$ .The matrix element $\langle n+m|e^{i\eta(\hat{a}+\hat{a}^\dagger)}|n\rangle$ can be expressed as [61]

$$\langle n+m|e^{i\eta(\hat{a}+\hat{a}^\dagger)}|n\rangle = \exp(-\tfrac{\eta^2}{2})\eta^{|m|}L_n^{|m|}(\eta^2)\left(\frac{n!}{(n+m)!}\right)^{\mathrm{sign}(m)/2} , \tag{3.11}$$

using the associated Laguerre polynomial

$$L_n^\alpha(x) = \sum_{k=0}^{n}(-1)^k\binom{n+\alpha}{n-k}\frac{x^k}{k!} .$$

Transitions that change the number n of vibrational quanta by no more than one are most important for the experiments described in this thesis. They have been given special names in the literature: A spectral line is called *carrier*, if an absorption or emission does not change the motional state of the ion. A spectral line is termed *blue sideband*, if an absorption process is accompanied by an increase in the motional quantum number n while it is termed *red sideband*, if n decreases upon absorption. Likewise, the n*th* red or blue sideband refers to higher order processes. When the laser is tuned to a particular sideband (index m), the coupling strength can be efficiently calculated for a given value of the Lamb-Dicke parameter η by using the recursion relation [62]

$$\begin{aligned} L_0^m(x) &= 1,\ L_1^m(x) = m+1-x \\ L_{n+1}^m(x) &= \frac{1}{n+1}\left((2n+1+m-x)L_n^m - (n+m)L_{n-1}^m\right) \text{ for } n>1 . \end{aligned}$$

Fig. 3.1 shows the coupling strength on the carrier and the first and second blue sidebands for a value of $\eta = 0.05$.

3.1.1. Lamb-Dicke regime

The expression (3.11) considerably simplifies in the so-called Lamb-Dicke regime: The Lamb-Dicke parameter η relates the spatial extension of the lowest harmonic oscillator state to the wavelength of the atomic transition. In the Lamb-Dicke regime, defined by the condition $\eta^2(2n+1) \ll 1$, the atomic wavepacket is confined to a space much smaller than the wavelength of the transition. A Taylor expansion in eq. (3.11) is then possible,

$$\exp(i\eta(\hat{a}^\dagger + \hat{a})) = 1 + i\eta(\hat{a}^\dagger + \hat{a}) + \mathcal{O}(\eta^2) ,$$

and processes that change the vibrational quantum number n by more than one are strongly suppressed. Note that the Lamb-Dicke regime is always defined with respect to the wavelength of the transition involved. If it is mentioned without reference to any particular transition,

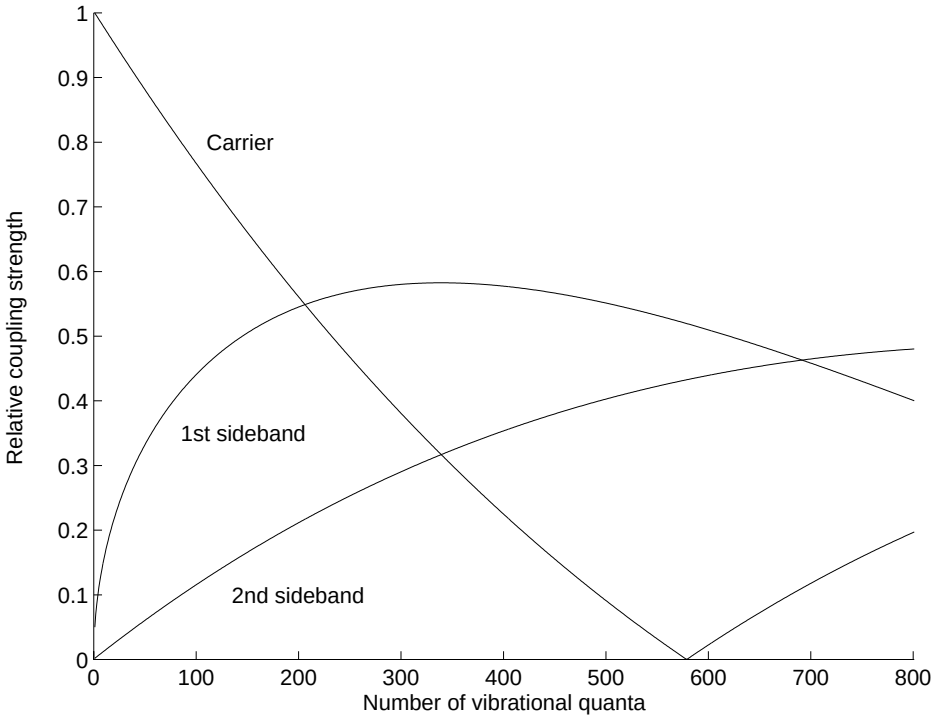

Figure 3.1.: Relative coupling strength on carrier and first and second sideband for $\eta = 0.05$.

it is assumed that the Lamb-Dicke criterion holds for all relevant transitions. Explicitly, the coupling strength on the carrier is well approximated by

$$\Omega_{n,n} = \Omega(1 - \eta^2 n) \,, \tag{3.12}$$

where Ω denotes the overall coupling strength. On resonance, the interaction Hamiltonian (3.6) reduces to

$$H_I = \tfrac{1}{2}\hbar\Omega_{n,n}(\sigma^+ + \sigma^-) \,.$$

Coupling to the red and blue sideband is considerably weaker, namely

$$\Omega_{n-1,n} = \eta\sqrt{n}\Omega \tag{3.13}$$

on the red sideband and

$$\Omega_{n+1,n} = \eta\sqrt{n+1}\Omega \tag{3.14}$$

on the blue sideband. On the red sideband, the Hamiltonian takes the shape

$$H_I = \tfrac{1}{2}i\hbar\Omega_{n-1,n}(\hat{a}\sigma^+ - \hat{a}^\dagger\sigma^-) \,. \tag{3.15}$$

This type of coupling is named *Jaynes-Cummings* (JC) Hamiltonian in the context of cavity QED, where it describes the interaction of a two-level atom with a quantised mode of the electro-magnetic field [63] (cf. chapter 7). On the blue sideband,

$$H_I = \tfrac{1}{2} i\hbar\Omega_{n+1,n}(\hat{a}^\dagger\sigma^+ - \hat{a}\sigma^-) \ .$$

This coupling is sometimes referred to as the anti-JC Hamiltonian. In the Lamb-Dicke regime, not only stimulated processes are unlikely to change the vibrational quantum number, but also spontaneous processes. This property is important in the context of sideband cooling. In order to satisfy the Lamb-Dicke criterion, the motion of the ion has to be cooled to a low-lying vibrational state.

3.1.2. Further remarks

Non-resonant interactions

So far, all non-resonant processes have been neglected, assuming that their coupling strength Ω_i is much smaller than the detuning. This condition is not always met in the experiments, especially in the Lamb-Dicke regime when the laser excites the transition on a sideband. In that case, coupling to the carrier has to be taken into account unless the coupling strength is very low. Coupling to the carrier changes the resonance frequency of the transition $|S,n\rangle \leftrightarrow |D,n\pm 1\rangle$ by [64]

$$\delta_S = -\frac{\Omega_{n,n}^2}{2\Delta} \ , \ \Delta = \nu_L - \nu \ , \tag{3.16}$$

if the condition $\Delta \gg \Omega$ does not hold strictly. This result is obtained by adiabatic elimination. Besides, there is always a small transfer of population to the non-resonantly coupled levels. If, for example, the transition $|S,0\rangle \leftrightarrow |D,1\rangle$ is driven with all the population initially in $|S,0\rangle$, then the populations of the levels $|D,0\rangle$ and $|S,1\rangle$ are proportional to the population of $|S,0\rangle$ and $|D,1\rangle$, respectively, with the proportionality factor given by $(\Omega_{n,n}/2\Delta)^2$ [59].

Generalizations of the model

Three-dimensional potential: For the sake of notational simplicity, the previous discussion was limited to the simple case of an ion confined in a one-dimensional harmonic potential. Generalization to the case of a three dimensional harmonic potential is straightforward and only amounts to replacing kx by the scalar product $\mathbf{k}\cdot\mathbf{r}$. The operator $\exp(i\eta(a^\dagger + a))$ is then replaced by $\exp(i\mathbf{k}\cdot\mathbf{r}) = \prod_m \exp(i\eta_m(a_m^\dagger + a_m))$, thereby allowing processes that change the quantum numbers of two or even all three oscillators simultaneously.

Two-ion crystal: A similar calculation can be done in the case of a two-ion crystal. In that case, the interaction Hamiltonian H_1 is given in the Schrödinger picture by

$$H_1 = \tfrac{1}{2}\sum_{i=1,2} \hbar\Omega_i\sigma_i^+ \exp\left(i\sum_m \eta_m^i(a_m^\dagger + a_m)\right)\exp(-i(\nu_L - \phi_i)t) + h.c. \ ,$$

where $a_m^\dagger$ and a_m are the creation and annihilation operators for the normal modes of oscillation labelled $1 \ldots m$. For the calculation of the Lamb-Dicke factors η_m^i, see [57]. Note that the phases ϕ_i and coupling strengths Ω_i for both ions are not necessarily equal.

Experimental realizations of the model

It is an experimental challenge to realise a good approximation to the model described above. The model assumes that the two-level atom interacting with the laser mode forms a system completely isolated from its environment, which is certainly an idealization. From an experimental point of view, the laser–atom coupling has to be made larger than any other coupling between the atom and its environment. Most importantly, the atomic levels should not couple strongly to other radiation modes of the electro-magnetic field, that is, the levels should be stable or metastable at least. This suggests using either stimulated Raman transitions coupling two hyperfine [60, 65] or Zeeman [66] ground states, or a quadrupole allowed transition coupling a metastable state to the electronic ground state. In the latter case, the induced electric-quadrupolar moment $\hat{Q}$ couples to the gradient of the electro-magnetic field:

$$H_I = \hat{Q} \nabla E(t)$$

This type of interaction takes the shape of eq. (3.3) when the Rabi frequency is defined as [57]

$$\Omega = \left| \frac{eE_0}{2\hbar} \langle S, m | (\boldsymbol{\epsilon} \cdot \mathbf{r})(\mathbf{k} \cdot \mathbf{r}) | D, m' \rangle \right| , \tag{3.17}$$

where E_0 is the electric field amplitude, $\mathbf{r}$ is the operator describing the position of the valence electron relative to the atomic centre of mass and m, m' indicate the magnetic quantum number. The dependence of the Rabi frequency on the polarization $\boldsymbol{\epsilon}$ and the wave vector $\mathbf{k}$ of the laser will be discussed in section 3.4.3. By using a quadrupole transition, the spontaneous decay rate of the excited state is reduced by a factor $f \approx (kQ/D)^2 \approx (kea_0{}^2/ea_0)^2 = (ka_0)^2$ compared with a dipole-allowed transition, a_0 being the Bohr radius. However, other mechanisms that destroy the coherence have also to be taken into account. For example, fluctuations of the laser phase, of the magnetic field and of the trap frequency [64] contribute to a loss of coherence. Therefore, the Rabi frequency has to be made larger than the overall decoherence rate. Since it is not easy to stabilise a laser to a linewidth below 1 kHz, a crude estimate assumes that the Rabi frequency should be on the order of at least 10 kHz if one aims at studying coherent phenomena. The coupling strength can be estimated to be

$$\Omega \approx \frac{kE_0}{2\hbar} ea_0{}^2 ,$$

thus requiring an electric field of $4000 V m^{-1}$ which can be generated by focussing a mere $20\,\mu W$ of light to a spot size of $(30\,\mu m)^2$. Note, however, that the power has to be increased by a factor of η^{-2} if the same Rabi frequency is to be achieved on the transition $|S, 0\rangle \leftrightarrow |D, 1\rangle$.

3.2. Laser cooling

Different methods have been developed to reduce the kinetic energy of trapped ions. The motion of the ions can be damped by coupling the trap electrodes to an electric circuit that

dissipates energy, by collisions with background gas atoms or by inelastic scattering of laser light. Out of these methods only laser cooling offers the prospect of cooling the ion into the quantum regime. Besides, it is flexible as it allows one to switch the interaction on and off at will. Laser cooling works by near-resonant excitation of an atomic transition. In the rest frame of the oscillating ion, the laser frequency appears frequency-modulated with the trap frequency. The strength of the sidebands depends on the amplitude of the ionic motion. Two limiting cases will be considered:

$\omega \ll \Gamma$**:** If the trap frequency ω is much lower than the decay rate Γ of the transition used for cooling, then the spacing of the sidebands is much smaller than the absorption width of the transition. The velocity of the ion due to the confining potential changes on a longer timescale than the time it takes the ion to absorb or emit a photon. So these processes can be assumed to change the momentum of the ion instantaneously. The ion behaves like a free particle seeing a time-dependent Doppler-shifted laser frequency. A velocity-dependent radiation pressure can provide cooling [67, 68], which has been termed *Doppler cooling*.

$\omega \gg \Gamma$**:** In the opposite case, the sidebands are resolved so that the laser can be tuned to a specific sideband. If the energy of the absorbed photons is smaller than the mean energy of spontaneously emitted photons, the kinetic energy of the ion shrinks.

The next two subsections explain the cooling mechanisms by means of simple models in case of a two-level atom. A more elaborate and mathematically stringent treatment of Doppler cooling can be found in [69].

The complementary aspects of both cooling techniques can be combined in a cooling scheme that allows the cooling of a thermal Ca^+ ion to the quantum mechanical ground state of the trapping potential.

3.2.1. Doppler cooling

Consider a two-level atom moving with velocity v interacting with a travelling wave laser field. The laser is characterised by its frequency ω_L and the Rabi frequency Ω, ω_0 denotes the atomic frequency and $\Delta = \omega_L - \omega_0$ the detuning of the laser. The laser exerts a radiation pressure force on the atom, given by

$$F = \hbar k \Gamma \rho_{ee} \,,$$

where the excited state probability is

$$\rho_{ee} = \frac{\Omega^2}{\Gamma^2 + 4\,(\Delta - kv)^2}$$

in the limit of low saturation. The radiation pressure force can be linearised around $v = 0$ if the velocity is already small :

$$F = F_0 + \left.\frac{dF}{dv}\right|_{v=0} v \,, \tag{3.18}$$

with

$$F_0 = \hbar k \Gamma \frac{\Omega^2}{\Gamma^2 + 4\Delta^2}$$

and

$$\left.\frac{dF}{dv}\right|_{v=0} = F_0 \frac{8k\Delta}{\Gamma^2 + 4\Delta^2} \, .$$

F_0 is the time-averaged radiation pressure which displaces the ion slightly from the centre of the trap. The velocity-dependent part of eq. (3.18) provides a viscous drag, if the detuning Δ is negative. The random nature of the absorption and emission processes counteracts this cooling force. The cooling rate is given by

$$\dot{E}_{cool} = \langle F v \rangle = \langle (F_0 + \left.\frac{dF}{dv}\right|_{v=0} v) v \rangle = \left.\frac{dF}{dv}\right|_{v=0} \langle v^2 \rangle \, .$$

Spontaneously emitted photons lead to a diffusive spreading of the mean squared momentum. Assuming uncorrelated spontaneous emission events, a heating rate results, given by

$$\dot{E}^{em}_{heat} = \frac{1}{2m}\frac{d}{dt}\langle p^2 \rangle = \frac{1}{2m}(\hbar k)^2 \Gamma \langle \rho_{ee}(v) \rangle \approx \frac{1}{2m}(\hbar k)^2 \Gamma \rho_{ee}(v=0) \, ,$$

provided that the atomic velocity is small. A second contribution to the heating rate, similar in size to $\dot{E}^{em}_{heat}$, results from the fluctuations of the cooling force due to the discreteness of the absorption process. In the steady state, the cooling rate $\dot{E}_{cool}$ equals the total heating rate $\dot{E}_{heat} = \dot{E}^{em}_{heat} + \dot{E}^{abs}_{heat}$ leading to

$$\dot{E}_{cool} + \dot{E}_{heat} = 0 \quad \Longleftrightarrow \quad \left.\frac{dF}{dv}\right|_{v=0} \langle v^2 \rangle = \frac{1}{m}(\hbar k)^2 \Gamma \rho_{ee}(v=0) \, .$$

Using the relation $m\langle v^2 \rangle = k_B T$ the cooling limit can be formulated as

$$k_B T = \frac{\hbar \Gamma}{4} \left(\frac{\Gamma}{-2\Delta} + \frac{-2\Delta}{\Gamma} \right) \, .$$

The lowest temperatures are obtained if $\Delta = -\frac{\Gamma}{2}$:

$$k_B T_{min} = \frac{\hbar \Gamma}{2} =: \frac{\hbar \Gamma}{4}(1+\alpha) \quad \text{with} \quad \alpha = 1 \, . \tag{3.19}$$

In the derivation it was assumed that the wave vector of spontaneously emitted photons points in or against the direction of the laser beam. If the photons are isotropically emitted into space, they cause heating in the transverse directions while the diffusive momentum spread in the cooled direction is proportionally smaller. The lower temperature can be accounted for by setting $\alpha = \frac{1}{3}$.[3] Cooling of the harmonic motion in all three oscillator directions $\mathbf{e}_i$ is accomplished by choosing a wave vector $\mathbf{k}$ that has a non-vanishing overlap with every

[3] More detailed calculations also consider the nature of the atomic transition. In case of a dipole radiation pattern, one obtains $\alpha = \frac{2}{5}$ [70].

direction $\mathbf{e}_i$.

Doppler cooling of atoms bears many similarities to Brownian motion and can in fact be cast into the form of a Fokker-Planck equation [69]. In the simple case described above, the atom performs a random walk in momentum space with a linear drift and a constant diffusion coefficient, which is known as an *Ornstein-Uhlenbeck* process in the literature [71]. In the stationary state, the momentum distribution has a Gaussian shape so that a thermal distribution results for the energy level occupation.

3.2.2. Sideband cooling

Sideband cooling on an atomic transition requires the trap frequency to be large compared to the laser linewidth and the decay rate of the excited state, allowing the laser to be tuned to the lower motional sideband of the transition. Then each excitation to the upper level is accompanied by a reduction in the vibrational quantum number. In the Lamb-Dicke regime, spontaneous decay does not affect the ion's motional state most of the time. So every cycle of absorption followed by spontaneous emission takes out a motional quantum until the ion reaches the ground state of motion that is decoupled from the laser excitation. Fig. 3.2 illustrates the basic process. Beyond the Lamb-Dicke regime spontaneous processes cause a

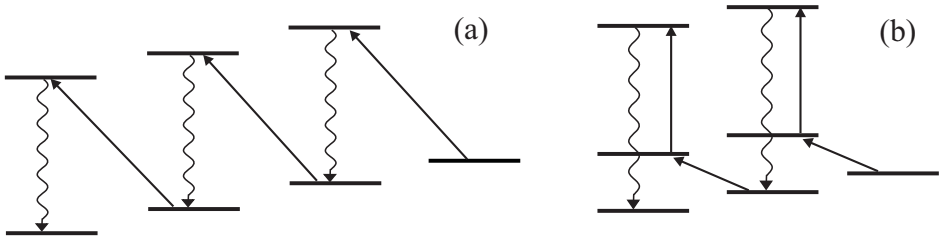

Figure 3.2.: Sideband cooling: (a) Each excitation to the upper state lowers the number of vibrational quanta by one while spontaneous emission does not change the motional state. (b) The lifetime of the upper level may be artificially shortened by coupling it to an auxiliary level that has a higher decay rate.

diffusion in the motional quantum number, thereby preventing the atoms to be efficiently cooled. Sideband cooling in this regime has been studied only theoretically so far [72]. In the following, it is assumed that the Lamb-Dicke criterion holds.

The cooling process has been described in great detail [70, 73, 74]. Here, a simple model is used to calculate two important parameters characterising the cooling: Ultimately, one seeks to achieve a ground state occupation p_0 as high as possible but also the cooling rate R is of concern. The cooling rate depends on the motional state and is given by the product of the decay rate of the excited level and its occupation probability:

$$R_n = \Gamma \frac{(\eta\sqrt{n}\Omega)^2}{2(\eta\sqrt{n}\Omega)^2 + \Gamma^2}$$

Non-resonant excitation from the $|n = 0\rangle$ state prevents the motional ground state from being a perfect 'dark state' and imposes a limit upon the minimum energy achievable. Fig. 3.3

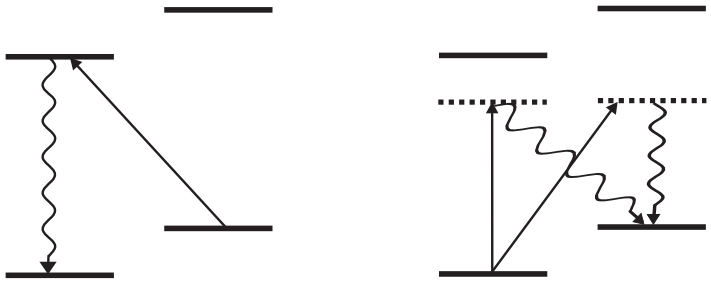

Figure 3.3.: (a) Cooling and (b) heating processes.

depicts the most prominent heating processes. The cooling limit can now be calculated under the assumption that $\langle n \rangle \ll 1$ and that the Rabi frequency is small compared to the decay rate. This allows one to adiabatically eliminate the excited electronic levels and to restrict the basis to the two lowest oscillator states. Calculating the steady state of the rate equations

$$\begin{aligned} \dot{p}_0 &= p_1 \frac{(\eta\Omega)^2}{\Gamma} - p_0 \left\{ \left(\frac{\Omega}{2\omega} \right)^2 \tilde{\eta}^2 \Gamma + \left(\frac{\eta\Omega}{4\omega} \right)^2 \Gamma \right\} \\ \dot{p}_1 &= -\dot{p}_0 \ , \end{aligned}$$

with p_0, $p_1 = 1 - p_0$ being the occupation probabilities for states $n = 0$ and $n = 1$ results in[4]

$$\langle n \rangle = p_1 = \frac{\Gamma^2}{4\omega^2} \left\{ \left(\frac{\tilde{\eta}}{\eta} \right)^2 + \frac{1}{4} \right\} \ . \tag{3.20}$$

In the resolved sideband limit, $\Gamma \ll \omega$, the particle is cooled to the zero-point energy of motion with high probability. The rate of the heating processes depends quadratically on the Rabi frequency while the cooling rate saturates as soon as $\eta\Omega$ becomes comparable to the decay rate Γ. This is why $\eta\Omega$ should not be chosen larger than Γ. Therefore, the magnitude of the decay rate Γ constrains the cooling rate maximally attainable. If the natural lifetime of the excited level is very long, it can be advantageous to shorten it by coupling the level to an auxiliary level having a shorter lifetime [75]. The effective linewidth is then given by [76]

$$\Gamma' = \frac{\Omega_{aux}^2}{(\Gamma_{aux} + \Gamma)^2 + 4\Delta_{aux}^2} \Gamma_{aux} \tag{3.21}$$

and is adjustable by appropriate setting of laser power and detuning Δ_{aux}.

Sideband cooling has been successfully applied to cool the motion of trapped Hg^+ [75] and Be^+ [65] ions[5]. In case of the Be^+ experiment a Raman transition was used for the cooling while the Hg^+ ion was cooled in a scheme similar to the one employed in the Ca^+ experiment described in the next chapter. In all these experiments, sideband cooling is preceded by a

[4] Two different Lamb-Dicke parameters $\eta, \tilde{\eta}$ enter into the final result. η is the Lamb-Dicke parameter for stimulated absorption processes to the excited state, while $\tilde{\eta}$ is related to the spontaneous emission process.

[5] Recently, sideband cooling has been also used to cool neutral atoms trapped in an optical lattice to the motional ground state [77–79].

Doppler cooling stage where the ions are quickly cooled on a dipole-allowed transition into the Lamb-Dicke regime. Sideband cooling on a dipole transition itself is difficult as it requires extremely tightly confining traps. Another possibility might be the use of intercombination lines for the purpose of sideband cooling [80].

3.3. Quantum state manipulation and analysis

This section gives a brief account of how the quantum state may be manipulated and how it can be analyzed. Central to the analysis is the electron shelving technique described below.

3.3.1. Electron shelving

The electron shelving technique allows one to discriminate between two electronic states with an efficiency close to 100%. In the level scheme shown in fig. 3.4 the ground state $|S\rangle$ is coupled to the metastable state $|D\rangle$ by a weak transition and to the state $|P\rangle$ by a strong transition. Since the weak transition is to be used for coherent manipulations, a method to measure the

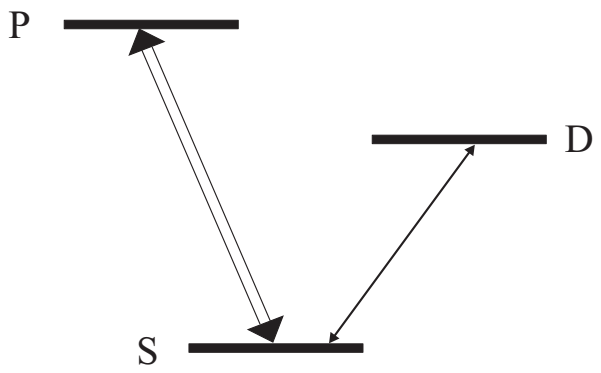

Figure 3.4.: Atomic levels relevant to electron shelving.

$|D\rangle$ state occupation is desired. This can be done by driving the strong transition with a laser, thereby projecting the atomic state either to the $|D\rangle$ state or its orthogonal subspace. No fluorescence is observed if the atom is in the $|D\rangle$ state, while in the opposite case, photons are scattered on the $|S\rangle \leftrightarrow |P\rangle$ transition. By repeatedly preparing an atomic state and measuring the fluorescence as described above, the $|D\rangle$ state occupation can be determined. Fig. 3.5 shows the resulting photon count distribution. The right peak corresponds to the ion being in the fluorescing state, the left one to the ion being in the 'dark' D state. Due to stray light the count rate is never zero. Both peaks have a Poissionian distribution. It is possible to discriminate between the S and the D level with an error rate as small as 0.1%. The state detection process is treated in more detail in appendix A.2.

3.3.2. Manipulation of the ion's quantum state

Sideband cooling allows the preparation of the ion in an almost pure motional state. Its internal degrees of freedom can be put into a well-defined state by optical pumping. Starting

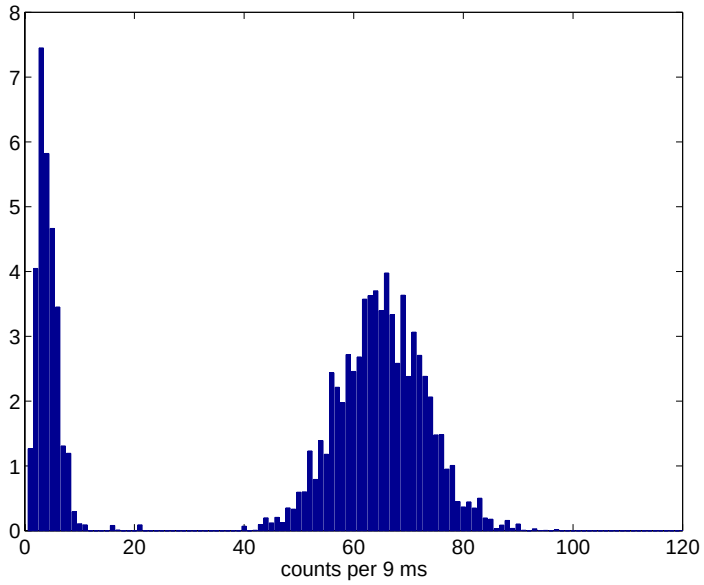

Figure 3.5.: Distribution of the count rate when the detection time is 9 ms. Count numbers smaller than 30 correspond to the ion being in the non-fluorescing state.

from this completely characterised state, the quantum state of the ion can be manipulated by coherently exciting it with a laser on a transition with resolved sidebands. The electronic state of the ion can be altered by tuning the laser to the carrier of the transition and applying a pulse of length T. For example, a pulse of length $T = (\pi/2)/\Omega$ – called $\pi/2$-pulse – transfers the ion to an equal superposition of the electronic ground state and the excited state if it was in the ground state initially. The motional state can be influenced by excitation on a sideband of the transition. For instance, a π-pulse on the blue sideband excites the ion from the ground state to the excited state and increases the vibrational quantum number by one. It has been shown that arbitrary states of motion may be generated by suitable sequences of pulses on the carrier and the sidebands [81].

3.3.3. Quantum state analysis

Electron shelving does not only permit one to monitor the electronic state of the ion. In combination with quantum state engineering techniques it allows for a complete analysis of the motional state [43]. Here, a number of simple methods are presented that characterise the motional state partially.

Determination of the distribution of motional states:

A population analysis of the motion states can be achieved by taking advantage of the motional state dependence of the Rabi frequency. The ion is supposed to initially be in the state $|S\rangle \otimes \rho$, where ρ is the density matrix characterising the motional state. If the blue sideband is driven for a time t prior to state detection, the measured $|D\rangle$ state occupation p_D depends on the

interaction time:

$$p_D(t) = \frac{1}{2}\left(1 - \sum_n \rho_{n,n} \cos(\Omega_{n+1,n} t)\right) \tag{3.22}$$

Then the diagonal elements of the density matrix can be computed by performing a Fourier transform or a singular value decomposition of the signal [60]. All elements of the density matrix including its phases can be determined by application of additional pulses [43].

Temperature measurements:

In many cases a detailed knowledge of the motional state is not required. To evaluate the quality of Doppler or sideband cooling, it suffices to measure the mean vibrational quantum number. Different methods exist for that purpose if the Lamb-Dicke criterion holds:

1. The motional ground state occupation can be measured by exciting the ion incoherently on the red sideband with saturating power and comparing the resulting $|D\rangle$ state population with similar experiments where the exciting laser is tuned to the blue sideband. Excitation on the blue sideband transfers half of the $|S\rangle$ state population to the $|D\rangle$ level, whereas with excitation on the red sideband, only half of the population that is *not* in the motional ground state is transferred. Therefore, the absorption strength p on the red and blue sidebands directly yields the ground state population [75]:

$$p_0 = 1 - \frac{p(\Delta = -\omega)}{p(\Delta = +\omega)} \tag{3.23}$$

   This method is useful only if the ion is in the ground state with substantial probability. Otherwise, the asymmetry in absorption strength is small, leading to a large uncertainty in the measured quantity.[6]

2. To evaluate the quality of Doppler cooling, measurement of the absorption strength on the carrier and the first sideband proves to be useful. In this case, the transitions should be incoherently excited without saturating the carrier. Then, the ratio of absorption probabilities is given by

$$\frac{p(\Delta = -\omega)}{p(\Delta = 0)} = \sum_n p_n \frac{(\eta\sqrt{n}\Omega)^2}{\Omega^2} = \eta^2 \bar{n} \,,$$

   where $\bar{n}$ is the mean vibrational quantum number. The Lamb-Dicke parameter is either calculated, or determined experimentally by measuring the Rabi frequencies on the carrier and the first sideband.

3. Yet another method takes advantage of the fact that the carrier Rabi frequencies weakly depend on the motional state. Coherent excitation of the carrier with a pulse of length

[6] The formula also applies, in case of coherent excitation, if the population is thermally distributed among the motional states.

t leads to damped Rabi oscillations:

$$p_D(t) = \frac{1}{2}\left\{1 - \sum_n \rho_{n,n}\cos(\Omega(1-\eta^2 n)t)\right\} \tag{3.24}$$

The loss of contrast is related to the mean vibrational quantum number. A short calculation (see appendix A.1) shows that for a thermal state $p_D(t)$ is well approximated by

$$p_D(t) \approx \frac{1}{2}\left\{1 - \frac{\cos(2\Omega t) + 2\Omega t\eta^2(\bar{n}+1)\sin(2\Omega t)}{1+(2\Omega t\eta^2(\bar{n}+1))^2}\right\} . \tag{3.25}$$

The last two methods are useful for checking whether the theoretical cooling limit is approached after Doppler cooling.

3.4. Sideband cooling and quantum state manipulation of Ca^+ ions

3.4.1. Level scheme of Ca^+

Calcium has proved to be an element suitable for ion trapping. Calcium has six stable isotopes with mass numbers ranging between 40 u and 48 u, the most abundant being ^{40}Ca. In nature, 97% of Calcium consists of ^{40}Ca. The nuclear spin of all Calcium isotopes is zero with the exception of ^{43}Ca which has a nuclear spin of $I = 7/2$. The singly charged Ca^+ ion has a hydrogen-like level structure. Its electronic configuration is similar to Argon with an additional valence electron. The five lowest energy levels are shown in fig. 3.6. All of the relevant transitions are accessible by solid state laser sources. The most prominent features of

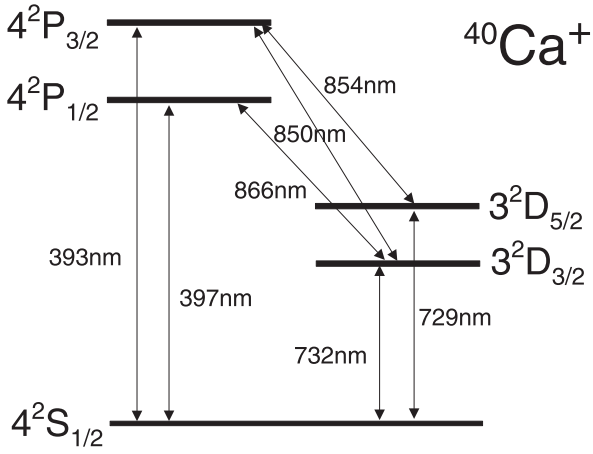

Figure 3.6.: Level scheme of $^{40}Ca^+$.

the level scheme are the metastable D levels. One out of 15 decays of the P levels populates

the D levels. The $S_{1/2}$ level is connected to the $D_{3/2}$ and $D_{5/2}$ levels by electric-quadrupole transitions with transition rates of approximately $(2\pi)\,0.16\ s^{-1}$. Accordingly, the lifetime of the D levels is roughly 1 s [82]. Wavelengths and transition rates of the other transitions are listed in the following table.

Transition wavelengths and lifetimes of $^{40}Ca^+$ [57]

		$S_{1/2} \Leftrightarrow P_{1/2}$	$S_{1/2} \Leftrightarrow P_{3/2}$	$P_{1/2} \Leftrightarrow D_{3/2}$	$P_{3/2} \Leftrightarrow D_{3/2}$	$P_{3/2} \Leftrightarrow D_{5/2}$
τ_{nat}	ns	7.7(2)	7.4(3)	94.3	901	101
λ_{air}	nm	396.847	393.366	866.214	849.802	854.209

		$S_{1/2} \Leftrightarrow D_{5/2}$	$S_{1/2} \Leftrightarrow D_{3/2}$
τ_{nat}	s	1.045	1.080
λ_{air}	nm	729.147	732.389

Two other quantities of interest are the Landé factors g_J that determine the energy splitting of the Zeeman levels in a magnetic field and the branching ratios of the P levels which are important for Doppler and sideband cooling.

Landé factors for relevant energy levels [83]

	$S_{1/2}$	$P_{1/2}$	$P_{3/2}$	$D_{3/2}$	$D_{5/2}$
g_J	2	2/3	4/3	4/5	6/5

Branching ratios of the P levels [84]

$\frac{P_{1/2}\rightarrow S_{1/2}}{P_{1/2}\rightarrow D_{3/2}}$	$\frac{P_{3/2}\rightarrow S_{1/2}}{P_{3/2}\rightarrow D_{3/2}}$	$\frac{P_{3/2}\rightarrow S_{1/2}}{P_{3/2}\rightarrow D_{5/2}}$
15.88	150.8	17.6

The experiments described in following chapters below are all done using the isotope $^{40}Ca^+$.

3.4.2. Cooling techniques

Doppler cooling

The $S_{1/2} \leftrightarrow P_{1/2}$, transition having a linewidth of 20 MHz, is suitable for Doppler cooling. Since the $P_{1/2}$ level decays with a probability of 6% to the metastable $D_{3/2}$ level, optical pumping has to be prevented by simultaneously exciting the $S_{1/2} \leftrightarrow P_{1/2}$ and $D_{3/2} \leftrightarrow P_{1/2}$ transitions (see fig. 3.7 a). The repumping laser needs to have a polarization component perpendicular to the quantization axis that is chosen by applying a small magnetic field of a few Gauss. For Doppler cooling, the frequency of the laser at 397 nm is red detuned by approximately $\Gamma/2 = 10$ MHz while the frequency of the repumping laser is kept on resonance. This prevents coherent population trapping in a superposition of the $S_{1/2}$ and $D_{3/2}$ level that is decoupled from interaction with the laser fields. Due to the favorable branching ratio, the ion is cooled on the $S_{1/2} \leftrightarrow P_{1/2}$ transition while the influence of the $D_{3/2} \leftrightarrow P_{1/2}$ transition is small. Therefore, the cooling limit is expected to be close to the Doppler cooling limit of a

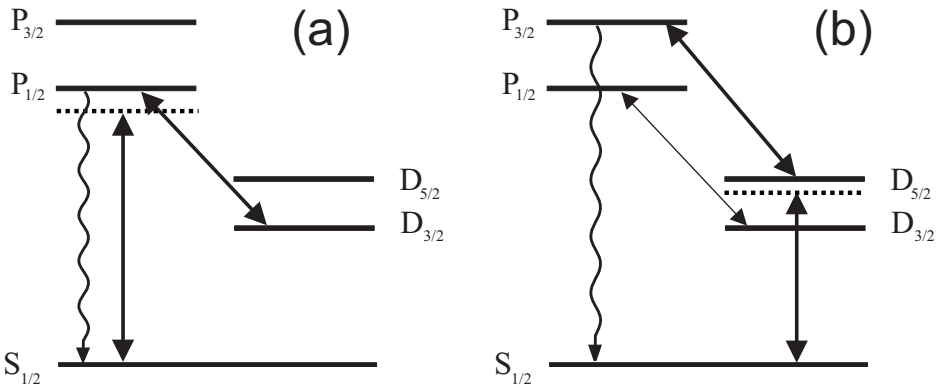

Figure 3.7.: a) Doppler cooling. b) Sideband cooling.

two-level atom, yielding a mean vibrational quantum number of $\bar{n} = 10$ for a trap frequency of 1 MHz. Then the Lamb-Dicke parameter is $\eta_{729} = 0.096$ on the $S_{1/2} \leftrightarrow D_{5/2}$ transition and $\eta_{393} = 0.179$ on the $S_{1/2} \leftrightarrow P_{3/2}$ transition. Hence the Lamb-Dicke criterion ${\eta_{393}}^2 \bar{n} = 0.32 < 1$ is approximately satisfied even on the transition with the shortest wavelength. On the other hand, an average of 2 motional quanta is expected at a trap frequency of 5 MHz. Clearly, a second cooling step is required to prepare the ion in a pure state of motion.

Sideband cooling

The $S_{1/2} \leftrightarrow D_{5/2}$ transition is used for sideband cooling. Since the natural lifetime of the $D_{5/2}$ level is approximately one second, the upper level has to be quenched by coupling it to the quickly decaying $P_{3/2}$ level in order to realise an acceptable cooling rate. The quadrupole transition splits in a non-zero magnetic field into ten different transitions. A good approximation to a three-level system can be realised by choosing the $S_{1/2}(m = -1/2) \leftrightarrow D_{5/2}(m = -5/2)$ transition for sideband cooling and coupling the upper level to the $P_{3/2}(m = -3/2)$ level. Again, the favourable branching ratio allows for a high number of cooling steps before the ion is lost from the cooling cycle. Pumping to other $D_{5/2}$ levels is prevented by the quenching laser. After a decay to the $D_{3/2}$ level, the laser at 866 nm recycles the ion to the $S_{1/2}$ level. Decay to the $S_{1/2}(m = +1/2)$ level can be counteracted by driving the $S_{1/2} \leftrightarrow P_{1/2}$ transition with σ^--polarised light. However, if the polarization is not perfectly circular, the laser also excites the ion from the $S_{1/2}(m = -1/2)$ level giving rise to two unwanted effects. Firstly, the S level is broadened by the coupling, thus eventually reducing the cooling rate. Secondly, sideband cooling is impeded by Doppler 'cooling' on the $S_{1/2} \leftrightarrow P_{1/2}$ transition. That means, that the ion is heated on the dipole transition if its energy is below the Doppler limit. In conclusion, the $S_{1/2}(m = +1/2)$ level should not be pumped out continuously, but by short pulses that scatter only a few photons. Fortunately, it turns out that this level is populated only after 80-160 cooling cycles, the exact number depending on the polarization of the quenching laser as can be seen in fig. 3.8. In the experiments, the cooling efficiency was found not to be affected by optical pumping to the wrong $S_{1/2}$ level. Therefore, only a single short pulse was applied after the sideband cooling stage.

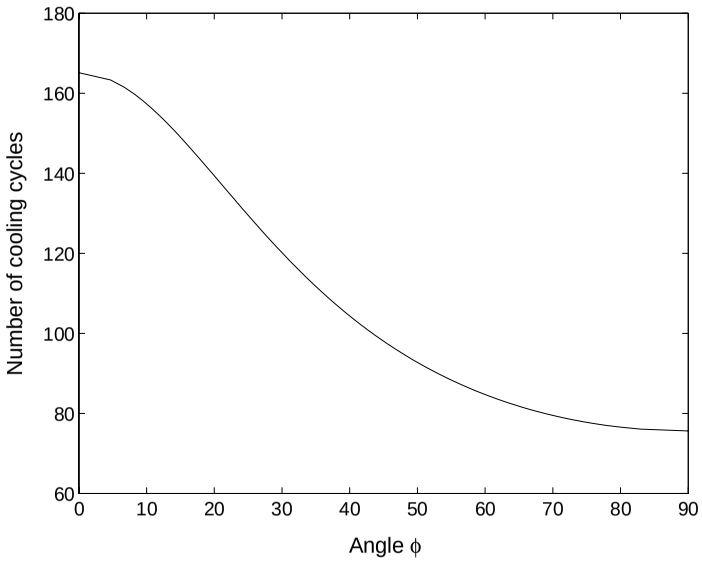

Figure 3.8.: Average number of cooling cycles before optical pumping to the $S_{1/2}(m = +1/2)$ level occurs versus polarization of the quenching laser. ϕ denotes the angle between the polarization and the component of the magnetic field that is perpendicular to the k-vector of the beam. Since the quenching laser needs to have a polarization component perpendicular to the magnetic field, the optimum situation cannot be exactly realised.

The $S_{1/2}(m = -1/2) \leftrightarrow D_{5/2}(m = -5/2)$ and $S_{1/2}(m = +1/2) \leftrightarrow D_{5/2}(m = +5/2)$ transitions are equally well suited for sideband cooling in all but one aspect. No other Zeeman transition has a lower frequency than the $S_{1/2}(m = -1/2) \leftrightarrow D_{5/2}(m = -5/2)$ transition. If its red sideband frequency coincides by chance with a sideband of another Zeeman transition, then excitation of the other transition also leads to a decrease in phonon number (disregarding higher order processes involving micromotional sidebands or sidebands of other oscillators). Those unwanted coincidences can be minimised by a proper choice of the magnetic field strength that shifts the energy levels by

$$\Delta E = g_j \mu_B B m_j \ ,$$

where μ_B is Bohr's magneton and g_j the Landé factor (cf. fig. 5.12). A field of 4 Gauss spreads the components of the $S_{1/2} \leftrightarrow D_{5/2}$ transitions over a range of approximately 30 MHz. Using much higher magnetic fields is not advisable since they also broaden the $S_{1/2} \leftrightarrow P_{1/2}$ Doppler cooling transition, thereby increasing the Doppler limit.

3.4.3. Coherent manipulations: Geometrical considerations

For coherent manipulations of the ion's quantum state any $S_{1/2} \leftrightarrow D_{5/2}$ Zeeman transition could be used. Since it is desirable to approximate the ideal two-level atom as closely as possible, the geometric dependence of the coupling strength Ω has to be considered. It is

possible to suppress excitation on some of the transitions by a proper choice of the polarization and the laser beam direction. According to ref. [57], eq. (3.17) can be written as

$$\begin{aligned}\Omega &= \left|\frac{eE_0}{2\hbar}\langle S_{1/2},m|(\boldsymbol{\epsilon}\cdot\mathbf{r})(\mathbf{k}\cdot\mathbf{r})|D_{5/2},m'\rangle\right| \\ &= \left|\frac{eE_0}{2\hbar}\langle S_{1/2}\|r^2\mathbf{C}^{(2)}\|D_{5/2}\rangle\sum_{q=-2}^{2}\begin{pmatrix}1/2 & 2 & 5/2\\ -m & q & m'\end{pmatrix}c_{ij}^{(q)}\epsilon_i n_j\right| ,\end{aligned} \tag{3.26}$$

where $\langle S_{1/2}\|r^2\mathbf{C}^{(2)}\|D_{5/2}\rangle$ is the reduced matix element and the terms in round brackets are 3-j symbols. The geometry-dependent part is contained in the quadratic form $g^{(q)} := c_{ij}^{(q)}\epsilon_i n_j$. The polarization and the wave vector can be parametrised by the angle ϕ between the laser beam and the magnetic field and by the variable γ describing the angle between the polarization and the magnetic field vector projected into the plane of incidence. Choosing $\mathbf{B} = B_0(0,0,1)$, one obtains $\boldsymbol{k} = k(\sin\phi, 0, \cos\phi)$,[7] $\boldsymbol{\epsilon} = (\cos\gamma\cos\phi, \sin\gamma, -\cos\gamma\sin\phi)$ and

$$\begin{aligned} g^{(0)} &= \tfrac{1}{2}\,|\cos\gamma\sin(2\phi)| \\ g^{(\pm1)} &= \tfrac{1}{\sqrt{6}}\,|\cos\gamma\cos(2\phi) + i\sin\gamma\cos\phi| \\ g^{(\pm2)} &= \tfrac{1}{\sqrt{6}}\left|\tfrac{1}{2}\cos\gamma\sin(2\phi) + i\sin\gamma\sin\phi\right| . \end{aligned}$$

Fig. 3.9 shows the coupling strength for the $\Delta m = 0, \pm1, \pm2$ transitions as a function of ϕ and γ. Two configurations are particularly useful:

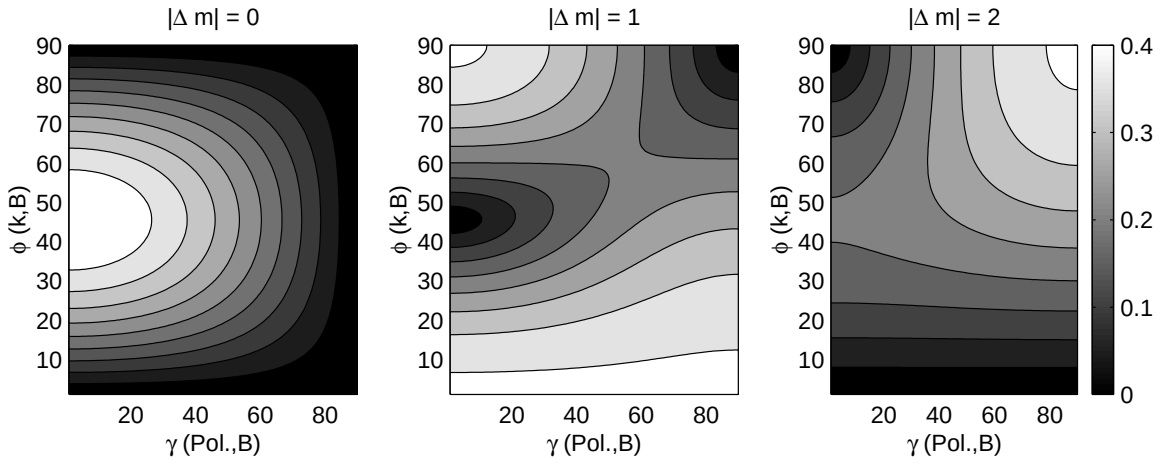

Figure 3.9.: Relative coupling strength on the $S_{1/2} \leftrightarrow D_{5/2}$ when $|\Delta m| = 0, 1, 2$. ϕ denotes the angle between the laser beam and the magnetic field, γ is the angle between the polarization and the magnetic field vector projected into the plane of incidence. Light shadings of grey indicate a high, dark shadings a low coupling strength.

[7] The y-component of $\boldsymbol{k}$ can be chosen to be zero due to cylindrical symmetry.

$\phi = 90°, \gamma = 90°$ If the polarization, the beam axis and the direction of magnetic field are mutually orthogonal, only the $\Delta m = \pm 2$ components are excited, thereby closely approximating the ideal situation of a two-level atom. The $S_{1/2}(m = -1/2) \leftrightarrow D_{5/2}(m = -5/2)$ transition would be used for sideband cooling and also for quantum state engineering.

$\phi = 45°, \gamma = 0°$ In this configuration, the $\Delta m = 0$ transitions are excited most strongly while the $\Delta m = \pm 1$ transitions do not couple to the laser. Again, for sideband cooling, the $S_{1/2}(m = -1/2) \leftrightarrow D_{5/2}(m = -5/2)$ transition would be used while state engineering would be done on the $S_{1/2}(m = -1/2) \leftrightarrow D_{5/2}(m = -1/2)$ transition.

The first configuration has the disadvantage that quantum state engineering is done on a transition that depends strongly on the magnetic field. Small fluctuating magnetic fields shift the resonance frequency randomly, thus contributing to decoherence. This effect is five times weaker on the $S_{1/2}(m = -1/2) \leftrightarrow D_{5/2}(m = -1/2)$ transition. Here, a field fluctuation of $\Delta B = 1$ mG changes the resonance frequency by only 550 Hz. However, the spectrum of the $S_{1/2} \leftrightarrow D_{5/2}$ transition has a more complicated structure in the second case. Furthermore, a higher intensity of the cooling laser is required to achieve the same cooling rate as in the first case. Fig. 3.10 shows the relative line strength ($\propto \Omega^2$) of the transitions for the cases described above. The reduced matrix element $\langle S_{1/2} \| r^2 \mathbf{C}^{(2)} \| D_{5/2} \rangle$ is related to the decay rate of the excited state by [57]

$$A = \frac{c\alpha k^5}{15(2j'+1)} \left| \langle S_{1/2} \| r^2 \mathbf{C}^{(2)} \| D_{5/2} \rangle \right|^2 , \tag{3.27}$$

where α is the fine structure constant. Inserting this equation into eq. (3.26) allows one to calculate the Rabi frequency as a function of the electric field. One obtains on the $S_{1/2}(m = -1/2) \leftrightarrow D_{5/2}(m = -5/2)$ transition

$$\Omega = \frac{eE}{\hbar} \sqrt{\frac{5\lambda^3 A}{64\pi^3 c\alpha}}$$

for optimal coupling. This formula can now be used in a numerical example to evaluate the feasibility of sideband cooling on the quadrupole transition: An electric field E=$2.3 \cdot 10^5 V/m$ generated by focussing 100 mW of light in a Gaussian beam to a spot with a waist $w_0 = 30\,\mu m^2$ yields a Rabi frequency $\Omega = (2\pi)\,1.2$ MHz on the carrier of the cooling transition. If the Lamb-Dicke factor was $\eta = 0.05$, the Rabi frequency on the red sideband would be $\Omega_{n,n-1} = (2\pi)$ 60 kHz$\sqrt{n}$ and the ion could be cooled from the Doppler limit to the ground state in less than a millisecond. This example shows that sideband cooling on a quadrupole transition does not necessitate long cooling times.

3.4.4. Pulsed spectroscopy on the $S_{1/2} \leftrightarrow D_{5/2}$ transition

All spectroscopic investigations of the $S_{1/2} \leftrightarrow D_{5/2}$ transition are done in a pulsed scheme consisting of the following steps:

1. **Doppler cooling.** The ion is pumped to the electronic ground state and precooled on the $S_{1/2} \leftrightarrow P_{1/2}$ dipole transition to a mean vibrational quantum number between 2 and 10. After cooling it is prepared in the $S_{1/2}(m = -1/2)$ level.

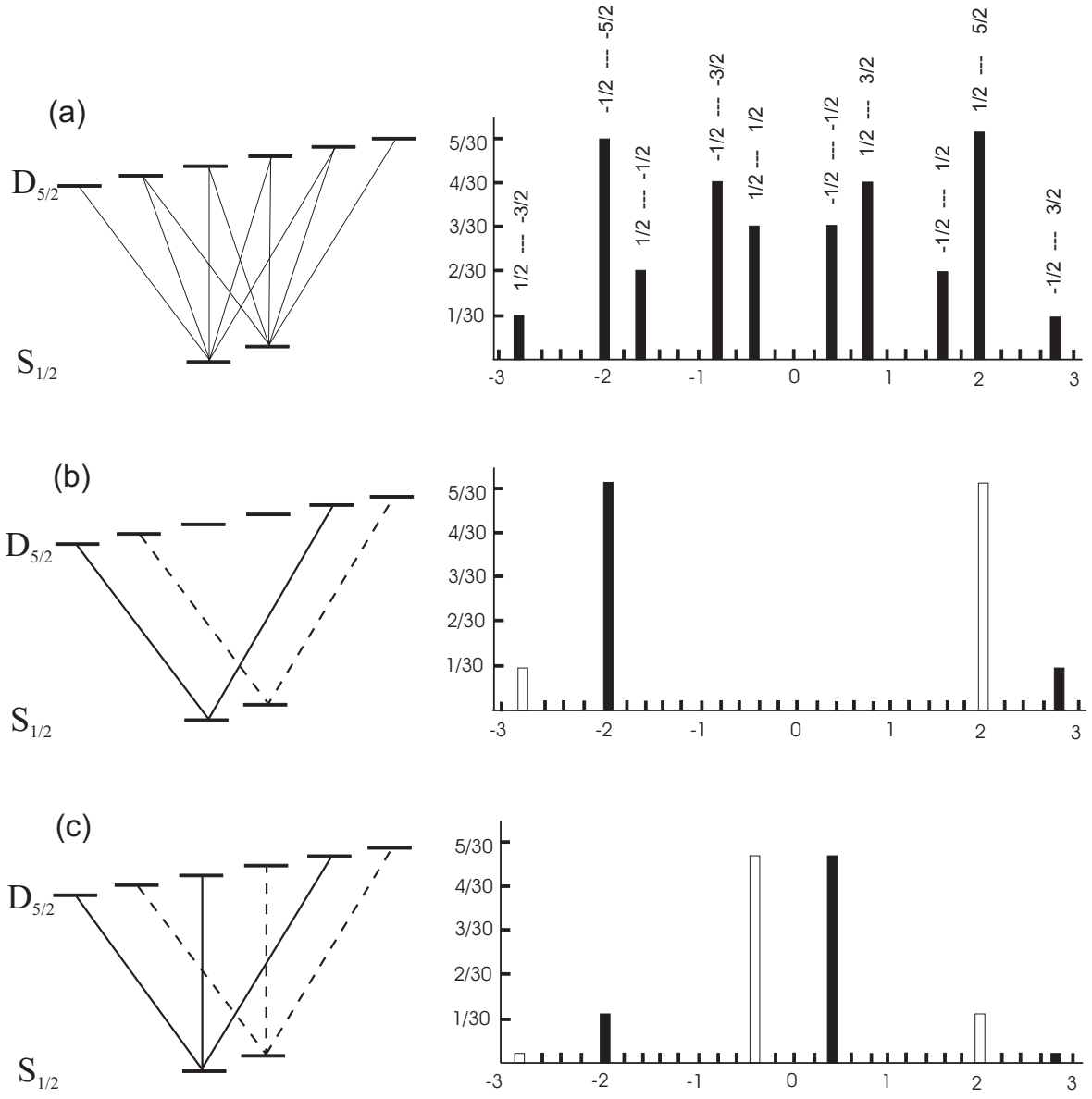

Figure 3.10.: (a) In a non-zero magnetic field the $S_{1/2} \leftrightarrow D_{5/2}$ quadrupole transition splits into ten components whose maximum line strengths are proportional to the their squared Clebsch-Gordan factors. (b) Transitions that couple to the laser if $\boldsymbol{\epsilon} \perp \boldsymbol{B} \perp \boldsymbol{k}$ ($\phi = \gamma = 90°$). (c) Allowed transitions in the case $\phi = 45°, \gamma = 0°$.

2. **Sideband cooling.** The laser at 729 nm is tuned to the lower motional sideband of the ion's motion. The laser at 854 nm shortens the lifetime of the metastable state so that its effective decay rate approximately equals the Rabi frequency on the sideband. In practice, the intensity of the laser at 854 nm is adjusted for optimum cooling results. If several normal modes of the ion's motion are to be cooled to the ground state, the tuning

of the cooling laser has to be sequentially alternated between the different sidebands. At the end of this cooling step, population in the $D_{5/2}$ level is pumped to the $S_{1/2}$ level. To ensure that the entire population is actually in the $S_{1/2}(m = -1/2)$ level, a short pulse of circularly polarised light is applied to the $S_{1/2} \leftrightarrow P_{1/2}$ transition.

3. **Quantum state engineering.** The motional state of the ion can be manipulated by applying pulses of varying frequency and duration on the quadrupole transition.

4. **Quantum state analysis.** Again, one or several pulses of light are applied to the $S_{1/2} \leftrightarrow D_{5/2}$ transition. This serves the purpose of transferring part of the population to the metastable state. The $D_{5/2}$ state population is read out in the next step. There is no clear distinction between steps 3 and 4. At the beginning of step 4, the ion should be in the electronic ground state. If only level occupancies are to be measured, this can be achieved by a pumping pulse with the laser at 854 nm.

5. **Detection.** The Doppler cooling lasers at 397 nm and 866 nm are switched on and the fluorescence of the ion is monitored for several milliseconds. Discriminating between the ion being in the S or D level is done by comparing the number of counts with a threshold value.

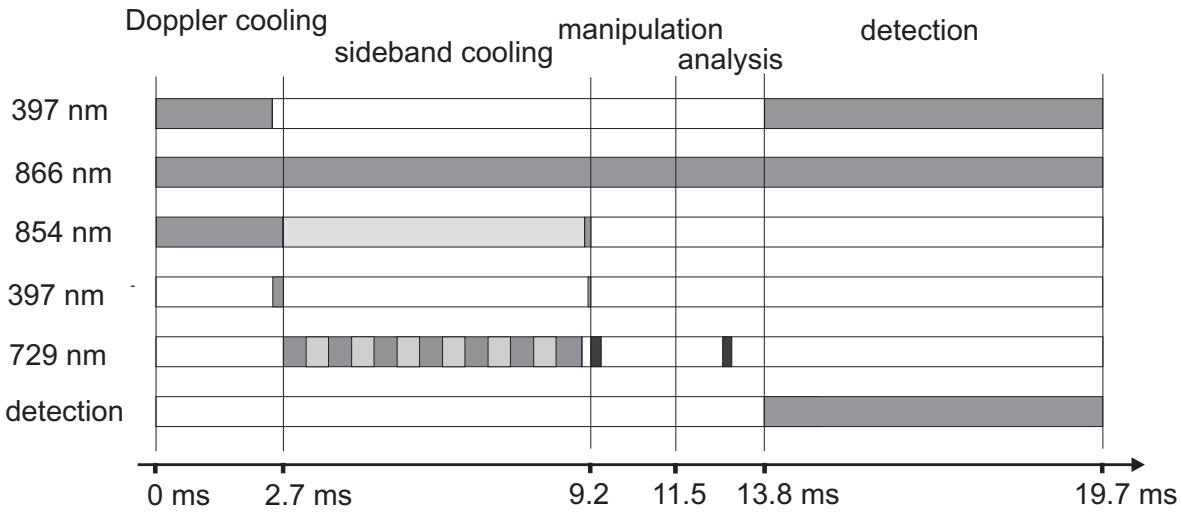

Figure 3.11.: Typical pulse sequence used in the experiments described in chapter 6. Different grey scales indicate changes in intensity or frequency.

Typically, the whole experiment takes beween 5 and 20 ms. By repeating the whole sequence 100 times, the D state occupation is measured. As an example, fig. 3.11 shows a pulse sequence used for simultaneously cooling two motional modes to the ground state of motion. There are many variations of this scheme. In its simplest form, the sideband cooling and state engineering steps are omitted, yielding an excitation spectrum of the quadrupole transition. If the sideband cooling step is directly followed by the state analysis, one can measure the ground state population by the method described on page 25. Delaying the state analysis by

a time τ permits to measure the ground state population as a function of τ. The heating rate of the oscillator can be inferred from such a measurement.

4. Experimental setup

This chapter describes the experimental apparatus. First, a broad overview is given. Then, the individual parts are characterised in more detail. The two main components are the ion

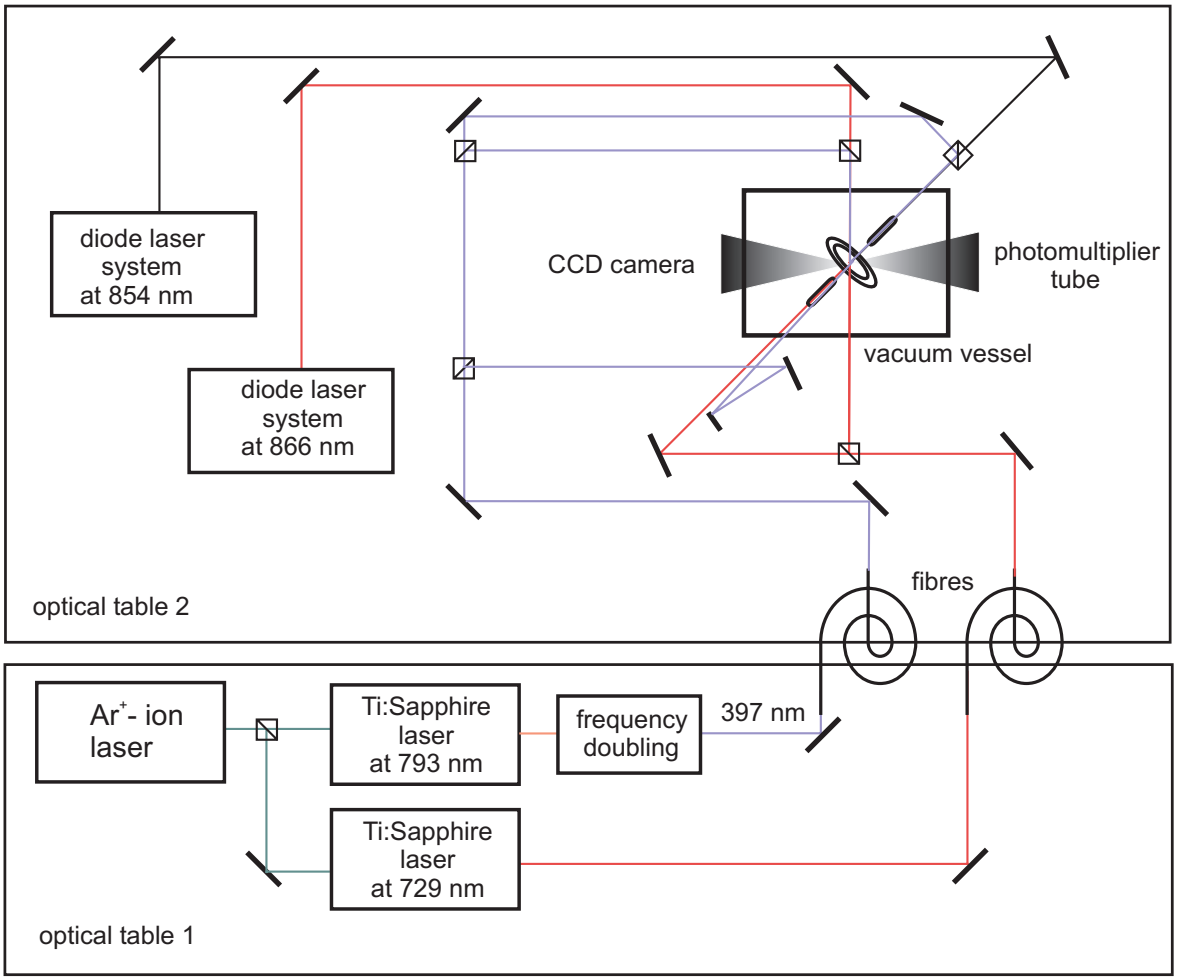

Figure 4.1.: Overview of the experimental setup. The experiment is spread over two optical tables. The Ti:Sapphire lasers together with their stabilisation and the Ar^+ pump laser are located on one table, the diode lasers and the vacuum vessel containing the Paul trap are on the other table.

trap apparatus and the laser sources used for an investigation of Ca^+. They are set up on two optical tables. Fig. 4.1 provides a general overview. Table 1 accommodates the laser sources at 397 nm and 729 nm. Their light is coupled into optical fibres and guided to the other optical table where the trap is mounted in an ultra-high vacuum system. Apart from the trap, the detection systems, i.e. an intensified CCD camera and a photomultiplier, as well as two diode lasers operated at wavelengths of 854 nm and 866 nm are on table 2. The light of the four lasers is split into different beams which are then superimposed with each other and steered onto the ion from six different directions. Finally, there is another ion trap apparatus on the same table. The other trap is a linear trap. It is used to store strings of several ions. Both ion traps are operated in a time-sharing scheme since they share not only all the laser sources but also the CCD camera and the computer control system. The laser beams are directed to one trap or the other by coupling them into different fibres, or by using a polarising beam splitter in combination with a half-wave plate as an adjustable beamsplitter. Except for the trap design, most of the experimental setup has already been described in detail in the thesis of H. C. Nägerl [85]. Since then, the drift stability of the laser sources has been improved.

4.1. Ion trap apparatus

4.1.1. Trap design

An open trap design has been chosen to provide access to the trap center from many different directions. The trap electrodes are made of molybdenum wire with a diameter of 200 μm. The quadrupole potential is generated by a ring electrode with an inner radius of 0.7 mm

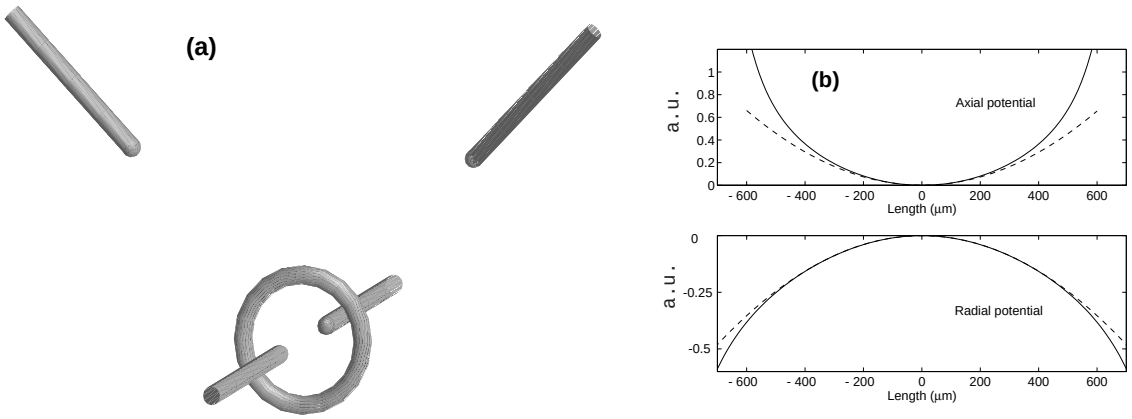

Figure 4.2.: (a) Arrangement of trap electrodes. The quadrupole potential is generated by applying an RF voltage to the ring electrode and a dc voltage to the tips in the symmetry axis of the ring. The other pair of electrodes is used to compensate for stray electric field perpendicular to the trap axis. (b) Potential in axial and radial direction. The dotted lines show the quadrupolar term of the potential.

and two tip electrodes in the symmetry axis of the ring. The distance between the tips is 1.2 mm. Fig. 4.2 (a) shows the arrangement of the electrodes (see also fig. 4.4). Axial trap frequencies of up to 5 MHz are generated by applying voltages of up to 1000 V at a frequency of 20.9 MHz to the ring electrode. The radial trap frequencies are lower by roughly a factor of two. Due to small deviations from the cylindrical symmetry, the radial degeneracy is lifted leaving two axes of symmetry with trap frequencies that differ by approximately 4%. The radio-frequency drive is applied only to the ring electrode which is grounded with respect to dc voltages. By application of a common dc voltage to the tip electrodes, the ratio of axial to radial frequencies is fine-tuned. An asymmetry in the tip electrode voltages shifts the ion towards the more negative tip. Two more tip-shaped electrodes are in the plane of the ring, their tips being separated from the trap center by 3 mm and pointing towards it. These compensation electrodes serve to move the ion in the plane of the ring. The ring electrode is formed by spot-welding the wire into the shape of a ring. The ends of the tip electrodes as well as the compensation electrodes are brought into hemispherical shape by polishing them on a lathe. All molybdenum electrodes are spot-welded to thicker wires with a length of approximately 30 mm and a diameter of 2 mm which are themselves attached to a multipin vacuum feedhrough.

The electrode configuration described above generates a good approximation to a pure quadrupole potential in the centre of the trap, as can be seen from a numerical simulation of the electric potential. Fig. 4.2 (b) shows the potential along the axial and radial directions (see fig. 2.3 (b) for a contour plot of the potential). The curvature varies by less than 10^{-3} over the central 100 μm of the trap. Higher order multipole terms become important outside the centre of the trap. The voltage needed to generate the same curvature at the position of the ion (i.e. the same trap frequency) is increased by a factor of 1.7, as compared with the case of a pure quadrupole potential. Voltages of up to 60 V have to be applied to the compensation electrodes in the plane of the ring in order to shift the ion to the centre of the quadrupole potential. The electric field produced by these electrodes is rather inhomogenous, probably due to the screening effect of the ring electrode. In the experiments, it was found that the ratio of axial to radial frequencies could be chosen to be smaller than two, even if positive voltages were applied to the tip electrodes. This shows that the compensation voltages not only shift the electric field at the position of the ion but also change its gradient. However, this effect does not have any negative consequences for the experiments. Voltage differences of less than 5 V on the tip electrodes are sufficient for compensation in the axial direction. Dc voltages on the tip electrodes are used only for the purpose of compensation since there is no need to change the ratio of axial to radial trap frequencies significantly.

4.1.2. Radio-frequency drive

The drive voltage is generated by feeding a helical resonator [86](quality factor ≈ 200) at 20.9 MHz with an input power of 0.5–3 W. The experimental setup is shown in fig. 4.3. The input power is produced by a function generator[1] and a 5 W amplifier[2]. A variable attenuator allows one to change the trapping frequencies continuously by a factor of four and thus to adjust the RF power. The helical resonator is mounted on top of the vacuum chamber inside a metal

[1]Synthesized function generator DS345, Stanford Research Systems.
[2]ZHL-5W, Mini Circuits.

shield that prevents the electronics of the diode lasers from picking up the drive frequency. All

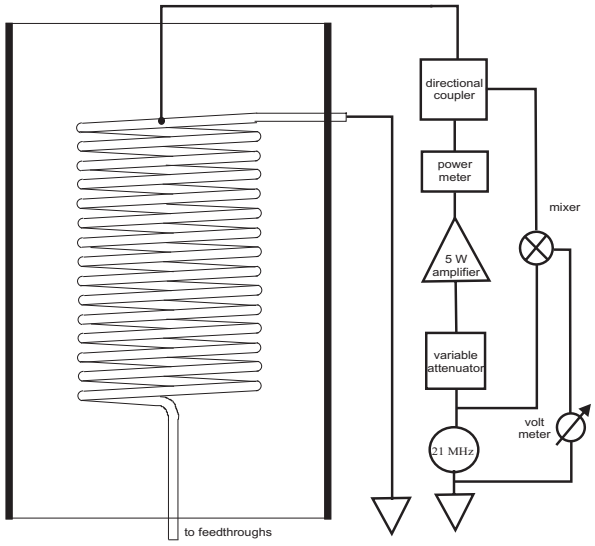

Figure 4.3.: Helical resonator. The copper cylinder (Ø = 10 cm) and the copper helix form a quarter wave resonator.

other electric connections going out of the vacuum system are low-pass filtered for the same reason. The power going into the resonator is measured by a power meter[3]. The reflected power is coupled out by a directional coupler and mixed with a signal at the drive frequency. Measuring the back-reflected power as a DC voltage is useful for impedance matching of the helical resonator and for monitoring its resonance frequency. When more than 2 W are fed into the resonator, it warms up and its resonance frequency changes slightly. After half an hour, an equilibrium state is reached and no further changes to the drive frequency have to be made.

4.1.3. Vacuum vessel

The trap is mounted in a vacuum vessel made of stainless steel. Various flanges provide optical access for the laser beams and for collection of the ions' fluoresence (cf. figs. 4.5 and 4.7). The vacuum vessel is a CF 63 double cross with six extra CF 35 flanges. The geometrical configuration is most easily visualised by imagining a cube around the trap. Then, the CF 63 flanges are at the centres of the cube's faces and the CF 35 flanges are at the corners of the cube, facing each other pairwise at opposite corners of the cube. The symmetry axis of the trap intersects the imaginary cube at the centre of two opposite edges. Fig. 4.4 shows the trap and the three directions that provide optical access for the laser beams. The angles between these laser beams are 70.5° and 54.7°. All windows are tilted by 6° so that back reflections from a beam exiting the vessel can be blocked with an aperture. The trap is mounted from above on a multipin electric feedthrough. The opposite CF 63 flange is used for the Ca ovens

[3] Daiwa CN-410M.

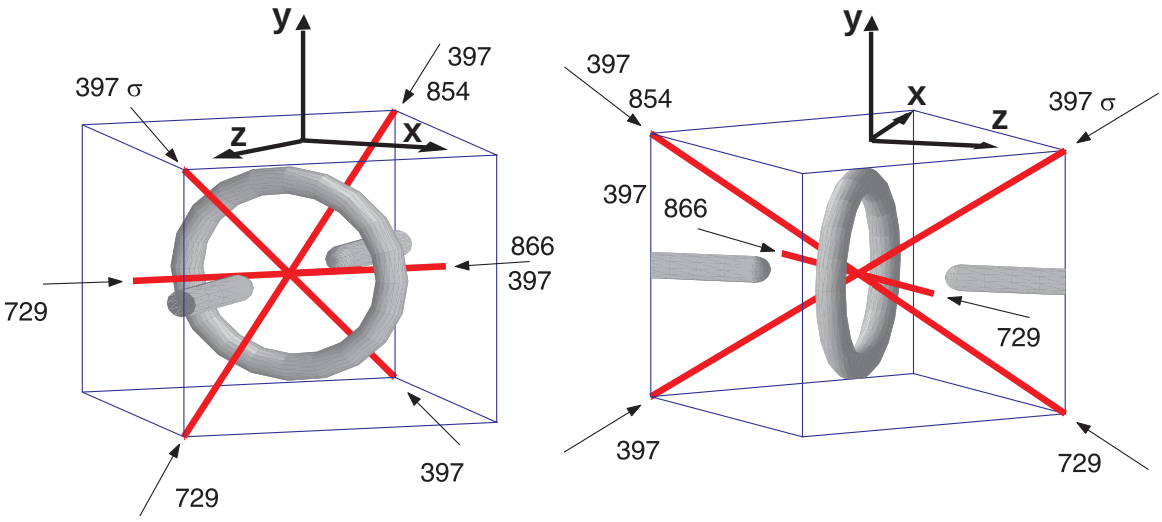

Figure 4.4.: Geometry of trap and laser beams. The coordinate system indicates the principal axes of the trap. All laser beams, indicated by wavelengths in nm, are insensitive to either x - or y - motion of the ion. The fluorescence is collected along the x+z direction. The CF 63 flanges are parallel to the faces of the cube.

and electron sources. The second pair of CF 63 flanges is equipped with tilted windows, the third pair of CF63 flanges is provided with re-entrant viewports, which allow one to place the front side of the lenses as close as 45 mm from the trap center (see fig. 4.7). Each of the two calcium ovens consists of a Ca-filled steel tube 60 mm in length. By sending a current of 3.5 - 4 A[4] through the tube, the vapour pressure of Ca is increased and a (rather poorly collimated) beam of Ca atoms is directed towards the trap. The aperture of the oven is 20 mm away from the trap. Electrons are produced by heating a short filament of thoriated tungsten wire with a current of 4 - 5 A. The filament, with a diameter of 200 μm and a length of 2 - 3 mm, is attached to two metal rods which are in turn stuck in an alumina rod with two holes through it (see fig. 4.6). A bias voltage of -8 V is applied to the filament which accelerates the electrons towards a sheet of tantalum 1 mm in front of the filament. Some of the electrons pass through a 1mm hole in the sheet and can be accelerated by the trapping voltage towards the trap. Two electron sources of this kind are mounted at a distance of 20 mm from the trap. Currents of up to several μA were measured to flow to the ring electrode if a voltage of +100 V was applied to the electrode. The bright yellow light emitted by the filament while loading ions does not add significantly to the stray light detected by the photomultiplier tube.

Before the vacuum chamber was mounted on the optical table it had been baked out at a temperature of 290°C for several days. It is now continuously being pumped by a 20 l/s

[4]It has previously been shown that currents of more than 7 A result in immeadiate and irreversible disintegration of the oven [87].

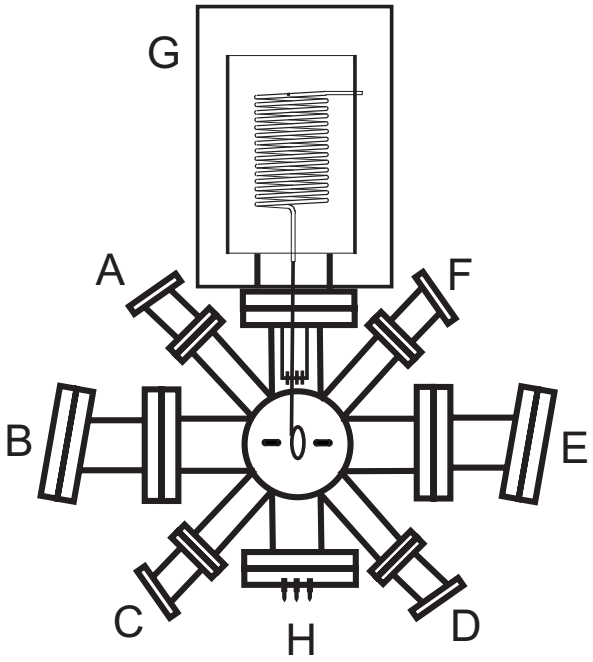

Figure 4.5.: Vacuum vessel as seen from the point of view of the CCD camera. (A-F) Tilted windows, (G) Helical resonator, (H) Ca ovens and electron sources. Getter pump and titanium sublimation pump are connected to a third pair of CF 35 flanges that is not shown in the figure.

ion getter pump[5]. A titanium sublimation pump[6] serves to maintain the base pressure. A pressure better than 10^{-9} mbar can be inferred from the fact that no current through the getter pump could be measured ($I < 0.1\,\mu A$). A pressure of $1 \cdot 10^{-10}$ mbar has been measured by a pressure gauge in another ion trap apparatus that was subjected to the same bakeout procedure and pumped by similar pumps. Therefore, it seems likely that the pressure is also in the range of 10^{-10} mbar in the apparatus described here.

4.1.4. Fluorescence detection

The ions' fluorescence at a wavelength of 397 nm is detected by a CCD camera[7] and a photomultiplier tube (PMT)[8]. The detection setup is shown in fig. 4.7. The fluorescence is collected with two microscope lenses. An f-number of $f \approx 1.5$ is achieved by placing each lens inside a re-entrant viewport so that the front side of the lens is at a distance of only 50 mm from the trapped ion.

The lens used for the PMT images the ion with an enlargement factor of 6 onto a 0.6 mm pinhole to reduce stray light. The pinhole, together with a colour glass filter and the PMT,

[5] VacIon Plus 20 with controller MiniVac, Varian.
[6] Titanium sublimation pump SUB-203, Caburn-MDC.
[7] ICCD, Princeton Instruments.
[8] H5783, Hamamatsu.

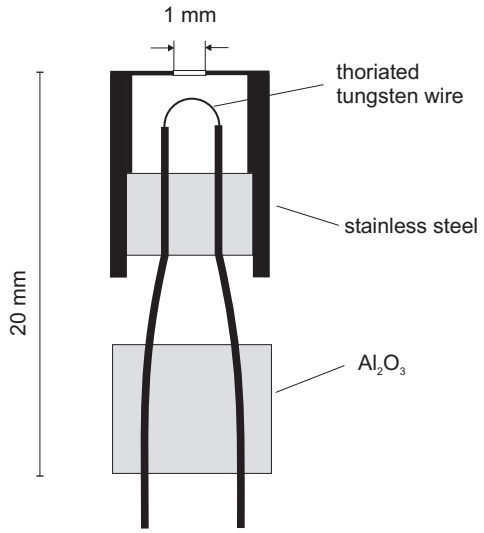

Figure 4.6.: Design of the electron source. The steel sleeve is fixed to the alumina rod by a screw. The lower piece of alumina splits apart and stresses the wires, thereby fixing their position with respect to the upper piece of alumina.

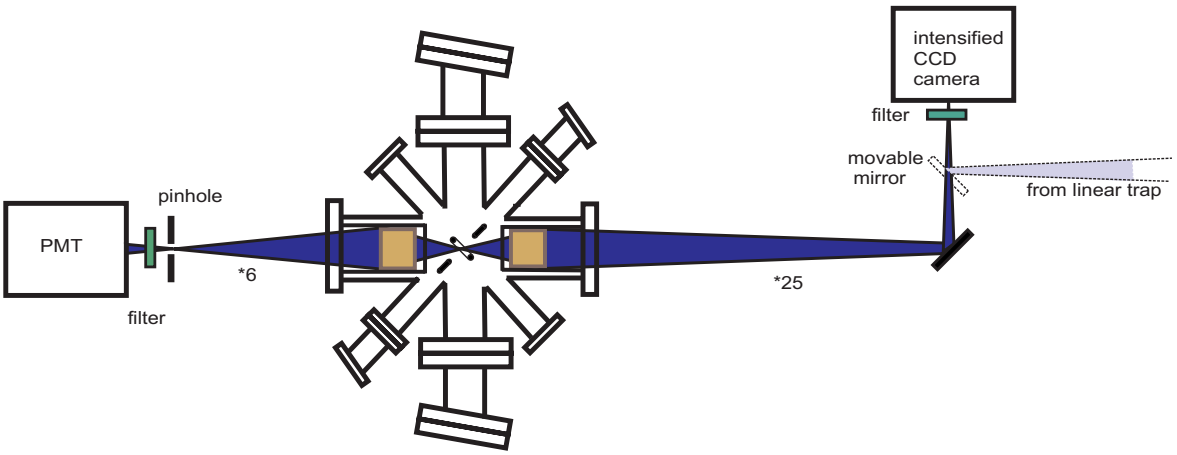

Figure 4.7.: Detection setup at 397 nm. Two microscope lenses placed inside re-entrant viewports are used to image the fluorescence onto a photomultiplier tube and a CCD camera, respectively. A kinematic mirror mount allows to image ions in the linear trap onto the CCD camera.

is mounted on an XYZ translation stage. The quantum efficiency of the PMT is specified to be 11% at 397 nm. At wavelengths above 500 nm its efficiency decreases rapidly so that its sensitivity at 729 nm is reduced by a factor of 10^4. With a transmission of 65% at 397

nm and less than $5 \cdot 10^{-8}$ at 729 nm, the colour glass filter[9] adds to this effect. Fluorescence count rates of up to 30 kHz per ion are achieved on top of a background count rate of 1 kHz, which is predominantly due to scattered light at 397 nm. Neither the dark count rate (< 10 counts/second) nor stray light at 729, 854 or 866 nm play an important role. In principle, a laser beam at 729 nm could be imaged onto the ion[10] by the microscope lens used for the CCD camera even though this beam would be subsequently imaged directly onto the PMT. The pulses from the PMT are amplified 40 times[11] and sent to the discriminator inside a photon counter[12].

The second microscope lens images the ion onto the chip of an intensified CCD camera, which is also used for monitoring ions in the linear trap. The enlargement factor is approximately 25. Since a resolution of a few microns is achieved and the pixel size is $21\,\mu\text{m} \cdot 21\,\mu\text{m}$, the ion is imaged onto a few pixels. A higher magnification would only decrease the rate of collected photons per pixel. Although the ion could be detected within a few milliseconds, typical exposure times are in the range of a few tenths of a second. The CCD camera image provides valuable information concerning the quality of Doppler cooling or the lack thereof. Changes in the ion's position as small as 1 μm can be detected, which allows a crude compensation of micromotion in two dimensions. Finally, the camera is useful for detecting the presence of additional ions other than $^{40}Ca^{+}$ that do not fluoresce. The presence of these ions can be inferred from a shift of the equilibrium positions of the fluorescing $^{40}Ca^{+}$ ions (see fig. 5.3).

4.1.5. Computer control

The whole experiment is controlled by a computer. Programs written in LabView[13] are used for PMT data aquisition, setting of laser frequencies and powers, and for the timing of the experiment. For this purpose, four data aquisition boards are employed. Two of them are multi-function I/O boards[14], the other two are timing boards[15]. The latter are programmed to generate the pulse patterns needed for the sideband cooling and quantum state manipulation experiments. A timing precision of better than $1\,\mu$s is achieved. Two additional pulses are produced by a delay generator[16]. This instrument as well as function generators, a photon counter and a lock-in amplifier are controlled by the computer via GPIB interface[17].

4.1.6. Laser beams

Up to eight laser beams are focussed onto the ion (see figs. 4.4 and 4.8). The blue light at 397 nm is split by two acousto-optical modulators (AOM) into two beams that can be switched

[9] BG40, 3mm.
[10] Ions spaced 20 μm apart have been individually addressed in the linear ion trap using such a beam [44]. Due to the large aperture of the lens, the spot size of the beam could be made as small as 6 μm.
[11] VT120A, EG&G.
[12] SR400, Stanford Research Systems.
[13] National Instruments.
[14] AT-MIO-16XE-50 and PC-MIO E, National Instruments.
[15] PC-TIO-10, National Instruments.
[16] DG535, Stanford Research Systems.
[17] AT-GPIB/TNT, National Instruments.

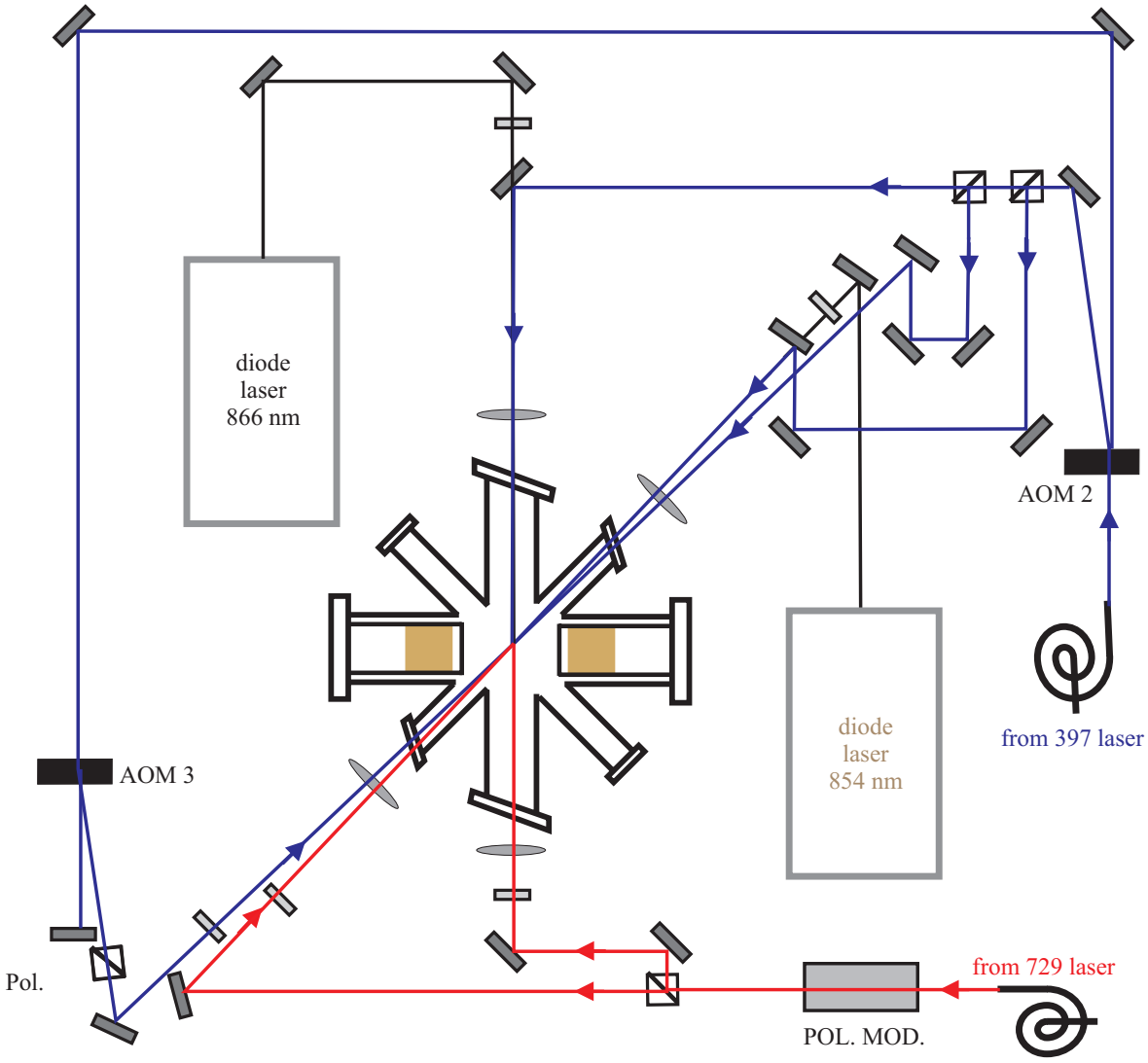

Figure 4.8.: Laser setup near trap. The light at 397 nm is divided into two beams that can be switched on and off independently. A polarisation modulator permits to switch the beam direction of the laser at 729 nm within 50 μs. $\lambda/2$ and $\lambda/4$ denote half- and quarter-waveplates used for polarisation control.

on and off and controlled in power independently. One of the beams is circularly polarised and allows one to prepare the ion in a Zeeman sublevel of the electronic ground state provided that magnetic field vector coincides with the beam's axis of propagation. The other beam is split into three beams that are used for Doppler cooling and compensation of the ion's micromotion. The ability to shut off the blue beams at certain times with a high extinction is essential to the experiments described later. This is accomplished only in combination with another AOM on the other table whose first order beam is coupled into the optical fibre. An

extinction of $3 \cdot 10^{-10}$ is achieved by switching off all three AOMs. The beams are focussed upon the ion (waist size $w_0 \approx 80\,\mu$m) by lenses made of fused silica[18].

The light of the repumping lasers at 866 nm and 854 nm is each separately superimposed by dichroic mirrors on one of the linearly polarised blue beams. Both infrared beams are linearly polarised. In order to avoid optical pumping of the ion into a state decoupled from the laser fields, they need to have a polarisation component that is perpendicular to the magnetic field. The focus of both beams has been chosen to be slightly larger than the focus of the blue beams.

The light of the laser at 729 nm is sent through an electro-optical polarisation modulator and subsequently split by a polarising beam splitter into two beams. Their relative intensities are controlled by the voltage (0 - 240 V) applied to the polarisation modulator. The beam that is reflected by the beamsplitter can be attenuated by a factor of 100, the transmitted beam by a factor of 500. The maximum switching rate is limited to 10 kHz by the electronics. Since all laser beams are perpendicular to either one or the other radial oscillation mode of the ion, both beams are needed if the radial x - and y - oscillators are to be cooled to the ground state simultaneously. This is the only experiment where two beams at 729 nm are required. A relatively small waist size of the beams has been chosen ($w_0 = 30\,\mu$m) since the Rabi frequency depends inversely on the beam size at the position of the ion.

4.2. Lasers

The following subsections describe the setup of the laser sources. The lasers used for excitation on the dipole transitions do not require a demanding frequency stabilisation since the decay rate of the P states is 20 MHz. However, they have to lock reliably over hours and their frequency drift should not exceed a few MHz per hour. Unlike the case of trapped neutral atoms, it is not generally possible to lock the required lasers to atomic resonance lines by Doppler-free spectroscopy techniques. For experiments with trapped Ca^+ ions the lasers have to be locked to temperature-stabilised cavities instead. The requirements for the laser that is used for excitation of the quadrupole transition are much more demanding, concerning its frequency drift as well as its short term linewidth because the latter sets an upper bound to the coherence time that can be achieved. Typically, it takes several minutes to perform a sequence of experiments. Thus, a drift stability of less than 20 kHz per hour is compulsory when coherently exciting the quadrupole transitions with Rabi frequencies of 20 kHz because a 5 kHz change in the laser frequency notably alters the experimental outcome. Finally, the power of the 729 nm laser has to be much higher than the power of the other lasers. While half a milliwatt of light is more than enough to excite the ion on one of the dipole transitions (then the transition can be easily saturated), at least a few ten milliwatts are required for fast coherent excitation of the quadrupole transition. All lasers are stabilised by application of the technique of frequency modulation spectroscopy [88] on an optical resonator, also known as Pound-Drever-Hall stabilisation [89].

[18] Lenses made of ordinary BK7 glass seemed to scatter more light, thereby increasing the stray light background detected by the PMT.

4.2.1. Frequency doubled Ti:Sapphire laser for 397 nm

The light from a commercial Ti:Sapphire laser[19] at 794 nm (1.6 to 2.0 W) is split into one main beam, which is directed towards the doubling resonator, and three auxiliary beams as shown in fig. 4.9. One of these beams passes on to a wavemeter, the second one is superposed

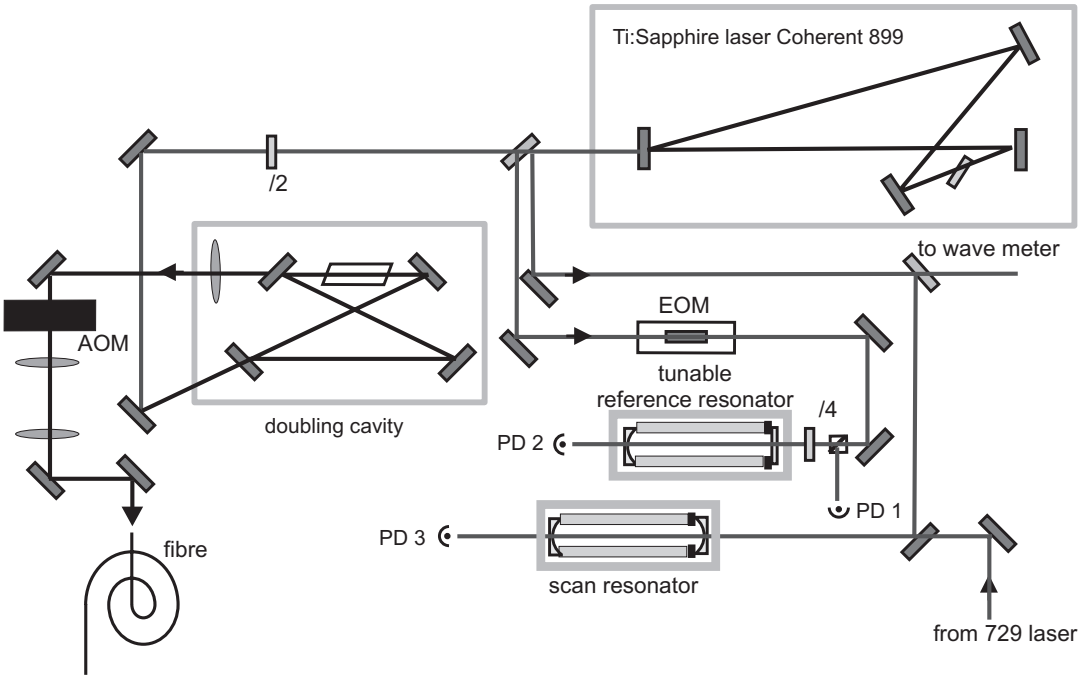

Figure 4.9.: Setup for 397 nm laser. The Ti:Sapphire laser is only shown schematically. PD 2 is a monitoring photodiode, PD 3 is used to detect the transmission peaks for the drift lock, PD 1 is used for deriving the Pound-Drever-Hall error signal. The AOM is used for fast ON-OFF switching in front of the fibre.

with light at 729 nm and is directed towards a drift lock cavity, and the third one enters an electro-optical modulator (EOM)[20] on the way to a stabilisation cavity (finesse F=100). With the Pound-Drever-Hall locking technique the laser has a linewidth of approx. 200 kHz. Presently, the servo loop uses solely the commercial tweeter piezo with a bandwidth of 18 kHz. The enhancement cavity with an LBO crystal for efficient frequency doubling is locked to the 794 nm laser by the Hänsch-Couillaud technique [90]. Up to 80 mW of power at 397 nm is generated, which then passes through a skewed lens for compensation of astigmatism and is coupled into a fibre via a telescope. An AOM in front of the fibre (1^{st} order efficiency 80%) is used for fast ON-OFF switching with a high extinction ratio. The transmission through the fibre is 33% at maximum. Typically we use about 1-2 mW after the fibre. The laser is detuned by scanning the voltage on the piezo of the reference cavity. This allows for a scanning range of up to 5 GHz. When the laser is locked to the cavity it still shows a drift with respect to

[19] CR-899, Coherent.
[20] LM 0202 Phas, Gsänger.

the atomic resonance of up to 1 MHz/min. This drift can chiefly be attributed to the piezo. In order to avoid it, the stabilisation cavity can be locked to the highly stable laser at 729 nm. For details of the locking technique, see ref. [85]. However, there is a tradeoff because the improved drift stability comes at the cost of the 794 nm laser falling out of its lock as soon as the 729 nm laser does so. Therefore, it might be a better idea to use the ion itself as a frequency reference for the 794 nm laser by monitoring its fluorescence.

4.2.2. Ultra stable Ti:Sapphire laser for 729 nm

To meet the high requirements concerning linewidth and stability, this laser is RF-stabilised to a high-finesse cavity with a resonance linewidth of 3 kHz. For that purpose, 5 mW of the light (out of 700 mW) is sent through an electro-optical modulator on the way to the stabilisation cavity. From ring-down measurements the cavity finesse has been inferred to be $F = 220000$ at the laser wavelength. The cavity mirrors[21] are optically contacted to the ends

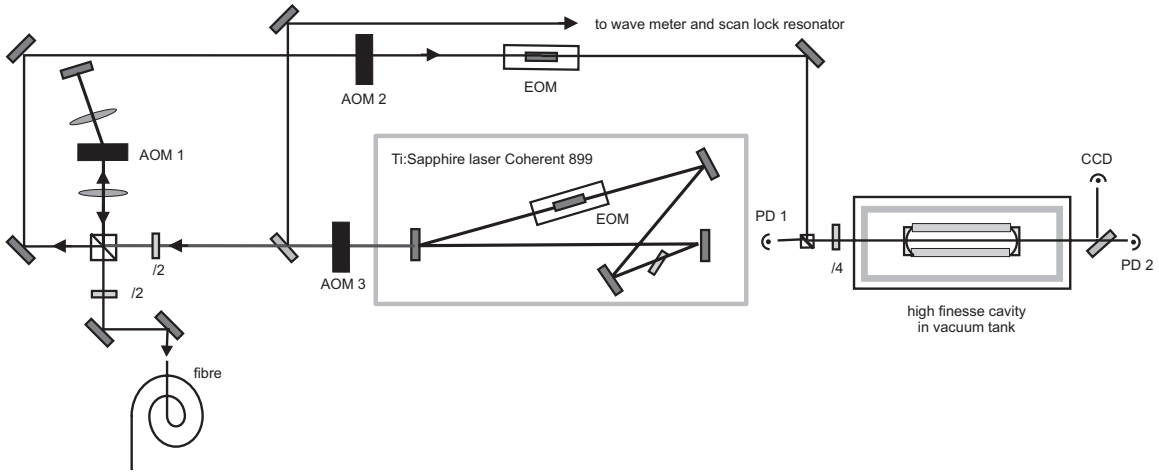

Figure 4.10.: Setup for 729 nm laser. AOM 1 is used in a double pass configuration for fine detuning of the laser frequency. In addition, it serves for power control and fast ON-OFF switching. The transmission through the high finesse cavity is monitored on a photodiode (PD 2) and on a CCD camera. PD 1 is used for deriving the Pound-Drever-Hall error signal. Intensity stabilisation of the laser power is accomplished with AOM 3.

of a cylindrical spacer made of an ultra-low expansion material[22]. The spacer is suspended by thin wires in a vacuum tank in order to achieve a good acoustical and thermal isolation from environmental perturbations. The vacuum tank is pumped to a pressure of less than 10^{-8} mbar by an ion getter pump. The dominant mechanism of energy exchange between the spacer and its environment is black-body radiation. If the spacer was a black body, the relaxation time towards thermal equilibrium would be 10 hours. The vacuum vessel is inside

[21] Research Electro-Optics.
[22] ULE, Corning.

a doubly temperature-stabilised mantle which reduces long-term deviations from the desired temperature to a millikelvin. The light that is back-reflected from the cavity is detected onto a photodiode whose signal is de-modulated, amplified and sent to the tweeter piezo of the ring resonator, to the high-voltage side of an intracavity EOM[23] (bandwidth 100 kHz) and to the RF-side of this EOM (bandwidth 1.5 MHz). A frequency stability of better than 100 Hz with respect to the cavity is deduced from the noise spectrum of the error signal with the servo loop closed. The frequency stability of the cavity is unknown and could only be measured by comparing the laser frequency to the resonance frequency of an independent cavity with a similar finesse. Since the resonance frequencies of the cavity can only be tuned

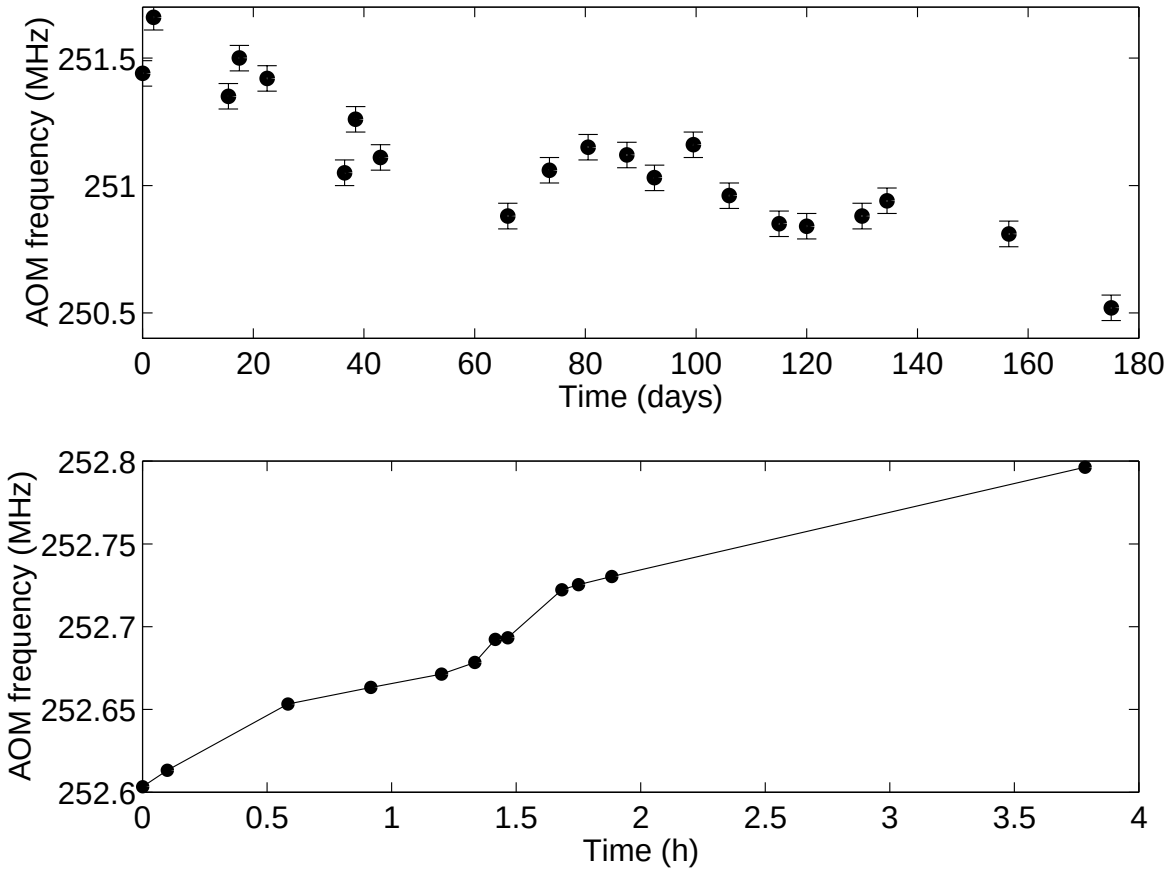

Figure 4.11.: Drift stability of the 729 nm high finesse cavity. Measurements of the resonance frequency of the carriers of two $S_{1/2} - D_{5/2}$ Zeeman transitions allow one to calculate the resonance frequency at zero magnetic field. The long-term drift (a) turns out to be -0.1 Hz per second, a hundred times better than the medium-term stability (b) which is 5 - 15 Hz per second.

[23] PM 25,Gsänger.

by changing its temperature, an AOM[24] is used in a double-pass configuration for setting the frequency and the power of the light that goes to the experiment. The maximum difference between the desired frequency and a TEM_{00} mode of the cavity is 375 MHz (the free spectral range of the cavity is 750 MHz). In combination with another AOM in the locking branch, this gap is bridged by choosing either the 1^{st} or -1^{st} order of the double-pass AOM. A stable function generator[25] is used for driving the AOM. By setting its frequency, the laser can be continuously tuned over a range of 50 MHz without significantly changing its output power. The light is coupled into a fibre (40 % efficiency) so that up to 140 mW are available for the experiments.

The drift stability of the reference cavity is measured by comparing its resonance frequency with the $S_{1/2} \leftrightarrow D_{5/2}$ transition frequency. This is done by measuring the center frequencies of two Zeeman transitions and interpolating the resonance frequencies to the case of zero magnetic field. Fig. 4.11 shows the long-term stability of the laser over the course of six months as well as its medium-term stability. Although the long-term drift is only -0.1 Hz per second, its medium-term behaviour is less satisfactory. Drift rates of 5 - 15 Hz per second are typically observed. The drift rate is always positive and seems to become smaller in the course of several hours. The sign of the drift is consistent with the assumption that the distance between the cavity mirrors increases (the laser frequency goes down). So far, this behaviour is unexplained. As the air temperature changes by as much as two degrees in the vicinity of the Ar^+ laser, it is conceivable that the temperature of the vacuum vessel increases as soon as the Ar^+ laser is switched on. It is also possible that the cavity mirrors slightly heat up locally due to light absorption in the mirror coatings. This conjecture could be tested by measuring the drift rate as a function of the light power coupled into the cavity.

4.2.3. Diode lasers at 854 and 866 nm

Since the diode laser systems closely resemble each other they will be described together. The systems have been characterised in detail in [91, 92]. The diode laser setup at 866 nm shown in fig. 4.12 is described below. The few differences in the setup of the other laser are mentioned in the text. A laser diode[26] with maximum output power 50 mW (100 mW for the laser at 854 nm) is combined with a collimator and an external grating in Littrow configuration to create an extended tunable resonator [93, 94]. The resonator is temperature-stabilised to 5 mK (at about 5° C above room temperature) and put inside a sturdy aluminum box to isolate the setup from acoustical vibrations, temperature fluctuations, and stray RF-fields. The resonator can be coarse-tuned with a fine thread, and fine-tuned with a piezo. This changes the angle of the grating with respect to the direction of light propagation from the diode. Slow integral feedback of the servo loop used for stabilising the laser frequency is applied to this piezo to correct for slow and fast fluctuations. Outside the aluminum box, the laser beam is directed through a pair of anamorphotic prisms for beam shaping and through an optical diode[27] (70 dB isolation) to avoid optical feedback other than that from the grating. The diode laser is again frequency-stabilised to an external reference cavity by the Pound-Drever-Hall method.

[24] Brimrose.
[25] Signal generator 2023, Marconi.
[26] SDL 5401-G1 for laser at 866 nm, SDL 5411-G1 at 854 nm.
[27] I-80-U4, Isowave.

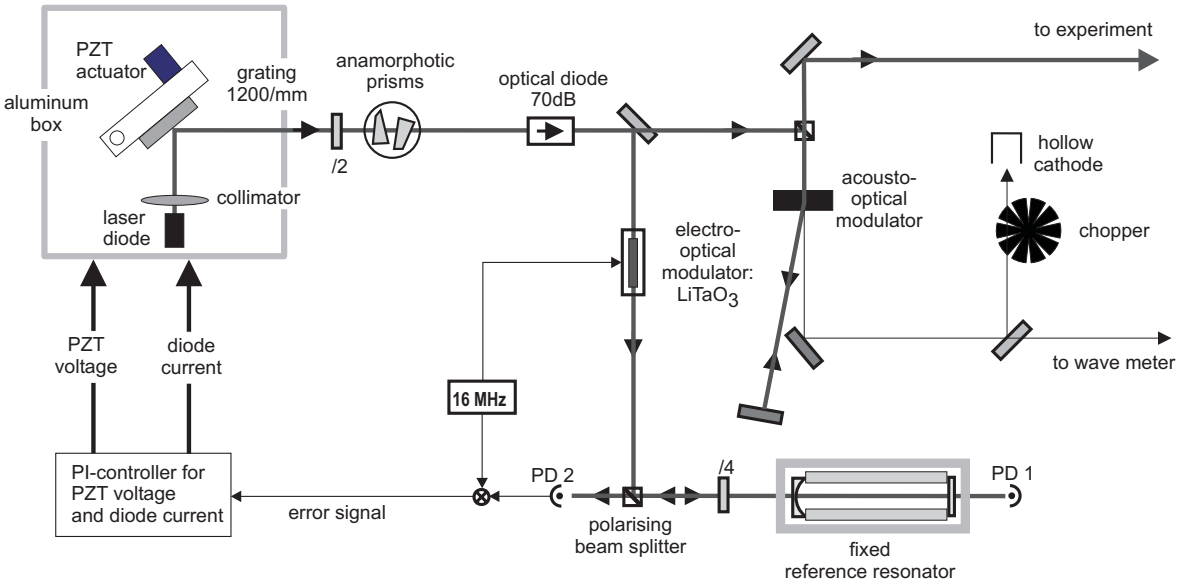

Figure 4.12.: Diode laser setup. The beam from a laser diode in the Littrow configuration is split into a main beam which passes an AOM and a stabilisation beam which passes an EOM on the way to a reference cavity. The light which is not deflected by the AOM is used for opto-galvanic spectroscopy in a hollow cathode. The anamorphotic prism pair for beam shaping is not used in all setups. Instead, a telescope is used to pass the beam through the optical diode.

The linewidth of this cavity is about 1500 kHz (finesse F=1000) to produce a narrow error signal.

After passing through the optical diode, part of the light is sent through an EOM (with a $LiTaO_3$ crystal) to generate sidebands at typically 16 MHz. The reflected light from the cavity is mixed with the local oscillator at 16 MHz to produce the error signal. The fast components of the servo signal then modulate the diode current for stabilisation. The current modulation is achieved with an FET circuitry inside the metal box close to the diode [91].

The main part of the light passes through a 270 MHz double pass AOM for frequency and power control and fast ON-OFF switching of the laser beam. The 0^{th} order light beam is coupled into a wavemeter (Michelson interferometer type), which allows for monitoring the wavelength to a precision of 10^{-7}, and additionally enters a hollow cathode lamp for Doppler-limited opto-galvanic spectroscopy in a hollow cathode [91]. A spectrum is shown in fig. 4.13, where in addition to the Doppler-broadened line the TEM_{00} transmission peaks of a monitor cavity are plotted. These serve as frequency markers. Typically, there are 1 to 3 mW of usable power for the beam directed to the experiment after it has passed the AOM.

The laser at 854 nm can be detuned with the help of the piezo-mounted mirror on the cavity across a few free spectral ranges (FSR = 750 MHz). Its double pass AOM is used only for setting the laser power and ON-OFF switching. As already mentioned, the drift stability of a laser locked to a tunable cavity is much poorer than the stability of a laser which

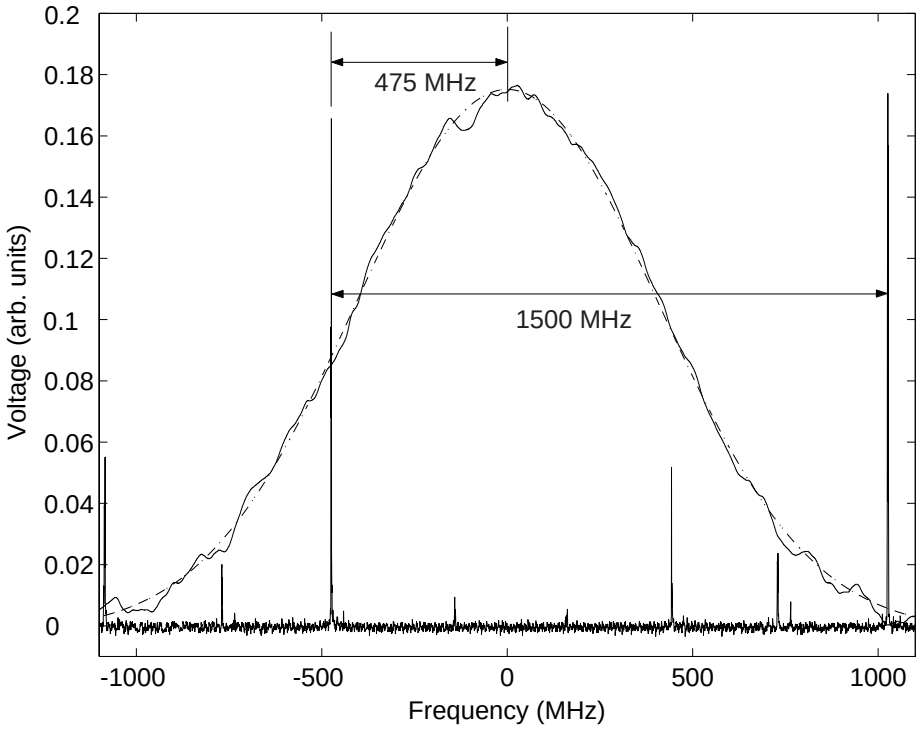

Figure 4.13.: Hollow cathode spectroscopy. The Doppler broadened signal is fit with a Gaussian (FWHM = 810 MHz, corresponding to a temperature of T=400 K). The transmission peaks of a Fabry-Perot cavity are used as frequency markers (free spectral range FSR = 1500 MHz). The laser is locked to the TEM_{00} 475 MHz away from the $P_{1/2} \leftrightarrow D_{3/2}$ transition so that its frequency is shifted on resonance by the AOM.

is stabilised to a fixed reference cavity. Therefore, the present 854 nm laser setup will be replaced by the design chosen for the repumping laser at 866 nm. Here, a very satisfactory drift stability is accomplished by putting the cavity into a pressure-tight steel tube which is then temperature-stabilised in a two-stage setup [92]. When another laser used for saturation spectroscopy of cesium vapor was stabilised to this resonator, its drift was measured to be 300 kHz within 4 hours. This corresponds to a temperature change of the spacer of less than 0.5 mK. For the ion trap experiments the tuning range of the laser ($\approx$ 150 MHz) was set to cover the $P_{1/2} \leftrightarrow D_{3/2}$ transition frequency by adjusting the temperature of the reference cavity. Readjustments of the temperature have to be done only rarely. After five months, the resonance frequency of the cavity had drifted no more than 150 MHz.

4.2.4. Wavelength measurements

The wavelengths of the lasers are measured interferometrically with a wave meter by comparing their respective wavelengths with the known wavelength of a HeNe laser. Two wave meters are used, one of them having a precision of 10^{-6}, the other 10^{-7}, which is due to improvements in the electronic signal processing [95]. If properly aligned, both instruments allow one to determine the laser frequency with an uncertainty of 500 MHz. In case of the lasers locked to fixed reference cavities (729 nm, 866 nm), this precision is sufficient to unambigously identify the proper cavity mode. Although optogalvanic spectroscopy on a Ca hollow cathode lamp does not offer a better resolution, it gives a check that the wave meters are not misaligned. Unfortunately, the life span of the hollow cathode lamps (about 1000 h) seems to be considerably shorter than the life span of the other components of the Ca^+ experiment and the signal quality tends to deteriorate after some time.

5. Ion storage

A number of basic steps has to be carried out before the more advanced experiments described in the next chapter can be undertaken. Most of them are part of the experimental routine and have to be done every time that the experiment is run. These steps serve as a guideline for the organisation of this chapter. The first section describes the procedure for trapping single or a few ions. Different methods for compensation of the micromotion were introduced in section 2.3. After reducing the first order Doppler effect by moving the ion to the centre of the trap, the atomic transitions are investigated by laser spectroscopy and the lasers are properly adjusted for the sideband cooling experiments described later. Though not part of the daily routine, electronic excitation of the ionic motion proves to be a useful tool for characterising some properties of the ion trap apparatus (see section 5.2).

5.1. How to trap single ions

Before a cloud of ions is loaded into the trap, the Doppler cooling lasers have to be set in frequency. As already mentioned, optogalvanic spectroscopy is used to determine the frequencies of the lasers resonant with the $S_{1/2} \leftrightarrow P_{1/2}$ and $D_{3/2} \leftrightarrow P_{1/2}$ transitions. Initially, the cooling laser at 397 nm is red-detuned from the line centre by 800 - 1000 MHz. The repumping laser at 866 nm is tuned to resonance. In the beginning, 200 - 1000 μW of light at 397 nm and 866 nm are sent through the trap. Prior to loading ions, the trapping potential is shortly turned off to get rid of unwanted ions that were possibly trapped before. Then, the trap frequencies are set to moderately low values in the range of 1 - 2 MHz and the vapour pressure of Ca is increased by sending a current of 4 A through the oven. It takes the oven a minute to heat up. After switching on the electron source, Ca atoms that are ionised in the trapping volume start to accumulate. Normally, the loading process takes about a minute. The initial detuning of the cooling laser enhances the probability of trapping Ca^+ ions. The lasers can now be focussed to the centre of the trap by maximising the fluorescence of the ion cloud. For large clouds of several hundred ions (diameter 200 - 250 μm), count rates of up to $3 \cdot 10^6$ per second have been observed.[1] However, smaller clouds are better suited for a precise adjustment of the laser beam positions. Fig. 5.1 shows a CCD image of such a cloud of ions. The initial energy of the ions depends on the position where the ionisation occurred. If, for example, a Ca atom is ionised 100 μm away from the trap centre at a trap frequency of 1 MHz, it aquires a potential energy equivalent to 1000 K, which is much higher than the temperature of the atomic beam. The ion cloud relaxes into a steady state where RF-heating [96] is balanced by laser cooling. The temperature of the ion cloud leads to a

[1] The ion number is estimated from a comparison of the fluorescence rate of the cloud to that of a few non-crystalline ions whose number is known from their crystalline state.

full width $\Delta/(2\pi) = \nu_{SP}\sqrt{2k_BT\log(2)/mc^2}$ at half the maximum height (FWHM) of the Doppler-broadened Gaussian profile of the cooling transition in the range of 1 - 1.5 GHz.

The number of trapped ions is reduced by switching off the cooling laser. The loss rate

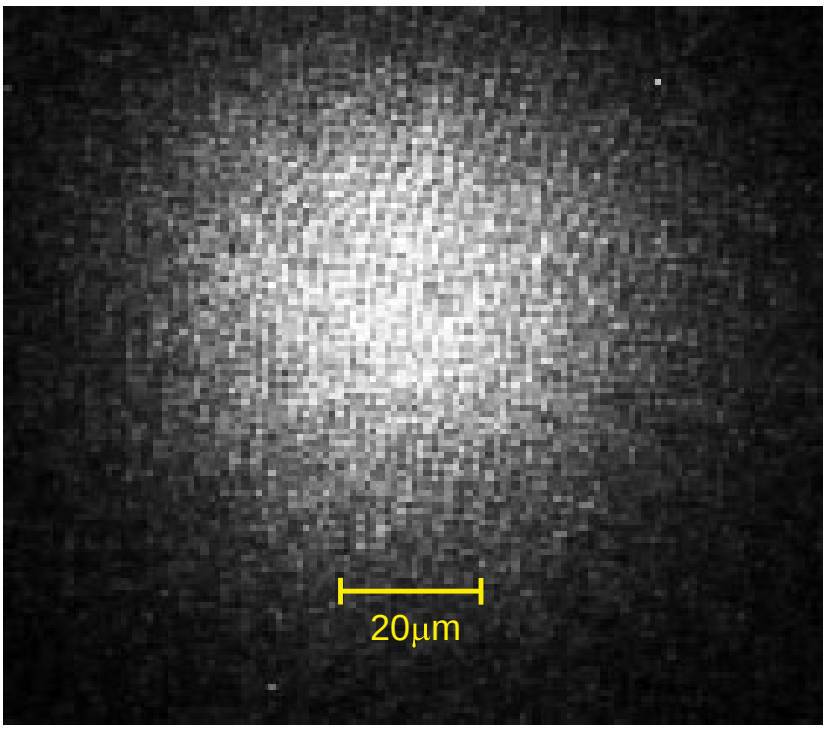

Figure 5.1.: Ion cloud as seen from CCD camera. All CCD images were recorded with exposure times of 0.5 s.

strongly depends on the trap frequency and generally increases with rising frequency. With shrinking cloud size, the frequency of the cooling laser has to be tuned closer to resonance. At low ion numbers, the ion cloud undergoes a phase transition to a state where the ions are arranged in a crystalline structure. This phase transition manifests itself by a pronounced drop in the linewidths of the excitation spectra. The number of scattered photons then suddenly decreases to a much lower value because the cooling laser is usually still red-detuned by several hundred MHz. On the CCD camera, the ordered ion structure is directly visible (see fig. 5.2 and fig. 5.3). Once a crystal has formed, the frequency of the cooling laser can be tuned closer to resonance. In addition, a lower laser power is now sufficient for saturating the atomic transitions. To reduce the ion crystal to a single ion, patience as well as luck is required. The lifetime of an ion in the trap amounts to roughly ten minutes if the ion is not laser-cooled. A single ion can be obtained by repeatedly blocking the cooling laser for 2 minutes. In an alternative approach, the trap is emptied after the lasers have been adjusted on an ion cloud. Then, one tries to load a single ion into the trap. For this purpose, the ionisation probability has to be reduced by lowering the temperature of the filament that provides the electrons.

The process of loading single Ca^+ ions is complicated by the fact that not only are Ca

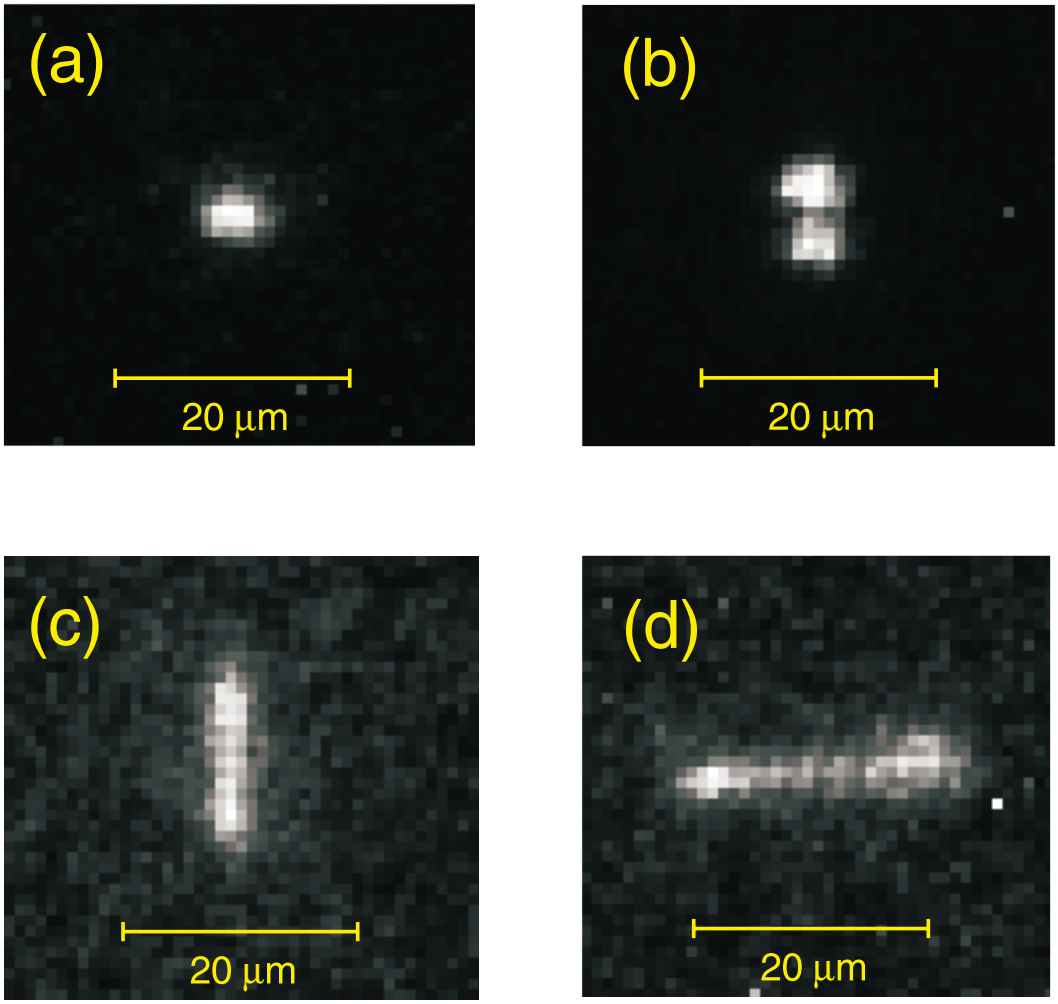

Figure 5.2.: (a) Single Ca^+ ion. (b) Two-ion crystal. The ions are aligned along the weakest axis of the trap. (c), (d) Electronic excitation of the radial modes of oscillation. The ions spend most time at the turning points of the orbit which, therefore, appear brighter. This kind of excitation is useful for measuring trap frequencies and determining the directions of the (radial) normal modes. The axial direction is known from the trap geometry.

atoms ionised and trapped, but also other charged atoms or molecules. The presence of these impurity ions can be derived from a lack of fluorescence at certain positions in the ion crystal. An example is shown in fig. 5.3 (a) where an ion seems to be missing in the lower left corner of the crystal. Impurity ions can be detected even if there is only a single fluorescing Ca

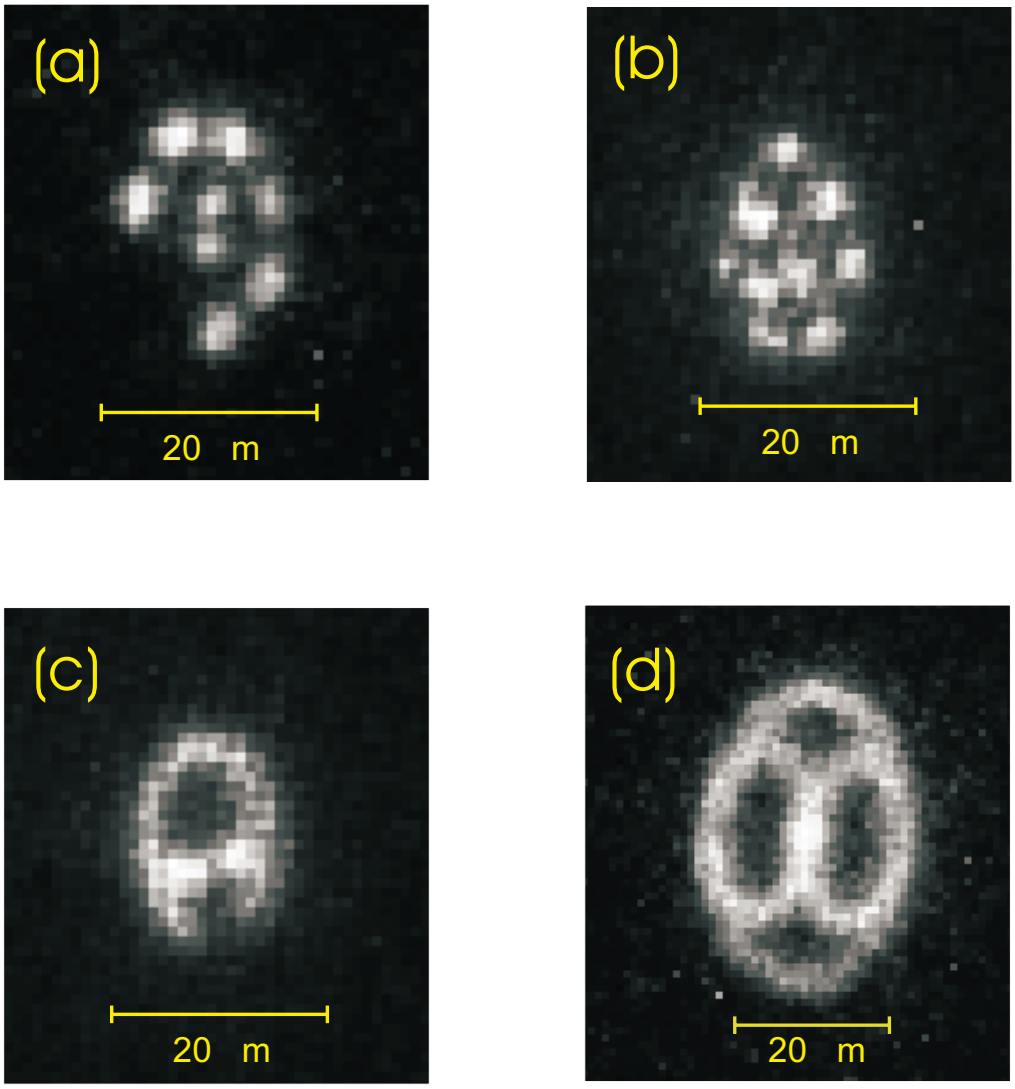

Figure 5.3.: Ion crystals. Crystal (a) contains an impurity ion in its lower left corner while crystal (b) is composed only of Ca^+ ions. (c),(d) Due to insufficient cooling, the ions are free to move over several μm. The crystal (c) probably contains impurity ions. In (d), the ions are arranged in three parallel rings centered along the stiff trap axis. The angle between this axis and the CCD camera direction is 45°.

ion by monitoring its position over the course of several minutes, because the ions tend to swap their positions in the crystal from time to time. Position swapping is probably caused by collisions of background gas particles with the ion crystal, leading to temporary melting

of the crystal. It seems that the mass of the dark ions is close to the mass of ^{40}Ca because attempts to change the trap parameters so that the dark ions are no longer stably trapped were not successful.

5.2. Electronic excitation of the secular motion

A simple method to measure the trap frequencies is to subject a trapped ion to an alternating electric field by applying an ac voltage to one of the trap electrodes. If the field is resonant with one of the trap frequencies, the ion starts to oscillate along the excited normal mode direction, its amplitude of motion being determined by the electric field strength, the laser cooling power and nonlinear terms of the trap potential [97]. The oscillation can be observed on the CCD camera (fig. 5.2 (c) and (d)), and also in the PMT signal by a drop or increase of the photon count rate owing to a change in the ion's velocity distribution. This method permits one to fix the trap frequencies with an uncertainty of 10^{-3}. The stability parameters

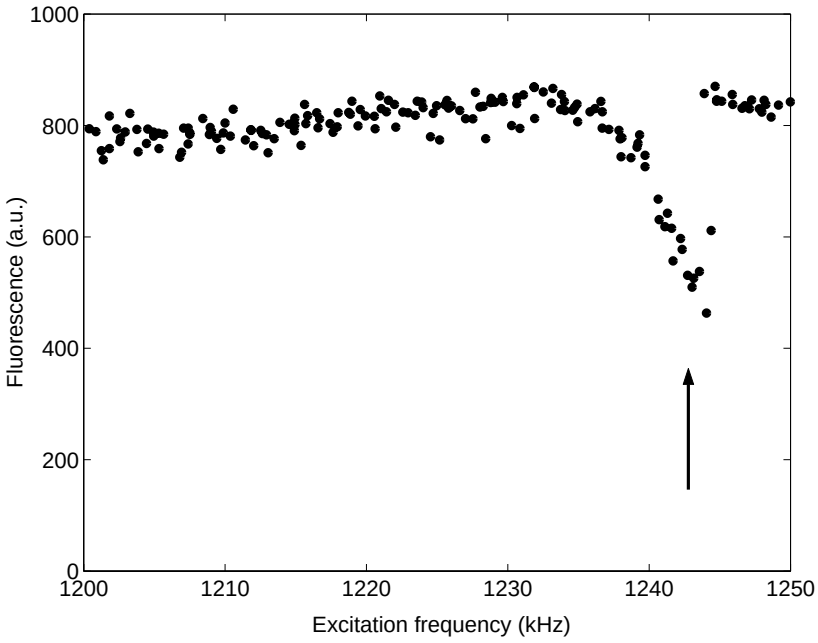

Figure 5.4.: The photon count rate of an ion was recorded while the excitation frequency was slowly swept across the resonance of one of the radial modes of motion. A drop in fluorescence indicates the resonance frequency. The asymmetric shape of the resonance is caused by the slight anharmonicity of the trap potential [98].

(a,q) can be calculated by measuring the axial as well as the radial oscillation frequencies. In the experiments, trap frequencies varied between $(\omega_x, \omega_y, \omega_z)$= (695, 665, 925) kHz and (2315, 2230, 4880) kHz, corresponding to stability parameters $0.15 \leq q_z \leq 0.62$, $-0.005 \leq a_z \leq 0.01$. The 4% difference between the two radial frequencies is caused by asymmetries of the ring

electrode[2]. It cannot be changed by varying the dc-voltages of the other electrodes due to the screening effect of the ring.

Electronic excitation of the normal modes of oscillation is also possible in case of small ion crystals. For a two-ion crystal, a measurement of the lowest center-of-mass motional frequency has been used to measure the magnification factor of the CCD light path by relating the distance between the ions to the separation of their images on the CCD chip.

For a two-ion crystal composed of a $^{40}Ca^{+}$ ion and a dark ion, measurements of the normal mode frequencies of the crystal open up the possibility to find out the mass of the impurity ion, provided that the oscillation frequencies of a single $^{40}Ca^{+}$ ion are known. In fig. 5.5, the calculated normal mode frequencies of such a crystal are plotted as function of the mass of the dark ion. The measured center-of-mass frequencies of the two-ion crystal[3], indicated by horizontal lines, suggest that the dark ion had a mass of 39 u. Although the measured

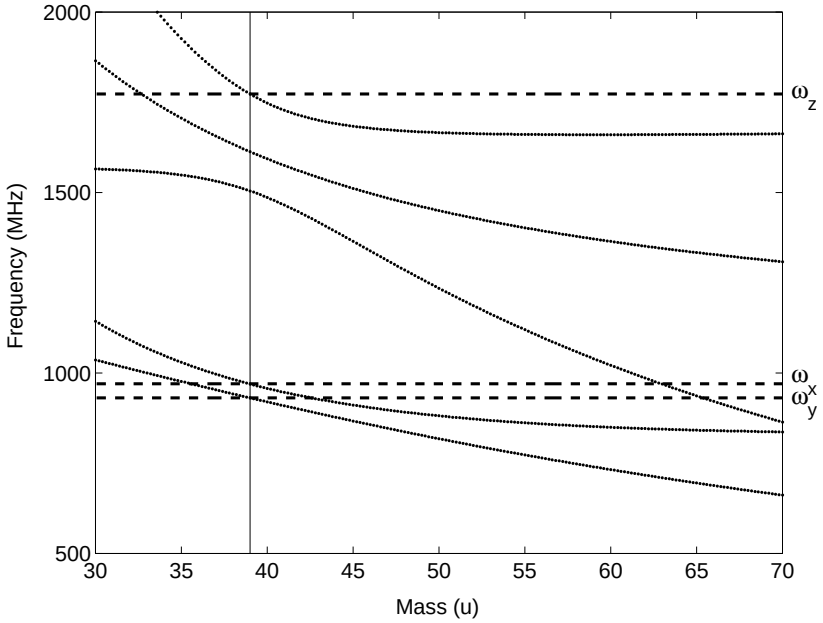

Figure 5.5.: Measurement of the mass of a dark ion. The dotted lines represent the measured COM mode frequencies of a two-ion crystal composed of a $^{40}Ca^{+}$ ion and a dark ion. The solid lines are normal mode frequencies calculated from eq. (2.17) as a function of the dark ion's mass, (the sixth normal mode, which has got a much lower frequency, is not shown. All calculated frequencies coincide with the measured ones for a dark ion with mass u=39.

and calculated frequencies seem to agree quite well for this mass number, the accuracy of the method should not be over estimated. It strongly relies on a precise measurement of trap

[2]Fortunately, the ring turned out not to be completely symmetric. With degenerate mode frequencies, laser cooling would have become much more involved.

[3]After this measurement, the dark ion was removed from the trap and the secular frequencies of the Ca ion were measured.

stiffness which is done with a single Ca^+ ion. The results of this measurement scheme are only reliable if the trap parameters do not change between the two measurements. In another attempt to figure out the mass of a dark ion in a two-ion crystal, the normal mode frequencies inferred from the shape of the spectrum of the $S_{1/2} \leftrightarrow D_{5/2}$ transition were consistent with a mass number u = 43 or u = 44. The origin of the impurity ions is not known so far.

5.3. Compensation of micromotion

Stray electric fields are likely to shift the ion from the RF zero-point to a region where the ion oscillates under the influence of alternating electric fields. The resulting Doppler shift aggravates, or even impedes, many experiments that require atomic transitions to be kept in resonance with light fields. Furthermore, if the amplitude of oscillation is larger than a fraction of a wavelength, the ion cannot be placed at a certain point in a standing wave of light. In the context of laser cooling, Doppler cooling becomes less efficient because the cooling transition is broadened by the moving ion. Therefore, it is highly desirable to cancel electric stray fields. Four techniques for compensating micromotion have been used in our experiments. They are presented in the next paragraphs. The efficiency is discussed in ref. [53].

5.3.1. Coarse compensation

In two dimensions, compensation of micromotion is achieved by lowering the strength of the RF-potential and monitoring the position of the ion with a CCD camera. By applying voltages to the compensation electrodes, the ion has to be shifted to a point which is independent of the RF-field strength. This method is only efficient at low trap frequencies. Besides, it has to be combined with other techniques since it does not permit to precisely detect the position of the ion in the CCD direction.

Another method for reduction of micromotion utilises the spectral shape of the $S_{1/2} \leftrightarrow P_{1/2}$ transition[4]. Its width is broadened by micromotional sidebands. After desaturating the laser at 397 nm and red-detuning it so that the photon scattering rate is reduced to approximately 50 % of the rate measured on resonance, one can try to lower the scattering rate even further by application of compensation voltages. The scattering rate is sensitive to all micromotional components, if the ion is illuminated by several laser beams from different directions. Alternatively, one can try to maximise the fluorescence rate on resonance.

5.3.2. Correlation measurements

A more sensitive technique relies on correlations between the arrival of photons at the PMT and the phase of the radio-frequency field that arise from the time-dependent Doppler shifts of the lasers in the rest frame of the ion. If the cooling laser is red-detuned, the absorption probability is maximised once every cycle when the ion moves towards the laser beam. The scattering rate is also velocity-dependent since the lifetime of the $S_{1/2}$ level (7 ns) is short compared to the RF-period (50 ns). The setup for the correlation measurement is shown

[4] In the limit of low saturation, the excited state population is proportional to $\sum_{n\in\mathbb{Z}} J_n(\beta)^2/((\Delta - n\Omega)^2 + \gamma^2)$, where Ω is the RF-frequency, Δ the detuning, γ the decay rate and β the micromotion modulation index [99, 100].

in fig. 5.6. The arrival of a photon triggers a time interval counter[5] which is subsequently

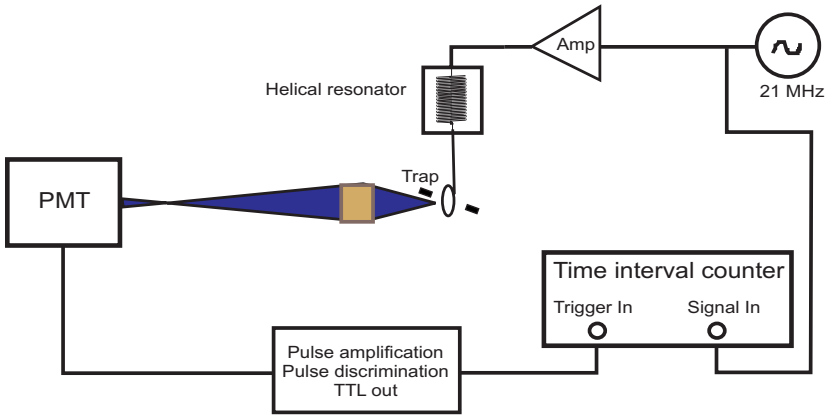

Figure 5.6.: Setup for compensation of micromotion. The time interval counter measures the time interval between the arrival of a photon at the PMT and the phase of the radio frequency field. The micromotion in the direction of the laser that excites the ion is compensated by minimising the modulation of the correlation signal by application of suitable compensation voltages.

stopped by a pulse synchronised to the RF drive frequency. From 10000 measurements each obtained by a single photon count, a histogram of time intervals is built up within a couple of seconds. The amplitude modulation of the distribution is proportional to the micromotional amplitude. This technique is sensitive only if the photon scattering rate strongly depends on the detuning of the laser. Therefore, the laser frequency should be tuned to the point of the steepest gradient of the fluorescence curve. Care has to be taken that the transition is not broadened by saturation. By keeping the stray light level low, a satisfactory sensitivity is achieved without sacrificing too much time to long data acquisition periods. Typically, the fluorescence count rate was 10 kHz while the stray light rate was 1 kHz or below. The correlation technique is sensitive to micromotion along the direction of the laser beam. It was shown in section 2.3, that all triplets of compensation voltages that do not give rise to micromotion in a certain direction lie in a plane. This can be seen in fig. 5.7 where points with vanishing micromotion along three non-collinear directions have been measured. The voltage triplet that shifts the ion to the centre of the RF quadrupole field is obtained by fitting planes to the data sets. The intersection point of the three planes yields the desired voltage triplet. The orientation of the planes does not have to be measured every time the micromotion is compensated, since changing stray electric fields only shift their distance from the origin (compare for eq. (2.14)). Once the normal vectors of the planes are known, it suffices to determine a single point on each plane in order to calculate the compensation voltages. The success of this method relies on a precise knowledge of the normal vectors. However, the orientation of the planes might shift if the position of the trap electrodes with respect to each other changes, which apparently happened more than once in the course of the

[5] SR620, Stanford Research Systems.

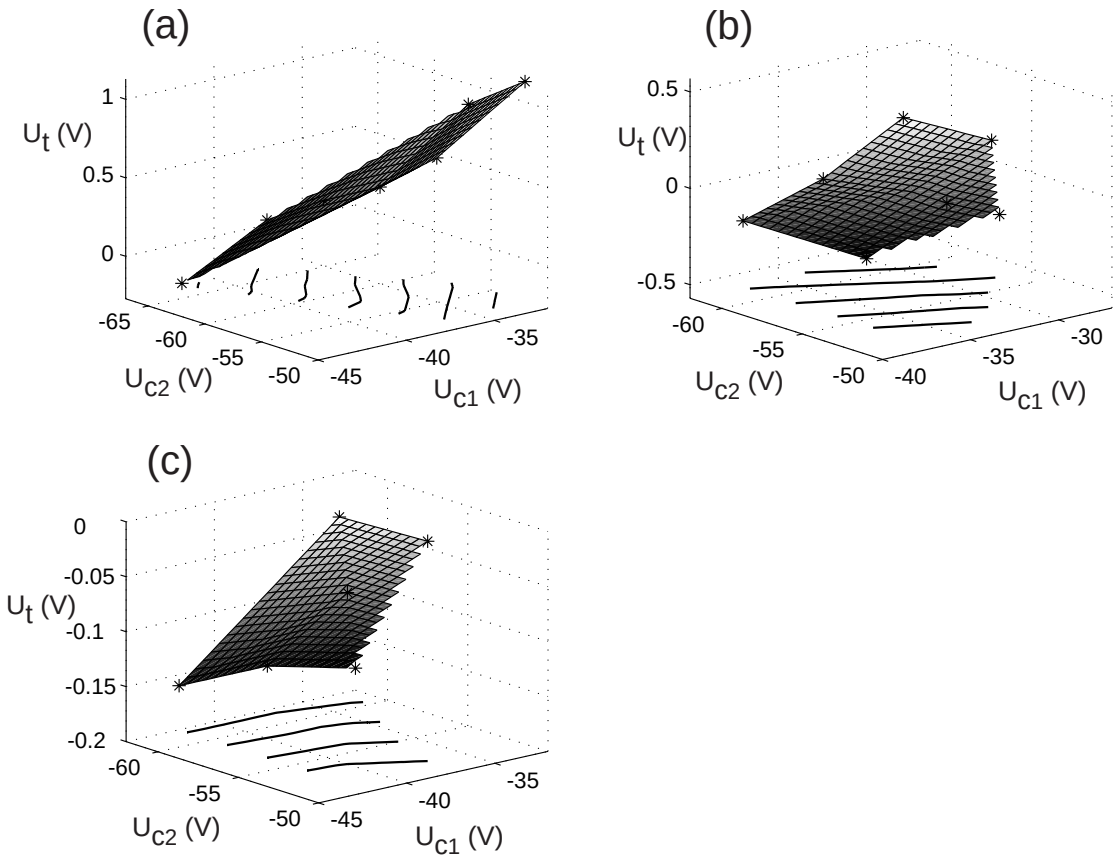

Figure 5.7.: Compensation voltage triplets (U_t, U_{c1}, U_{c2}) that shift the ion to a position with no micromotion in the direction of one of the laser beam. (a-c) show the planes obtained for the different beam directions of fig. 4.4. Measured voltage triplets are indicated by stars, the resulting surfaces (the meshes) are also represented by contour lines in the U_{c1}–U_{c2} plane. These appear to be more or less parallel and equidistant, proving that the surfaces have a planar geometry. The point $(U_t, U_{c1}, U_{c2}) = (-0.20, -64.0, -42.5)\,V$ is common to all three planes (U_t is the voltage applied to one of the tip electrodes, U_{c1}, U_{c2} are the voltages of the electrodes in the plane of the ring.

experiments. Under these circumstances, iterative compensation procedures seem to be more robust. Knowledge of the normal vectors is helpful for devising a compensation strategy that lets the compensation voltages quickly converge to the values corresponding to the ion in the trap centre. Both the iterative and the deterministic methods have been applied successfully in the experiments.

5.3.3. Resolved sideband measurements

Yet another experimental technique of detecting micromotion consists of resolved sideband spectroscopy on a narrow atomic transition. By determining the Rabi frequency Ω_1 of the first micromotional sideband of the $S_{1/2}(m = -1/2) \leftrightarrow D_{5/2}(m = -5/2)$ transition and comparing it to the Rabi frequency Ω_0 of the carrier (cf. chapter 5), the modulation index β is directly measurable, since $\Omega_1/\Omega_0 = J_1(\beta)/J_0(\beta) = \beta/2 + \mathcal{O}(\beta^2)$ in the limit of low modulation. Fig. 5.8 shows the modulation index as a function of the compensation voltage U_t. The minimum modulation index is only 0.021. This residual micromotion is probably due

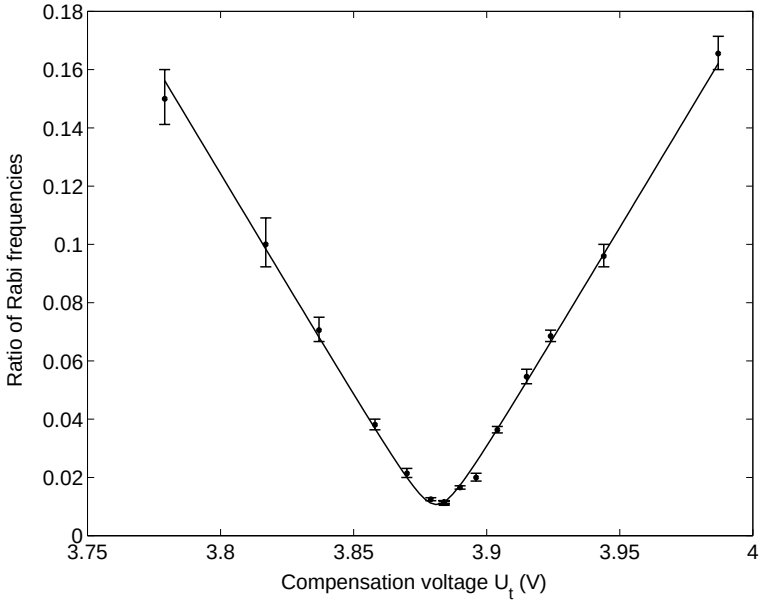

Figure 5.8.: Ratio Ω_1/Ω_0 of the Rabi frequencies on the first micromotion sideband and the carrier as a function of the compensation voltage. At the minimum, a modulation index $\beta = 2\Omega_1/\Omega_0 = 0.021$ is measured. The data are fitted by a function $\beta(U) = B\sqrt{(U_t - U_0)^2 + V^2}$.

to an unbalanced capacitive coupling of the RF field to the tip electrodes, causing an electric dipole field alternating at the drive frequency. This field component had been disregarded in the discussion of section 2.2 because of its small magnitude. Since it is 90° out of phase with the quadrupole component, the time-varying part of the electric field in the direction of the laser beam may be written $E(t) = E_q(\mathbf{r})\cos(\Omega_{RF}t) + E_d\sin(\Omega_{RF}t)$. $E_q(\mathbf{r})$ depends linearly on the position $\mathbf{r}$, which itself is a linear function of the compensation voltage. Thus, the magnitude $|E_0|$ of the electric field may be written

$$|E_0| \propto \sqrt{E_q(\mathbf{r})^2 + {E_d}^2} \propto \sqrt{(U - U_0)^2 + V^2}\,,$$

resulting in a hyperbolic dependence of the modulation index β on the compensation voltage U. For $\beta_{min} = 0.021$, the amplitude of micromotion is only $x_{min} = \beta_{min}(\lambda/2\pi) = 2.5$ nm,

corresponding to an electric field $E_{min} = m\Omega_{RF}^2 x_{min}/e$ of 17 mV/mm.

In our experiments, micromotion compensation is done routinely using the correlation method. By the above technique, it could be ascertained that the correlation method allows one to achieve minimum modulation indices in the range of 0.05. Though slightly more precise, the resolved sideband method would require three beams at 729 nm for a micromotion compensation in all directions.

5.4. Excitation spectra

Once the micromotion has been compensated, excitation spectra can be recorded on the dipole transitions, the width of the spectra being dominated by the radiative lifetime of the $P_{1/2}$ level. The spectroscopic information that is gained from the spectra presented in the next paragraphs, enables a precise setting of the laser parameters for the pulsed spectroscopic experiments described in the next chapter.

5.4.1. $S_{1/2} \leftrightarrow P_{1/2}$ cooling transition

Spectra of the $S_{1/2} \leftrightarrow P_{1/2}$ transition are taken by slowly scanning the laser frequency across the resonance, while the laser at 866 nm prevents optical pumping to the $D_{3/2}$ level. Fig. 5.9

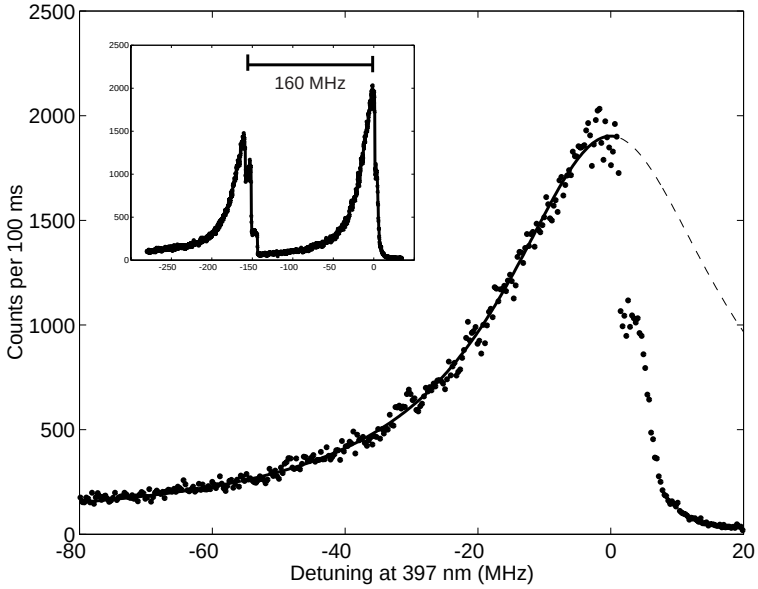

Figure 5.9.: Excitation spectrum of a single ion at 397 nm in a magnetic field of 3.5 G. When the detuning becomes positive, the ion is heated by the laser. The data set is fitted by a Lorentzian (dashed line) with a full width at half maximum of 36 MHz. The inset shows the signal used for the calibration of the frequency axis. For this purpose, the ion was excited by two laser beams that differed in frequency by 160 MHz.

shows a typical example. The asymmetric line shape is explained by the fact that the temperature of the ion depends on the detuning of the laser at 397 nm. As soon as it becomes positive, the ion is heated by the laser. For a proper fit, a self-consistent solution to the equations determining the line shape and the motional state of the ion would be required. Here, the line shape is simply approximated by a Lorentzian with a FWHM of 36 MHz. The measured width is close to the natural linewidth of 22 MHz when taking into account that the $S_{1/2}$ Zeeman levels are split by 9 MHz by a magnetic field of 3.3 G. The scaling of the frequency axis was inferred from the spectrum reproduced in the inset of fig. 5.9. For that purpose, the $S_{1/2} \leftrightarrow P_{1/2}$ transition was excited twice by two counterpropagating beams that differed in frequency by 160 MHz [6].

5.4.2. $D_{3/2} \leftrightarrow P_{1/2}$ transition

When recording spectra of the $D_{3/2} \leftrightarrow P_{1/2}$ transition, the laser at 397 nm is kept at a fixed frequency, while the laser at 866 nm is scanned across the resonance. This is done by changing

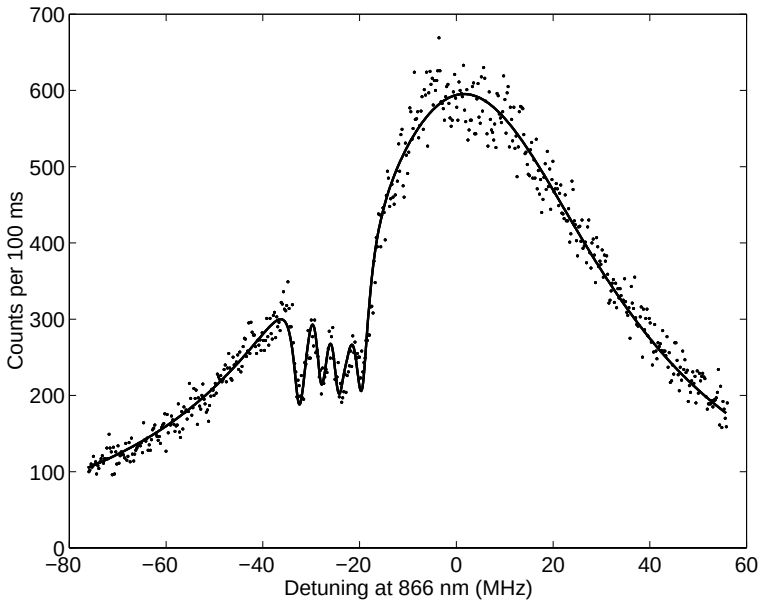

Figure 5.10.: Excitation spectrum at 866 nm. To the left of the resonance, coherent population trapping in superpositions of the $S_{1/2}$ and $D_{3/2}$ levels reduces the excitation rate to the $P_{1/2}$ level. Solid line: Using the 8-level Bloch equations to produce a fit to the data [101], a number of parameters can be determined: Detuning at 397 nm $\Delta_{397} = -25.5(9)$ MHz, saturation parameters $S_{397} = 0.53(2)$, $S_{866} = 4.2(3)$, combined laser linewidth $\delta = 430(50)$ kHz, magnetic field $B = 4(0.7)$ Gauss, $\angle(\epsilon, B) = 86(10)^\circ$.

[6] One of the Doppler cooling beams was chosen, the other one was the beam usually used for optical pumping into the $S_{1/2}(m = -1/2)$ level. For the calibration of the frequency axis, it was linearly polarised and detuned in frequency by adjusting the AOM to a different order of diffraction.

the frequency of its AOM. Compared with the cooling transition, spectra of the $D_{3/2} \leftrightarrow P_{1/2}$ transition are much more easily interpreted because the influence of the laser at 866 nm on the motional state of the ion is negligible as long as Raman effects occuring in the vicinity of the point $\Delta_{866} = \Delta_{397}$ are disregarded. Fig. 5.10 shows an excitation spectrum at 866 nm. The dips in the fluorescence curve to the left of the resonance indicate dark states where population is trapped in a coherent superposition of the $S_{1/2}$ and $D_{3/2}$ levels whenever the lasers have equal detunings with respect to the $S_{1/2} \leftrightarrow P_{1/2}$ and $D_{3/2} \leftrightarrow P_{1/2}$ transitions. This peculiar line shape can be used to extract information about the detuning of the lasers, their intensity and their combined linewidth (see figure caption 5.10), by numerically solving the Bloch equations to produce a fit to the data [101]. Close to a dark state, the density matrix sensitively depends on the detuning of the lasers. In all later experiments, the experimental difficulty of keeping the detuning of the blue laser fixed is avoided by setting the laser frequency at 866 nm on, or several MHz above, resonance.

5.4.3. $D_{5/2} \leftrightarrow P_{3/2}$ transition

For a spectroscopic investigation of the $D_{5/2} \leftrightarrow P_{3/2}$ transition, the $D_{5/2}$ level has to be populated. Therefore, all lasers are switched on when the laser at 854 nm is scanned. The laser at 729 nm induces quantum jumps in the fluorescence. If the excitation is strong enough, many jumps occur within the 100 ms interval of fluorescence collection, so the mean fluorescence rate is reduced to approximately half of the maximum value by the laser at 729 nm. As

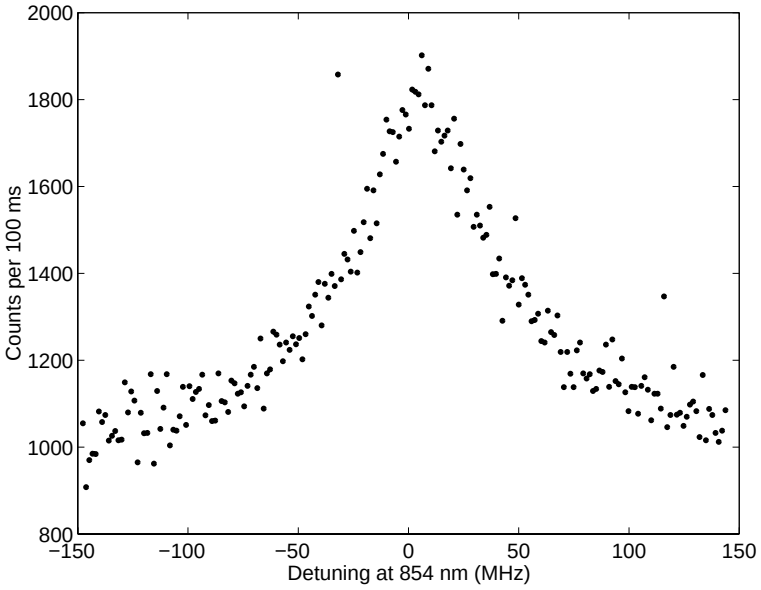

Figure 5.11.: Spectrum of the $D_{5/2} \leftrightarrow P_{3/2}$ transition while the other lasers at 397, 866 and 729 nm are on. The laser at 854 nm depopulates the $D_{5/2}$ that is populated by the laser at 729 nm. The laser power is reduced to a value where, even on resonance, the $D_{5/2}$ level is not pumped out completely.

can be seen in fig. 5.11, the laser at 854 nm restores the fluorescence when scanned across the resonance. For this scan, the laser intensity was reduced so that even on resonance the fluorescence was not completely restored, so that saturation broadening was avoided.

5.5. Optimisation of the laser parameters and the magnetic field

Sideband cooling requires the motional state of the ion to be in the Lamb-Dicke regime. Thus, the lasers at 397 and 866 nm have to be adjusted for optimum Doppler cooling. Experimentally, this is done by de-saturating the laser powers and detuning the frequency of the cooling laser towards longer wavelengths until the fluorescence has dropped to half the value emitted on resonance. The repumping laser is blue-detuned by several MHz, thus avoiding coherent population trapping. This setting yields a photon count rate of 10 kHz in the fluorescing state, which allows one to discriminate between the ion being in the $S_{1/2}$ or $D_{5/2}$ level with almost 100 % detection efficiency after collecting the fluorescence for 5 ms or less. In principle, the necessary detection time could be even halved by switching the frequency of the cooling laser to resonance before state detection is done. The frequency of the repumping laser at 854 nm is set on resonance by maximising the fluorescence rate while the laser at 729 nm is switched on. The same technique is utilised for optimising the (narrow) focus of the laser at 729 nm. For that purpose, the repumping laser partially pumps out the metastable state. A drop in the photon scattering rate indicates an improved excitation rate to the $D_{5/2}$ level. For the sideband cooling experiments, the frequency of the repumping laser is not an important parameter. While the task of pumping out the metastable level quickly can be accomplished at any laser frequency that is less than 100 MHz away from resonance, the sideband cooling efficiency in principle slightly improves if the quenching laser is red-detuned. However, this effect is extremely weak. Still, quenching the $D_{5/2}$ level by red-detuning the laser from resonance (and using a higher laser power instead) might be beneficial because of the reduced dependence of the quenching rate on a change in laser frequency (cf. eq. (3.21)).

Magnetic field

For preparation of the ion in one of the Zeeman ground states, the direction of the magnetic field has to be aligned with the direction of the circularly polarised laser at 397 nm. Three magnetic field coils serve to generate an arbitrary magnetic field of up to 10 G at the position of the ion. One of them produces the main contribution to the magnetic field, parallel to the σ^--polarised beam, the two others are used to compensate the transverse components of the static ambient magnetic field. Compensation is set by using only the σ-polarised beam for Doppler cooling and adjusting the coil currents until the fluorescence signal vanishes. The quality of the achieved optical pumping cannot be reliably judged by comparing the fluorescence rate of σ-polarised light with the rate achieved with linearly polarised light since also the Doppler cooling is reduced in the former case so that the ion is likely to scatter less photons[7]. Instead, a lower limit to the pumping efficiency of 95% or better is inferred from

[7] A comparison of the fluorescence rates might yield valid results when done in a more elaborate scheme where a cooling beam and a probe beam are used. The cooling beam would have to be switched off for short time

the transfer efficiency of a π-pulse on the carrier of the $S_{1/2} \leftrightarrow D_{5/2}$ transition.

For the magnetic field strength, a conflict arises between the desire to use a strong magnetic field for a wide splitting of the Zeeman components of the $S_{1/2} \leftrightarrow D_{5/2}$ transition and the demand of Doppler cooling the ion to a low vibrational quantum number. A field of 4 G splits

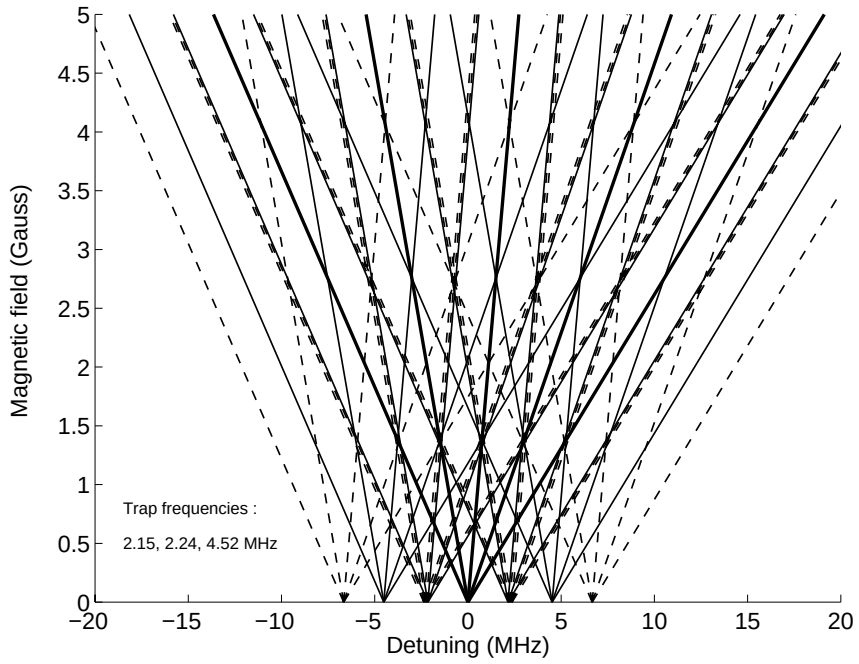

Figure 5.12.: Structure of the $S_{1/2} \leftrightarrow D_{5/2}$ transition as a function of the magnetic field. Solid lines indicate the resonance frequencies of the carriers and the first motional sidebands $\pm\omega_y, \pm\omega_z$, dashed lines the weaker transitions corresponding to the motional $\pm\omega_x, \pm(\omega_y \pm \omega_z)$ sidebands. This situation is encountered in the experiments where one of the radial modes always only weakly couples to the laser beam. The trap frequencies chosen for this example were (2.15, 2.24, 4.52) MHz. Occurrence of degenerate transition frequencies can be prevented by proper choice of the magnetic field strength (for example B=3.6 G).

adjacent Zeeman levels of the metastable state by 6.6 MHz, which is more than the separation of vibrational states. In the experiments, magnetic fields typically ranged between 3 G and 5 G, the suitable value depending on the trap frequencies. Fig. 5.12 serves to illustrate the problem. For given trap frequencies, magnetic field strengths have to be avoided that give rise to degenerate resonance frequencies of spectral lines belonging to different Zeeman transitions. Such degeneracies would not only complicate quantum state engineering, but also would reduce the number of sideband cooling cycles before optical pumping to the other Zeeman $S_{1/2}$ level occured (cf. section 3.2.2).

intervals so that the fluorescence could be probed by the other beam without changing the temperature of the ion. By gating the fluorescence detection and averaging over many such experiments, the pumping efficiency could be inferred.

6. Sideband cooling and coherent dynamics on the $S_{1/2} \leftrightarrow D_{5/2}$ transition

This chapter presents the main experimental results of this thesis. These are the preparation of the ion's motion in a pure quantum state by sideband cooling and first steps towards the goal of 'quantum state engineering' on an optical transition. Before experiments along these lines are undertaken, a thorough understanding of the spectral structure of the quadrupole transition is required. The laser frequencies necessary for excitation of the different Zeeman transitions and their motional sidebands are found by the spectroscopic investigations described in section 6.1. Moreover, excitation of the quadrupole transition also offers a means of assessing the ion's temperature after Doppler cooling. It turns out that Doppler cooling -if done appropriately - reduces the vibrational quantum numbers to values between 2 and 15 in accordance with the theoretical predictions for a two-level atom. Starting from these numbers, sideband cooling allows one to place the ion in the lowest quantum state with high probability. Section 6.4 discusses the cooling results as well as the cooling dynamics. Heating rates are measured by time-delayed temperature measurements after sideband cooling, and are found to be comfortably low (190 ms/phonon at $\omega_z = 4.5$ MHz). Therefore, heating rates present no obstacle to the coherent manipulations of the ion's quantum state described in section 6.5.1. In fact, it is the 1 ms coherence time that limits the maximum number of operations. The final section is devoted to experimental shortcomings that limit the fidelity of the operations achieved so far.

6.1. Spectroscopy on the $S_{1/2} \leftrightarrow D_{5/2}$ transition

The general measurement scheme for investigating the $S_{1/2} \leftrightarrow D_{5/2}$ transition has already been described in section 3.4.4. For recording spectra of the quadrupole transition, the most basic mode of pulsed spectroscopy is applied: After Doppler cooling the ion and preparing it in the $S_{1/2}(m = -1/2)$ level, a laser pulse at 729 nm is applied to the ion and the quantum jump technique is used to test whether the excitation was successful. The experiment is repeated a hundred times before the laser frequency at 729 nm is stepped to a new value.

6.1.1. Spectrum of a single ion

A spectrum of the quadrupole transition is routinely recorded every time experiments are done. To keep the recording time short, a pulse sequence of 5 ms duration is used. The laser is scanned at full light power (120 mW at the ion) across the $S_{1/2} \leftrightarrow D_{5/2}$ resonance with a resolution of 20-30 kHz. The resulting spectrum is reproduced in fig. 6.1.

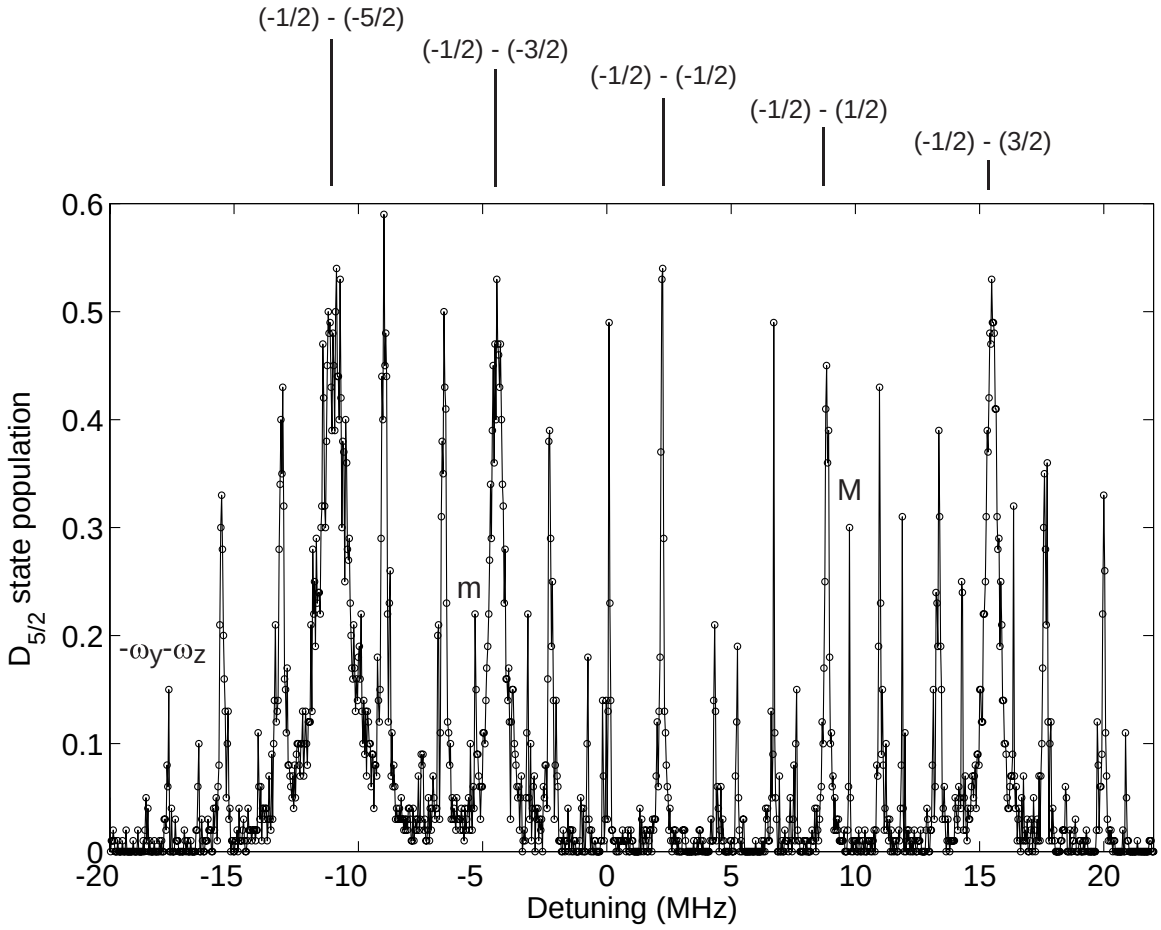

Figure 6.1.: Spectrum of the $S_{1/2} \leftrightarrow D_{5/2}$ transition of a single Ca^+ ion. A magnetic field of 4.1 Gauss spreads the spectrum over 40 MHz. Lines above mark the equidistantly spaced carrier transitions ($\Delta_{carrier} = 6.72$ MHz) which are flanked by motional sidebands separated by the trap frequencies $\omega_y = 2.14$ MHz and $\omega_z = 4.48$ MHz. The spectrum illustrates a situation that is unfavourable for sideband cooling and coherent manipulations since the separation $\Delta_{carrier}$ of adjacent carriers nearly equals the sum $\omega_y + \omega_z$ of radial and axial trap frequencies. The absorption strength rapidly decreases with rising sideband index (see for example the $-(\omega_y+\omega_z)$ sideband) indicating a satisfactory Doppler cooling efficiency. The first micromotional sideband of the $S_{1/2}(m = -1/2) \leftrightarrow D_{5/2}(m = -5/2)$ Zeeman component is marked by the letter M. Also visible are its motional sidebands as well as the -1^{st} micromotional sideband (m) of the $S_{1/2}(m = -1/2) \leftrightarrow D_{5/2}(m = +3/2)$ component. For the recording of the spectrum, the polarisation and beam direction were set for optimum exication of the $\Delta m = \pm 2$ Zeeman components. The laser detuning is given with respect to the $S_{1/2} \leftrightarrow D_{5/2}$ resonance frequency in a zero magnetic field.

The $S_{1/2} \leftrightarrow D_{5/2}$ transition frequency interpolated to zero magnetic field can be read off from the spectrum in terms of the AOM frequency (cf. fig. 4.11) as well as the magnetic field strength at the position of the ion.

The sideband structure is more clearly resolved by recording only selected spectral lines with a higher resolution. Fig. 6.2 shows the carrier of the $S_{1/2}(m = -1/2) \leftrightarrow D_{5/2}(m = -5/2)$

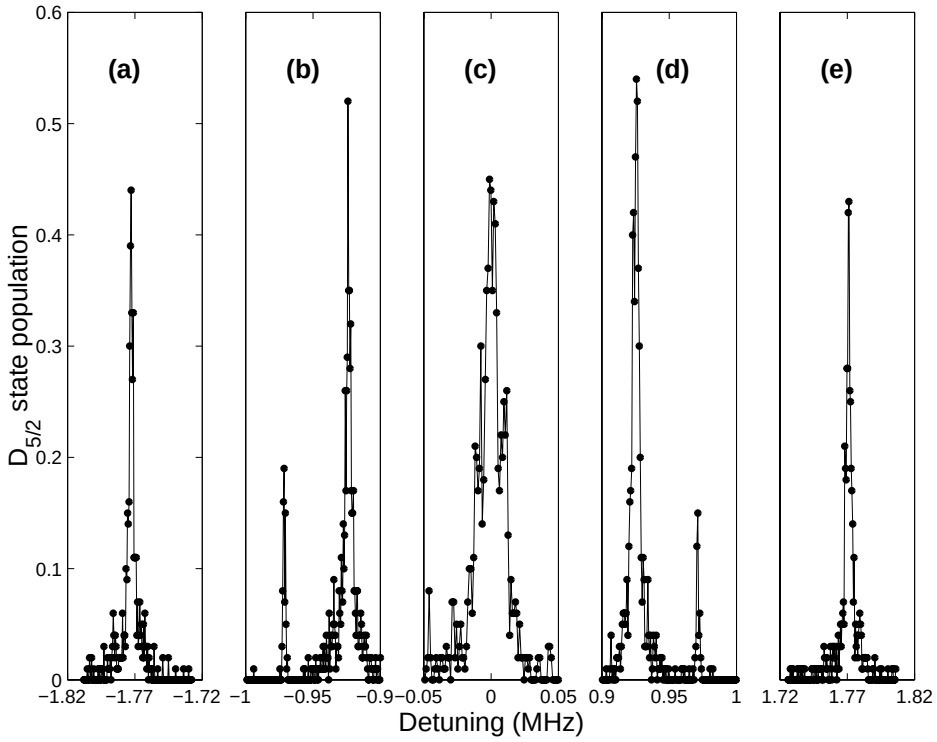

Figure 6.2.: Sideband spectrum of the $S_{1/2}(m = -1/2) \leftrightarrow D_{5/2}(m = -5/2)$ Zeeman component. (c) Carrier transition. (b+d) Radial sidebands ($\omega_y = 926$ kHz, $\omega_x = 971$ kHz). The x-oscillator couples to the laser only weakly. (a+e) Axial sidebands ($\omega_z = 1772$ kHz). The carrier transition was recorded at lower laser power.

Zeeman component together with the first order motional sidebands. For the recording of the carrier, the intensity of the excitation pulse had to be reduced. While the absorption on the ω_y and ω_z lines is about equal, it is noticeably reduced on the ω_x lines. This is due to a small overlap of the beam direction of the exciting laser with the x-oscillator, resulting in a much smaller Lamb-Dicke parameter. The laser essentially interacts only with the y- and z-oscillators. This situation is advantageous when either the y- or the z-oscillator is excited because in that case the laser appears to interact with a particle trapped in a two-dimensional potential. The influence of the vibrational state distribution in the third dimension on the y- or z-coupling strength is negligible. A similar situation is encountered when the other laser beam at 729 nm (cf. fig. 4.4) is used, with the roles of the x- and y-oscillators interchanged. If not otherwise noted, the laser beam that couples to the y- and z-oscillators is used for the experiments.

High-resolution scans of single spectral lines are interesting for several reasons. One motive for recording narrow spectral lines is in order to measure the drift of the laser frequency in time which is done by determining the centre frequency of a resonance line several times in the course of an hour (see fig. 4.11). In order to automatically compensate for the drift by changing the AOM frequency in time, the drift has to be known with an uncertainty of 1 Hz/s.

The linewidth of a narrow spectral line sets an upper bound to the linewidth of the exciting laser and allows an estimate of the short-term stability of the magnetic field and the trap frequency.

Fig. 6.3 is a recording of the $S_{1/2}(m = -1/2) \leftrightarrow D_{5/2}(m = -5/2)$ carrier transition, done

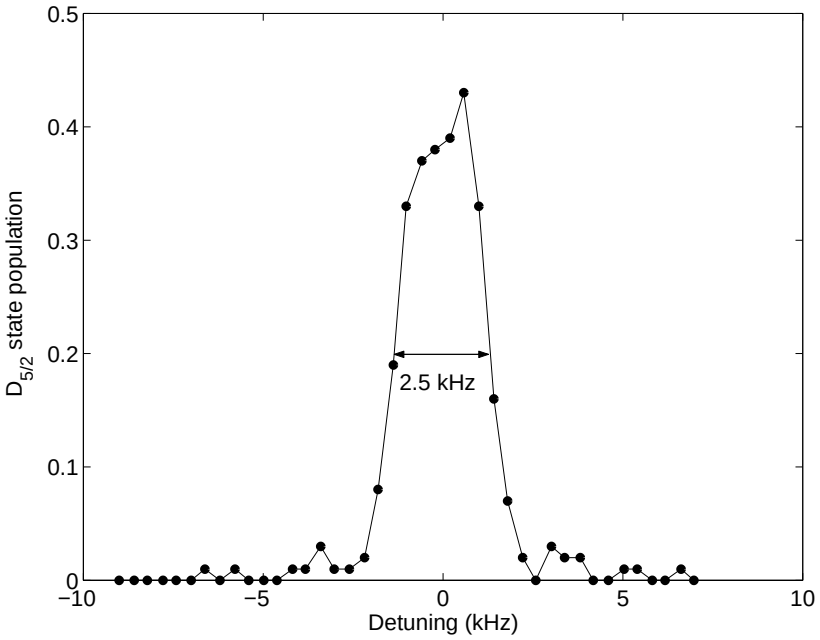

Figure 6.3.: High-resolution scan of the $S_{1/2}(m = -1/2) \leftrightarrow D_{5/2}(m = -5/2)$ carrier transition. For recording of a narrow line, a long excitation time τ was used ($\tau = 1$ ms) and the transition was de-saturated by reducing the laser power to $P_{729} = 0.4\ \mu$W.

with an excitation time of 1 ms and a light power of less than $0.5\,\mu$W. The timing of the excitation was synchronised to the phase of the power line in order to avoid line-broadening due to magnetic field fluctuations at 50 Hz. Typically, minimum linewidths of 2 kHz are measured, thus establishing an upper bound of 2 kHz to the laser linewidth. If the experiments are not carried out line-synchronously, magnetic field fluctuations at 50 Hz limit the $S_{1/2}(m = -1/2) \leftrightarrow D_{5/2}(m = -5/2)$ linewidth to 10 kHz. These periodic field variations can be mapped in the line-synchronous mode by measuring the resonance frequency as a function of the power line phase. As is shown in fig. 6.4, the field changes by as much as 0.6 μT, causing the resonance to shift by 17 kHz. It was checked that the magnetic field coils do not contribute to magnetic field noise. Periodic fluctuations of the magnetic fields also occur at frequencies in the range of 50 - 500 Hz that are no multiples of the line frequency. Measurements with a

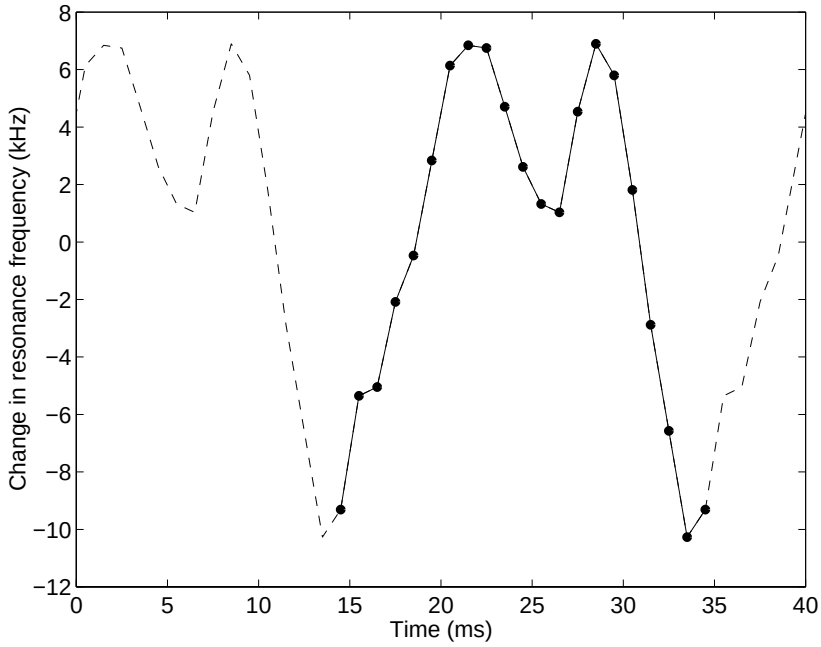

Figure 6.4.: Change of $S_{1/2}(m = -1/2) \leftrightarrow D_{5/2}(m = -5/2)$ carrier frequency as a function of excitation pulse timing. The timing is referenced to the phase of the power line. The peak difference of 17 kHz corresponds to a change in the magnetic field of 0.6 μT. The periodicity of the phenomenon is emphasised by the dashed line.

flux-gate magnetometer[1] yielded field amplitude variations of up to 0.1 μT. These magnetic field fluctuations could be noticeably reduced only by a μ-metal shield. However, the present setup is not well suited for easy screening. No screening is used in the present experiments, but attention is paid so as not to increase field fluctuations by inadvertently putting up (switching) power supplies close to the trap. Attempts to actively compensate for changes in the field proved to be unsuccessful owing to the difficulty of measuring the field that is to be compensated.

However, the minimum linewidth observed in the experiments is not caused predominantly by changes in the magnetic field. Other line-broadening mechanisms will be discussed in more detail in section 6.6.

6.1.2. Ramsey resonance experiments

Line-synchronous magnetic field fluctuations shift the $S_{1/2}(m = -1/2) \leftrightarrow D_{5/2}(m = -5/2)$ resonance frequency by as much as 2 kHz per millisecond. If the transition is coherently excited, with the excitation time being long, a shift of the resonance frequency during the excitation complicates the spectral line shape. Ramsey resonance experiments [102] offer the prospect of providing information about decoherence mechanisms without being significantly

[1] FLC 100, S. Mayer Meßgeräte.

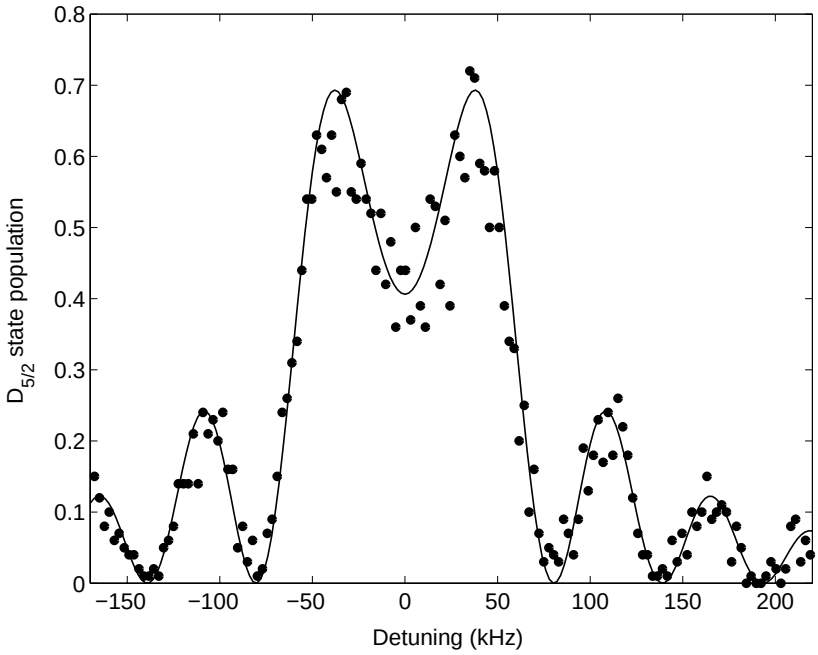

Figure 6.5.: Carrier transition excited by a pulse of 20 μs duration. The Rabi frequency is $\Omega = (2\pi)\,60$ kHz.

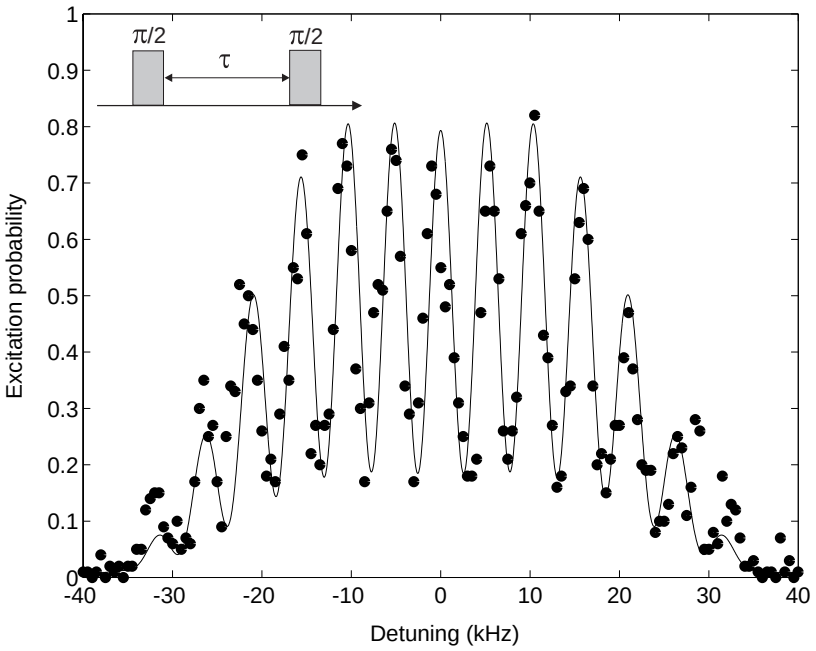

Figure 6.6.: Ramsey resonance experiment. Two $\pi/2$-pulses with a duration of 25 μs were applied. The pulse separation time was 200 μs. The solid curve is obtained by numerically computing the time evolution of the density matrix. It matches the experimental data optimally for a decay rate $\gamma = (2\pi)\,2.5$ kHz and a Rabi frequency $\Omega = (2\pi)\,10.9$ kHz which means that the $\pi/2$-pulse time was chosen a little bit too long. The decay is assumed to be purely transversal.

affected by these deterministic but only imprecisely known shifts. Instead of using a long weak single pulse, we excite the transition by two strong $\pi/2$-pulses separated by a delay time τ. The single pulses have a high Rabi frequency and are, therefore, not affected by small changes in resonance frequency. Their Rabi frequency and the pulse length determine the envelope of the line shape while the pulse separation sets the fringe contrast. Fig. 6.5 shows a single short pulse, though not a $\pi/2$- but rather a 2.4π-pulse. The outcome of a Ramsey-type excitation is displayed in fig. 6.6. In this experiment, the transition was excited by two 25 μs pulses separated in time by 200 μs. A decay rate of 2.5 kHz is deduced from the agreement between the data and a fit produced by numerically solving the time evolution of the density matrix with the decay rate and the Rabi frequency as adjustable parameters. The decay rate was assumed to be purely transversal, i.e. caused by fluctuations of the laser phase, the magnetic field etc..

6.1.3. Two-ion spectra

Spectra of the quadrupole transition have also been recorded by exciting a two-ion crystal. Fig. 6.7 shows that, in this case, the fluorescence signal is a three-valued signal and two thresholds have to be set to discriminate between the different outcomes of the experiment (0,1,2 ions fluorescing). The structure of two-ion spectra is noticeably more complicated than

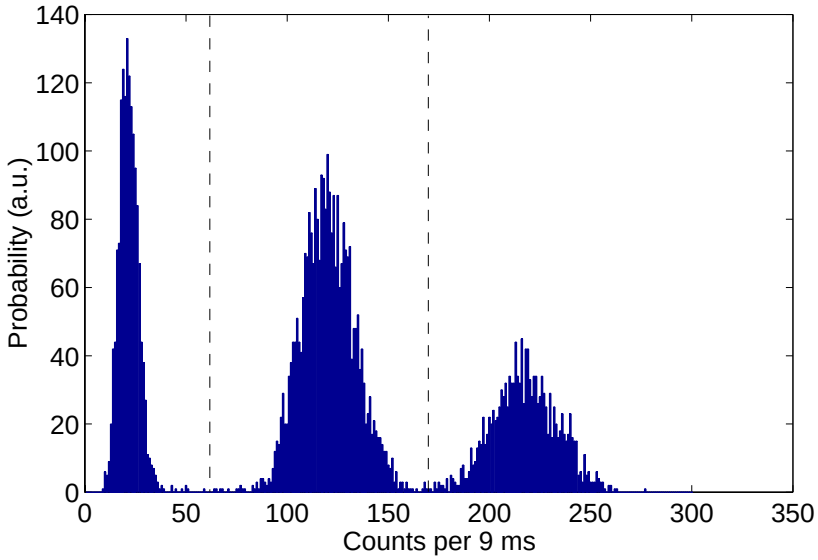

Figure 6.7.: Fluorescence histograms of a two-ion crystal excited on the quadrupole transition. Dashed lines indicate the thresholds used for fluorescence discrimination. At the time of the recording of this histogram, a misalignment of the AOM used for switching the laser at 854 nm prevented a perfect switching-off of the repumping light, causing a shortening of the $D_{5/2}$-lifetime. Evidence for the reduced lifetime (100 ms) can be seen in the region of the lower threshold. Those counts result from a decay of the non-fluorescing state during the detection time (cf. appendix A.2.2).

spectra recorded with a single ion as can be seen in fig. 6.8. There are now six different

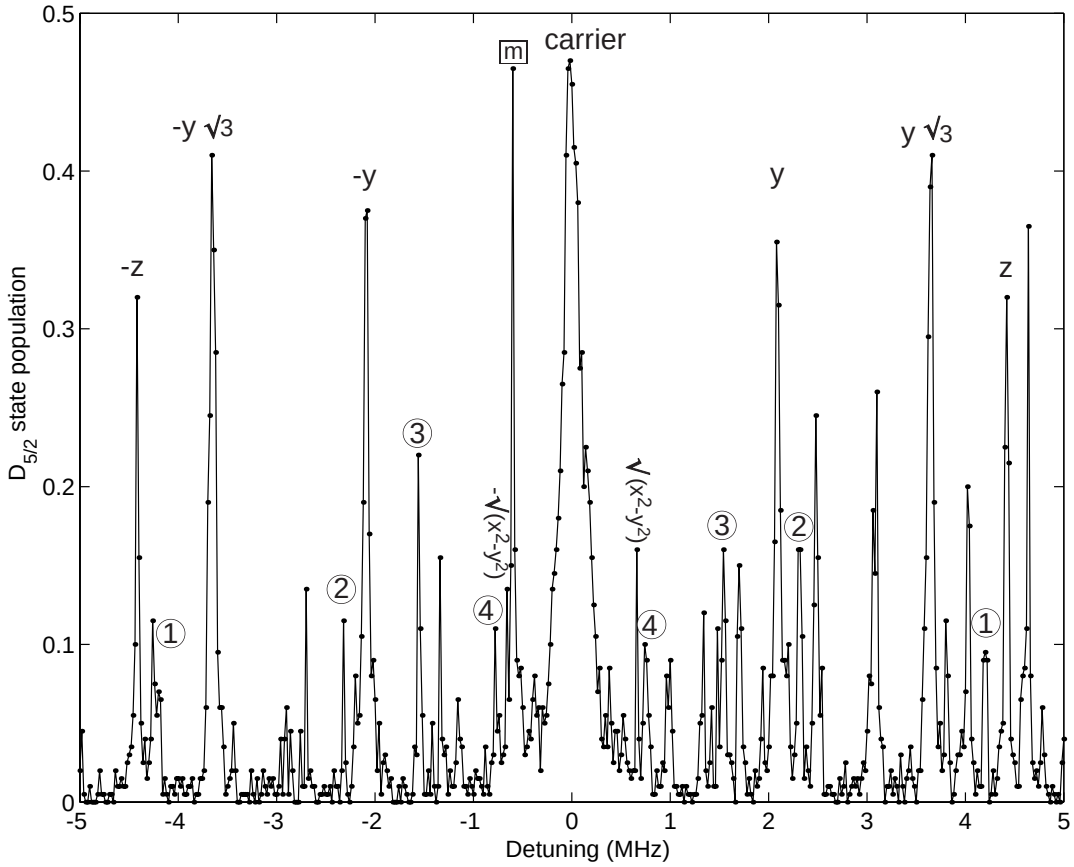

Figure 6.8.: Two-ion spectrum: $S_{1/2}(m=-1/2) \leftrightarrow D_{5/2}(m=-5/2)$ transition and motional sidebands. The ω_y, ω_z, $\sqrt{3}\omega_y$ and $[\omega_x^2 - \omega_y^2]^{1/2}$-sidebands are clearly visible. The ω_x-sidebands are occluded by the ω_y-sidebands. The $[\omega_z^2 - \omega_y^2]^{1/2}$-mode is either not excited by the laser or unresolved from the $\sqrt{3}\omega_y$-sideband. Numbered circles denote second order motional sidebands. (1) $2\omega_y$. (2) $\omega_z - \omega_y$. (3) $\sqrt{3}\omega_y - \omega_y$. (4) $\omega_z - \sqrt{3}\omega_y$. Spectral lines that are not symmetric with respect to the carrier belong to a different Zeeman transition. (m) indicates the -1st micromotional sideband of the $S_{1/2}(m=-1/2) \leftrightarrow D_{5/2}(m=+1/2)$ transition.

normal modes instead of three, and the number of second motional sideband frequencies nearly quadruples. In addition, the spectrum acquires micromotional sidebands since the Coulomb repulsion shifts the ions out of the RF zero-point. In fig. 6.8, motional sidebands of the $S_{1/2}(m=-1/2) \leftrightarrow D_{5/2}(m=-5/2)$ transition are identified by their symmetric spacing with respect to the carrier transitions. Four out of six normal modes show up in the spectrum. The resolution of the scan was not high enough to clearly resolve the radial centre-of-mass frequencies. Probably the $\sqrt{3}\omega_y$-mode ('stretch mode') and the $[\omega_z^2 - \omega_y^2]^{1/2}$-mode are also

too close in frequency to be individually resolved[2]. As a result of efficient Doppler cooling, the second motional sidebands have a much lower coupling strength. Finally, a number of spectral lines are visible that belong to other Zeeman transitions. Similar spectra are obtained

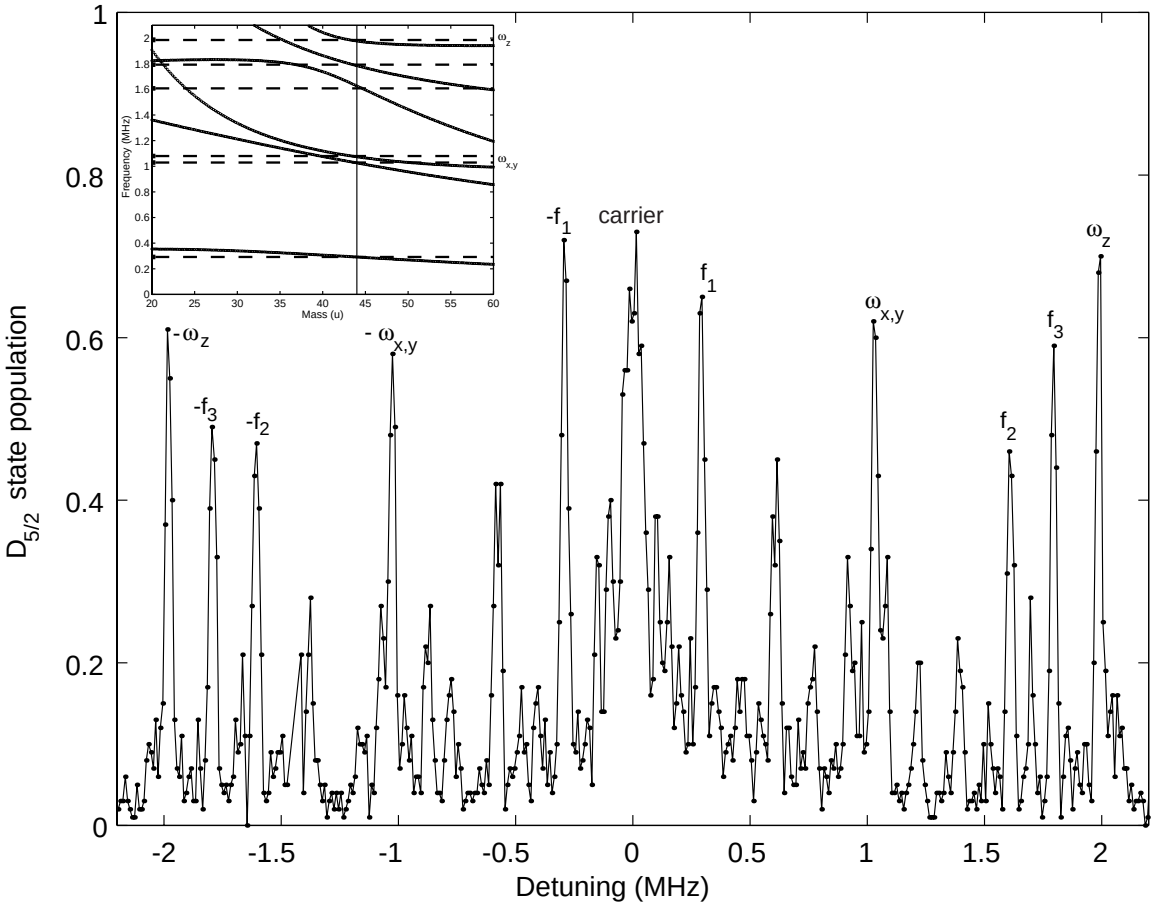

Figure 6.9.: Spectrum of a $^{40}Ca^{+}$ and an impurity ion. The $S_{1/2}(m = -1/2) \leftrightarrow D_{5/2}(m = -5/2)$ transition and its motional sidebands are displayed. The frequencies of the motional sidebands (292, 1028, 1080, 1608, 1794, 1985 kHz) suggest that the dark ion had a mass m= 43-44 u.

in the case of a two-ion crystal composed of a $^{40}Ca^{+}$ ion and an impurity ion, the sideband frequencies depending on the dark ion's mass. From the motional sideband distribution of the spectrum of fig. 6.9, it appears likely that the dark ion had a mass of either 43 or 44 u.

[2]In a trap where the axial frequency coincides with the doubled radial frequency, the mode frequencies are degenerate.

6.1.4. Ac-Stark shifts

It should be noted that the resonance frequency of a spectral line is dependent on the intensity of the laser due to non-resonant excitations on other spectral lines. Therefore, normal mode frequencies can be precisely inferred from the $S_{1/2} \leftrightarrow D_{5/2}$ spectra only at low light intensities. Frequency shifts of up to 50 kHz have been observed. Experimental evidence for ac-Stark shifts will be given in section 6.5.1.

6.2. Coherent dynamics after Doppler cooling

Once carrier and sideband frequencies have been measured, more information is gained by varying the length of the exciting pulse instead of its frequency. After Doppler cooling, the time evolution of the excited state population differs notably on the carrier and on the first sideband as can be seen from fig. 6.10 and fig. 6.11. On the carrier, the ion oscillates periodically between

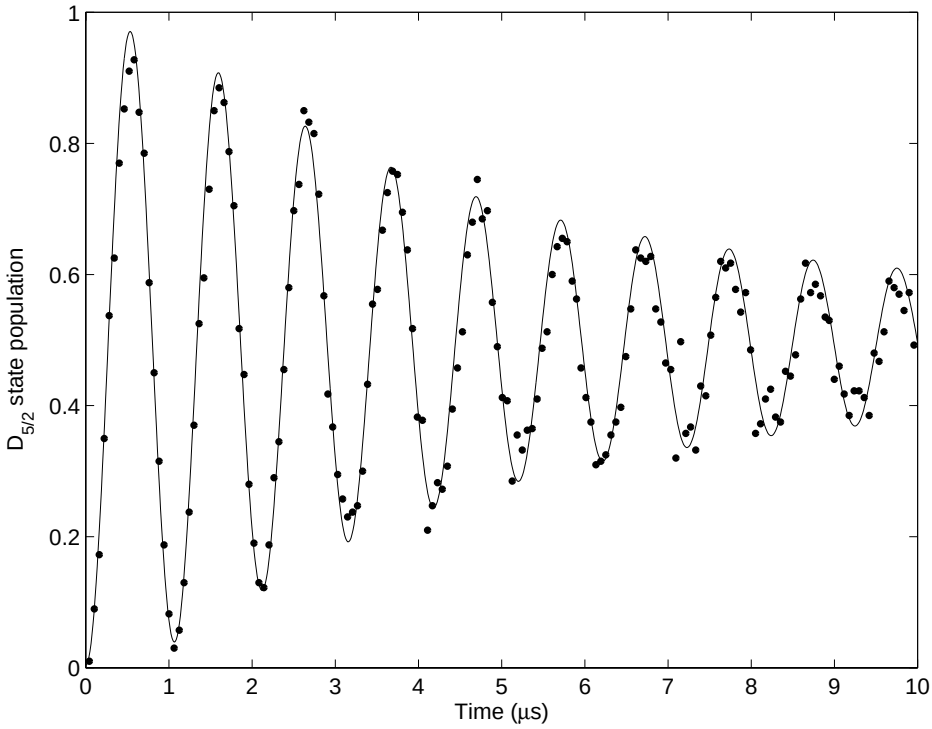

Figure 6.10.: Rabi oscillations on the carrier for a thermal motional state. The damping is caused by the weak dependance of the Rabi frequencies on the motional state. Each point represents 400 experiments.

the ground state and the excited state. The loss of contrast is attributable to a dephasing of the Rabi oscillations of populations in different vibrational states (cf. eq. (3.24)).

Excitation on the motional sideband yields a completely different time evolution. No Rabi oscillations are observed on the first motional sideband as long as the population is spread

over a range of levels whose Rabi frequencies differ significantly. Instead, the signal is strongly damped and quickly settles to a steady state. The solid curve is a fit assuming a thermal

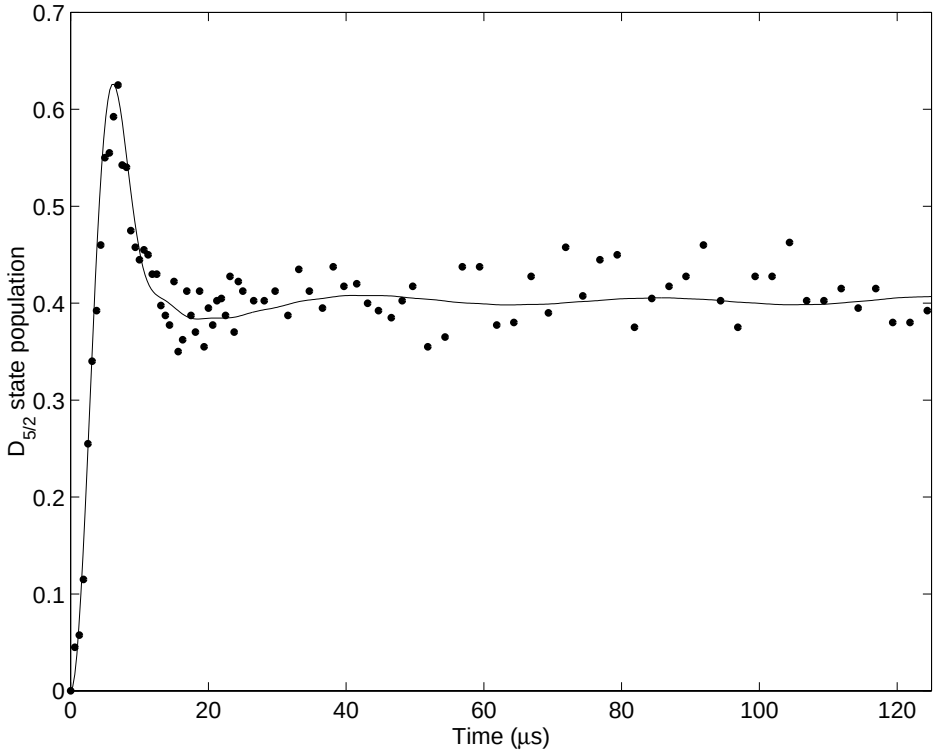

Figure 6.11.: Rabi oscillations of a thermal state with $\bar{n} = 18$ on the upper motional (radial) sideband ($\Omega_{0,0}/(2\pi) = 250$ kHz, $\eta = 0.07$). Each point represents 400 experiments.

distribution where the mean vibrational quantum number $\bar{n}$ and the detuning Δ have been adjusted to match the data. From the fit, a mean vibrational quantum number of $\bar{n} = 18$ is inferred.

6.3. Temperature measurements after Doppler cooling

Sideband cooling can be sucessfully applied only if a sufficiently low temperature is achieved after Doppler cooling. In the following paragraphs, different methods for evaluating the efficiency of Doppler cooling are discussed.

Carrier excitation

A convenient tool for optimising Doppler cooling is provided by the damping rate of Rabi oscillations on the carrier transition. In our experiments, the damping rate was minimised by appropriately setting the detuning and the intensity of the cooling lasers, as well as the

relative intensities of the two beams needed for cooling. The loss of contrast of Rabi oscillations on the carrier transition is governed by an effective mean vibrational quantum number $\hat{n} = \sum \eta_k^2 \bar{n}_k$ that depends on the mean occupation of all oscillators interacting with the laser beam (cf. appendix A.1). A high value of $\hat{n}$ results in a fast relaxation of the oscillation. Quantitative temperature measurements by determining $\hat{n}$ are possible only after cooling all but one oscillator to the motional ground state. Besides, the Lamb-Dicke parameter has to be known. As an example, fig. 6.20 shows Rabi oscillations on the axial sideband after sideband cooling. The loss of contrast is caused by the thermally distributed radial y-oscillator with $\bar{n}_y = 10$.

Sideband excitation

If the laser excites the first motional sideband, then observation of the time evolution $p_D(t)$ of the internal atomic state population offers the possibility to measure the mean occupation numbers of the oscillators individually, provided the Lamb-Dicke factor is known, since in the Lamb-Dicke regime, $p_D(t)$ is a function of $\eta^2 \bar{n}$. An example is provided by fig. 6.11 where a mean vibrational quantum number of $\bar{n} = 18$ was inferred from the shape of the excitation curve.

Comparison of excitation strengths

Other kinds of temperature measurements rely on a comparison of the excitation strengths at different laser frequencies. For example, if the first motional sideband and the carrier transition are incoherently excited with unsaturating laser power, the mean occupation number is related to the absorption strengths by $\bar{n} = p_D^{sideband}/(p_D^{carrier}\eta^2)$. Again, knowledge of the Lamb-Dicke parameter is required.

Yet another technique relates the mean vibrational quantum number to the occupation probability of the lowest oscillator state. This is done by a comparison of the absorption probabilities on the lower and upper motional sideband (see section 3.3.3). However, this method is useful only if $\bar{n} \leq 2$. At higher temperatures, a measurement on the second motional sidebands gives better results because it is sensitive to the population in the two lowest oscillator states. Fig. 6.12 illustrates the technique. From the absorption on the second lower and upper motional sidebands, it can be inferred that the axial oscillator at $\omega_z = (2\pi)$ 1740 kHz was cooled to a mixture of state with $\bar{n} = 5.3$ (1.0).

Doppler cooling results

All methods described above were applied in the experiments to judge the Doppler cooling efficiency. Normally, a vibrational occupation ranging between the Doppler limit and two times its value was observed after cooling had been optimised. The lowest value ever achieved was $\bar{n}_z = 2.5$ at a trap frequency $\omega_z = (2\pi)$ 4.5 MHz, in accordance with the Doppler limit $n_{Doppler} = 2.4$. Sub-Doppler temperatures [104] were never observed.

On the contrary, Doppler cooling sometimes resulted in temperatures far above the theoretical cooling limit. It was found that Doppler cooling critically depended on the ratio of the intensities of the beams at 397 nm (remember that two cooling beams are required for the setup described here). Certain intensity ratios resulted in non-thermally distributed

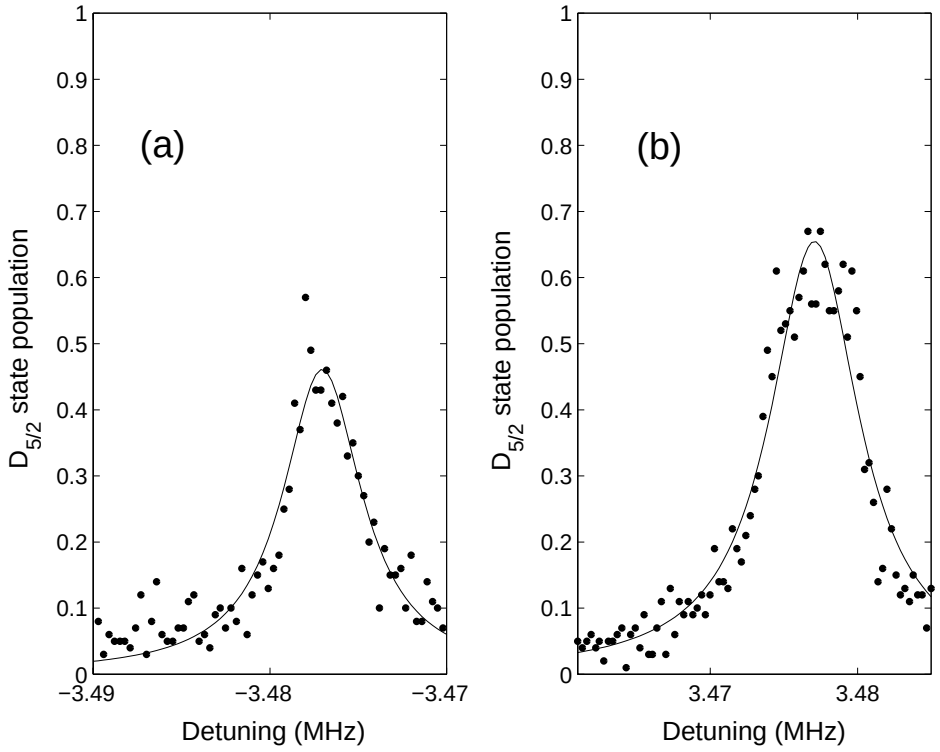

Figure 6.12.: Second axial sidebands ($\omega_z = (2\pi)$ 1740 kHz) after Doppler cooling. An asymmetry in the sideband strengths $x = p_D(-2\omega)/p_D(2\omega) = 0.7$ is clearly visible, giving a mean vibrational number $\bar{n} = x^{1/2}/(1 - x^{1/2}) = 5.3$ (1.0) [103].

states of vibration with mean values far above the Doppler limit. Evidence of this behaviour is presented in fig. 6.13. The time evolution of the atomic state on the carrier and on the first sideband is totally different from the usual evolution. While the oscillations on the carrier are rapidly damped, the sidebands exhibit fast and only weakly damped oscillations. This is possible only if the coupling strengths on the sideband are high and nearly equal for all populated oscillator states. The observed time evolution can be explained by assuming that the oscillator states have a distribution that is close to a Gaussian centred around $\bar{n} = 210$ with a half width $\langle(\bar{n}-n)^2\rangle^{1/2} = 130$ (see fig. 6.13 (d) and (e)). Furthermore, it has been found that the mean vibrational quantum number differed considerably for the radial oscillators. This conclusion rests on the observation that high contrast Rabi oscillations could be observed on the carrier when using one of the beams at 729 nm (sensitive to motion in the y- and z- mode) while excitation with the other beam (which coupled mainly to the x- and z-mode) led to a strongly damped Rabi oscillation signal.

To clarify the importance of the intensity and polarisation of the cooling laser beams for the cooling results, all cooling beam directions were equipped with half-wave plates so that the polarisation could be freely chosen. For a Doppler cooling configuration where two beams at 397 nm of equal intensity were used, the polarisations of both beams were systematically

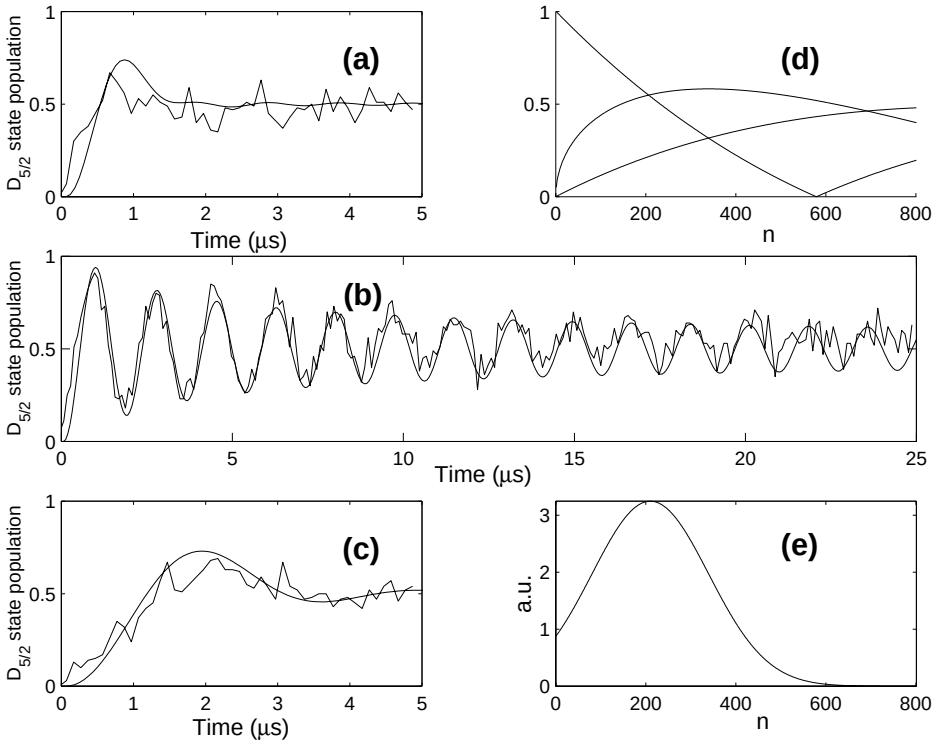

Figure 6.13.: Time evolution of the atomic state on the carrier (a) and the first (b) and second (c) motional sidebands after imperfect Doppler cooling. (d) shows the coupling strength of carrier and sidebands as a function of the vibrational quantum number in units of $\Omega_{0,0}$. (e) displays a distribution of states that closely reproduces the observed data. See text for further details.

varied and an effective vibrational quantum number was determined for the axial and one of the radial oscillators by measuring the loss of contrast of Rabi oscillations. By varying the polarisation of one of the beams, the mean quantum number could be changed between values of 15 and 250. The cooling results seemed to be independent of the relative polarisation of both cooling beams, so effects associated with standing waves play no role in the cooling process. Also, the polarisation of the repumping laser has no effect on the final vibrational state. For the experiments described in the remaining part of this chapter, a Doppler cooling configuration was chosen that resulted in mean vibrational quantum numbers close to the Doppler cooling limit for all three oscillators.

6.4. Sideband cooling experiments

After Doppler cooling the ion into the Lamb-Dicke regime, it can be put into a pure state (the $\langle n \rangle = 0$ state) by sideband cooling. The experimentally achieved fidelity of this process is discussed in the following section. A detailed account of the cooling results and the dynamics

of the cooling process is given. The period of time that the ion spends in the motional ground state in the absence of laser cooling is an important parameter in experiments aiming at coherent quantum state manipulations. Most of those experiments [64, 103] have been plagued by unexpectedly high motional heating rates. In our experiments, it is found that the observed motional heating rates present no obstacle to coherent manipulations. Heating occurs on a time scale that is long compared with the overall coherence time which is limited by other causes.

6.4.1. Sideband cooling results

The pulse sequence used for the Doppler cooling experiments is expanded by a sideband cooling step that puts the ion into the motional ground state of one or several oscillators. For this purpose, the cooling laser at 729 nm is tuned to one of the lower motional sidebands while at the same time the lifetime of the metastable level is quenched by the laser at 854 nm. The sideband is typically excited for several milliseconds at a Rabi frequency $\Omega_{0,1}$ of a few kilohertz. At the end of the sideband cooling step, population in the $D_{5/2}$ level is transferred to the $S_{1/2}$ level by the 854 nm repumping laser, and a short laser pulse of σ^--polarised light at 397 nm ensures that no population remains in the $S_{1/2}(m = +1/2)$ level.

The ground state occupation is determined by probing sideband absorption on the lower and upper motional sidebands immediately after the cooling pulse (see Eq. 3.23). To obtain optimum cooling results, the cooling laser power had to be reduced from its maximum value ($\Omega_{0,1} = 50$ kHz). The intensity of the quenching laser was optimised by minimising absorption on the lower motional sideband.

Sideband absorption spectra are shown in fig. 6.14 and 6.15.[3] In the upper figure, the radial y-oscillator at $\omega_y = (2\pi)$ 926 kHz was cooled to the ground state with 75 % probability, as can be inferred from the asymmetries of its sidebands, while the radial x-oscillator remained in a thermal state. The lower figure shows sideband cooling of the axial oscillator at a frequency of $\omega_z = (2\pi)$ 4.51 MHz. Here, the red sideband disappears completely after sideband cooling. The ground state occupation of $p_0 = 99.9\%$ is the best ever measured in our experiments. Sideband cooling results generally improve at high trap frequencies. A ground state occupation of up to 98% of the radial y-mode was achieved at $\omega_y = 2.0$ MHz, while no more than 90% were transferred to the ground state at $\omega_y = 920$ kHz. At $\omega_y = 700$ kHz, the ground state occupation was only 85%.

Several causes eventually contribute to the reduced cooling efficiency. Firstly, the initial distribution of motional states is broader, as Doppler cooling is less efficient at low frequencies since $\bar{n}_{Doppler} \propto \omega^{-1}$. Secondly, the Lamb-Dicke parameter is also inversely proportional to the trap frequency. Therefore, the Lamb-Dicke criterion is less strictly satisfied. However, the observed cooling limits are orders of magnitude higher than predictions based on theoretical models [76] (see also Eq. 3.20). Although lower than expected ground state occupation is partly due to motional heating of the ion (cf. subsection 6.4.3) during the detection time, it cannot fully account for the discrepancy between measured and expected results. For example, the dependence of cooling results on the intensity of the cooling laser must obviously have

[3] In these experiments, sideband cooling has been performed on the $S_{1/2}(m = +1/2) \leftrightarrow D_{5/2}(m = +5/2)$ transition, unlike most other experiments described in this thesis, where the $S_{1/2}(m = -1/2) \leftrightarrow D_{5/2}(m = -5/2)$ transition has been used.

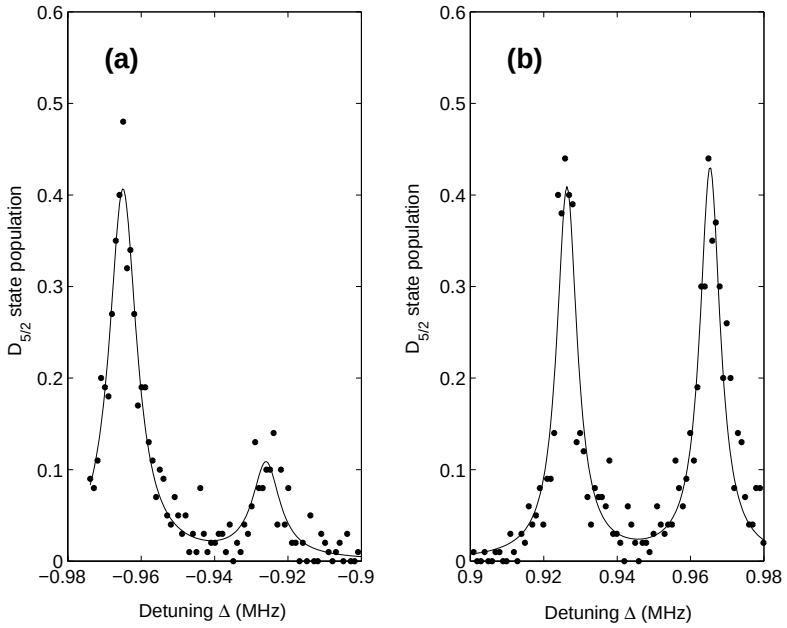

Figure 6.14.: Sideband absorption spectrum on the $S_{1/2}(m = +1/2) \leftrightarrow D_{5/2}(m = +5/2)$ transition after sideband cooling of the radial y-oscillator. The frequency is centered around (a) red and (b) blue sidebands at $\omega_y = (2\pi)$ 926 kHz and $\omega_y = (2\pi)$ 965 kHz. Comparison of the sideband heights yields a 75% ground state occupation for the radial y-mode. The radial x-mode remains uncooled.

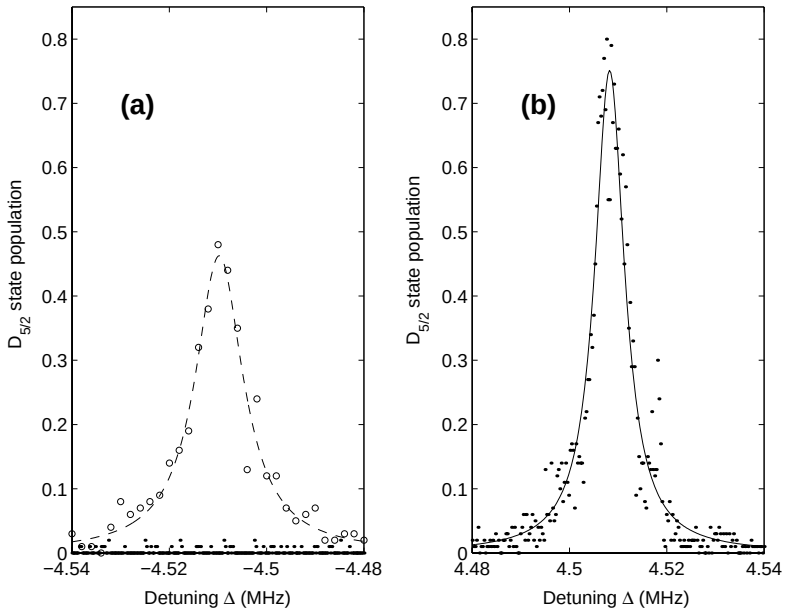

Figure 6.15.: Sideband absorption spectrum on the $S_{1/2}(m = +1/2) \leftrightarrow D_{5/2}(m = +5/2)$ transition after sideband cooling (full circles). The frequency is centered around (a) red and (b) blue sidebands at $\omega_z = (2\pi)$ 4.51 MHz. Open circles in (a) show the red sideband after Doppler cooling.

another reason.

The feasibility of cooling mixed states with high mean vibrational quantum number has not been systematically investigated. In one case, it was found that a state distribution with $\bar{n}_y \approx 80$ could be cooled to the ground state with approximately 90% probability within several milliseconds. In that case, the Lamb-Dicke parameter was $\eta_y = 0.045$, so that the condition $\eta_y^2 \bar{n}_y = 0.2 \ll 1$ was still satisfied.

If more than just one vibrational mode is to be cooled to the ground state, the cooling laser has to be cycled between the lower motional sidebands of the modes that should be cooled. The radial y-mode and the axial mode were simultaneously cooled to the ground state within 8 ms by tuning the laser to one of the sidebands for 200 μs, then switching the laser frequency to the other sideband for 200 μs, and so on. This procedure is more efficient than successively cooling first one and then the other mode because it avoids re-heating of the mode that was cooled first.

In order to cool all three vibrational modes of a single ion to the ground state, a second cooling beam has to be used in our setup to allow for cooling of the radial x-mode. Given a radial mode splitting of 50 kHz ($\omega_y = 1140,\ \omega_x = 1190,\ \omega_z = 2200$ kHz) it is possible to cool both radial modes without changing the frequency of the cooling laser. Using a scheme similar to the one described above and a total cooling time of 6 ms, the *pure* motional state $n_x = n_y = n_z = 0$ was realised with a probability slightly higher than 60%. This result could certainly be improved by enhancing the Doppler precooling so that the population in all motional modes is close to the Doppler limit. Increasing the cooling time, using a third cooling frequency and working at higher trap frequencies would also surely improve the result further.

6.4.2. Cooling dynamics

The cooling dynamics from the Doppler limit into the final state is studied by varying the cooling time τ_{cool} between zero and a maximum value, and determining the resulting ground state occupation from sideband absorption measurements. Fig. 6.16 shows $\langle n \rangle$ as a function of τ_{cool}. We find that initially $\langle n \rangle$ decreases rapidly, then it tends towards its finite final value. The decay constant, or cooling rate, determined by the data is 5 ms^{-1}. Taking into account our experimental parameters, both this value and the exponential behaviour are consistent with the expected 3-level dynamics during the sideband cooling process. The finite cooling limit is determined mainly by non-resonant excitation of the ion out of the ground state and heating in the subsequent spontaneous emission, and by heating out of the ground state during the detection process.

6.4.3. Heating rate measurements

In order to investigate motional decoherence of the system after sideband cooling, the system is left alone for a certain delay time t and is just interacting with the environment, i.e. with the surrounding electrodes and any possible perturbation acting on the motion of the ions. Then its mean vibrational quantum number is inferred from a measurement of the ground state population, assuming that the resulting state is thermal. The result of such a measurement is shown in fig. 6.17, where $\langle n_z \rangle$ is plotted as a function of the delay time t, yielding a heating

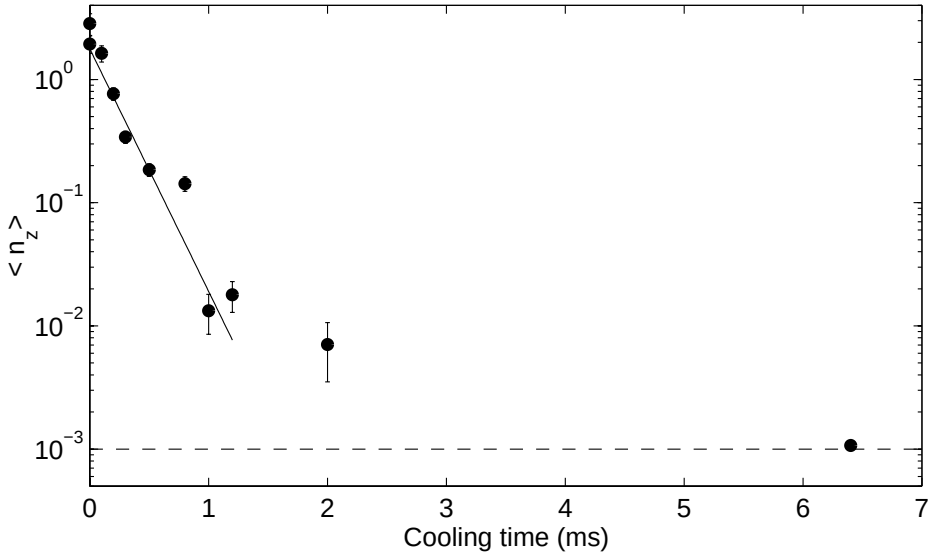

Figure 6.16.: Cooling dynamics: Mean phonon number vs. cooling pulse length deduced by sideband absorption measurements. The solid line assumes an initial exponential decay with 5 ms^{-1} decay constant. The dashed line indicates the detection limit set by off-resonant excitation to the D level.

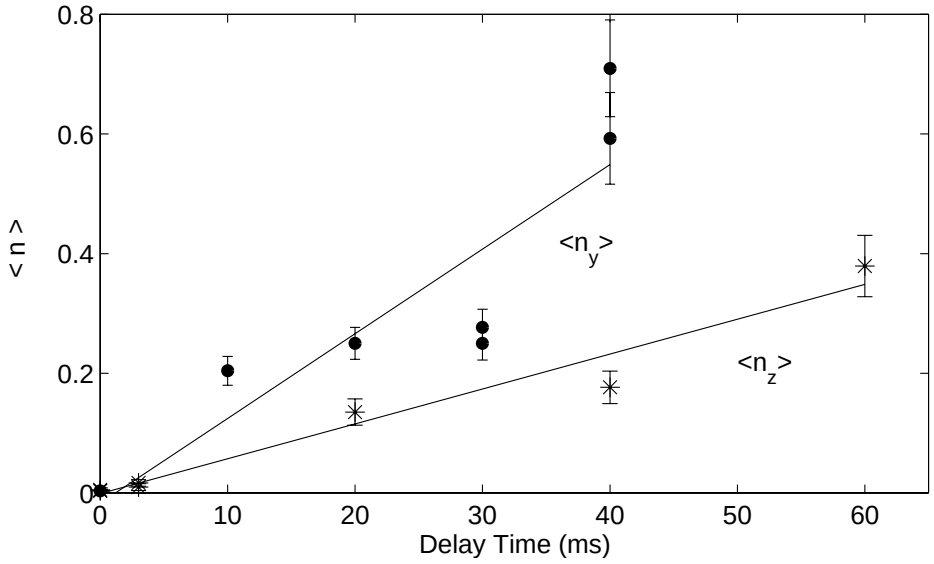

Figure 6.17.: Heating rate measurements for the axial and radial vibrational modes at 4 MHz and 1.9 MHz, respectively. Heating rates are 1 phonon in 190 ms for the axial and 1 phonon in 70 ms for the radial mode.

rate of $d\langle n\rangle/dt = 0.0053$ ms^{-1} (i.e. 1 phonon in 190 ms) at a trap frequency of $\omega_z = (2\pi)$ 4 MHz. For the radial y direction the heating rate was determined to be 1 phonon per 70 ms at $\omega_y = (2\pi)$ 1.9 MHz. The coherence time seems to be limited to approximately 1 ms by other mechanisms in the present setup (see section 6.6). Therefore, no substantial heating occurs within the time available for quantum state manipulations, in contrast to many experiments done by the ion trapping group in Boulder where heating rates of several quanta per millisecond were often observed. Heating is caused by fluctuating electric fields that couple to the ion's charge. However, the origin of these fields is currently under debate. For example, models that attribute the heating to fluctuations in the trap parameters or to Johnson noise in the trap electrodes are unable to account for experimentally observed heating rates [105–108]. Another possible source of electric field noise are fluctuating patch fields on the trap electrode surfaces [64, 103]. It might be possible to rule out some models by experimentally determining scaling laws that relate the observed heating rate to parameters that enter the model (i.e the secular frequency, the characteristic trap size and so on). Unfortunately, this approach is rendered difficult by the fact that many parameters can be changed only by opening the vacuum system and replacing the ion trap by a new one. From a comparison of all sideband cooling experiments existing to date, it seems that the heating rate strongly scales with the trap size. This finding is also supported by the experiment described here. Its trap size is one of the largest used for sideband cooling while the heating rates are among the smallest so far measured.

Prior to the measurements shown in fig. 6.17, much higher heating rates at 1.7 and 2 MHz were observed (one quantum per 4 millisecond) and found to be caused by a malfunctioning TTL logic chip close to the ion trap that emitted a broad noise spectrum centered around 2 MHz. A measurement at 1.1 MHz yielding a rate of one quantum per 12 ms might also have been affected by that noise source and cannot be compared to the results measured at higher frequencies after removing the corrupted chip.

6.4.4. Sideband cooling of two ions

Sideband cooling of one of the normal modes of a two-ion crystal proceeds completely analogously to the case of a single ion. The cooling laser is tuned to the lower motional sideband of the mode to be cooled and, by probing the absorption on the lower and upper motional sideband, the ground state probability is measured. Fig. 6.18 displays sideband cooling results for the cooling of the radial (y) and axial center-of-mass modes as well as the stretch mode. For the axial COM mode at $\omega_z = 4.44$ MHz, more than 98% ground state occupation is achieved. The stretch mode oscillator, having a frequency $\omega_{y\sqrt{3}} = 3.66$ MHz, is cooled to the ground state with more than 96% probability and the ground state occupation of the radial COM mode ($\omega_y = 2.1$ MHz) is approximately 96%. These results were obtained in three consecutive experiments.

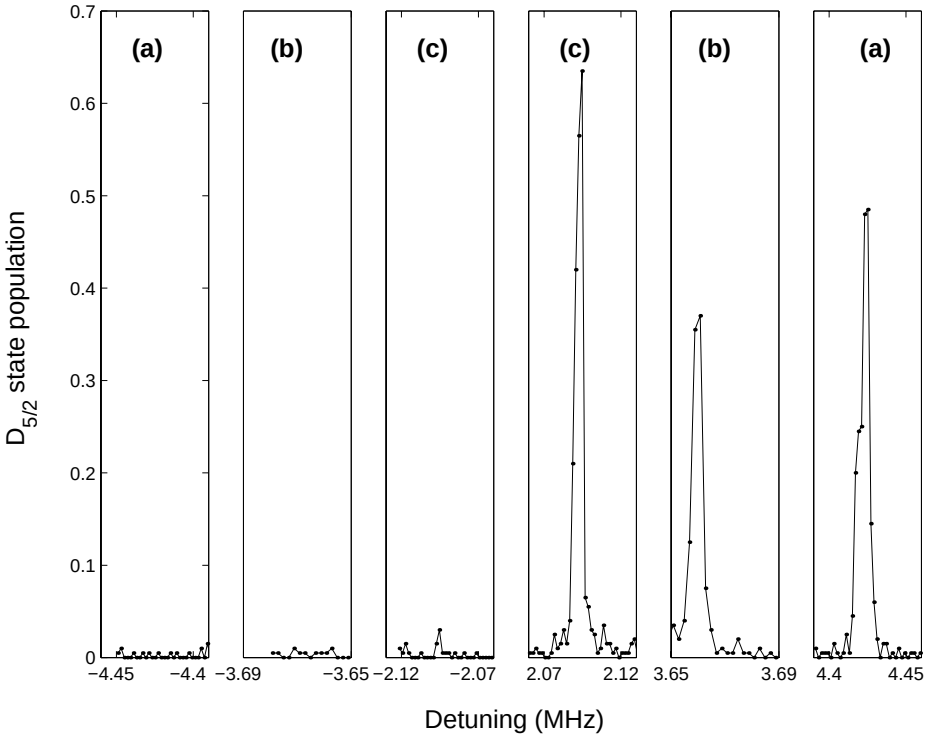

Figure 6.18.: Sideband cooling of several modes of a two-ion crystal. Shown are the lower and upper motional sidebands of (a) the axial mode ($\omega_z = 4.44$ MHz), (b) the stretch mode ($\omega_{y\sqrt{3}} = 3.66$ MHz) and (c) the radial mode $\omega_y = 2.1$ MHz. Ground state occupations after one-dimensional sideband cooling are $\langle p_0 \rangle_z \geq 98\%$, $\langle p_0 \rangle_{y\sqrt{3}} \geq 96\%$ and $\langle p_0 \rangle_y \approx 96\%$, respectively.

6.5. Coherent dynamics after sideband cooling

6.5.1. Rabi oscillations

After sideband cooling the ion to the ground state, Rabi oscillations are not only observed when exciting the transition on the carrier but also on the upper sidebands. Rabi oscillations on the carrier and the radial-y sideband have been excited in fig. 6.19 after preparing the y-mode in the lowest oscillator state. The contrast of the oscillations is notably higher than in fig. 6.10 since now only the z-oscillator is in a thermal state causing a reduction in contrast. The radial-y sideband is excited at only a fortieth of the laser intensity used for carrier excitation in order to avoid non-resonant carrier excitation (cf. subsection 6.5.2). By comparing the Rabi frequencies on the carrier and on the sideband, the Lamb-Dicke factor can be calculated (i.e. the angle ϕ between the k-vector of the laser and the direction of oscillation). From the data in fig. 6.19, a Lamb-Dicke factor of $\eta_y = 0.045$ is calculated for a trap frequency $\omega_y = (2\pi)\ 1850$ kHz, corresponding to an angle $\phi = 52°$.

If ground state cooling is less efficient, excitation on the blue sideband results in a more

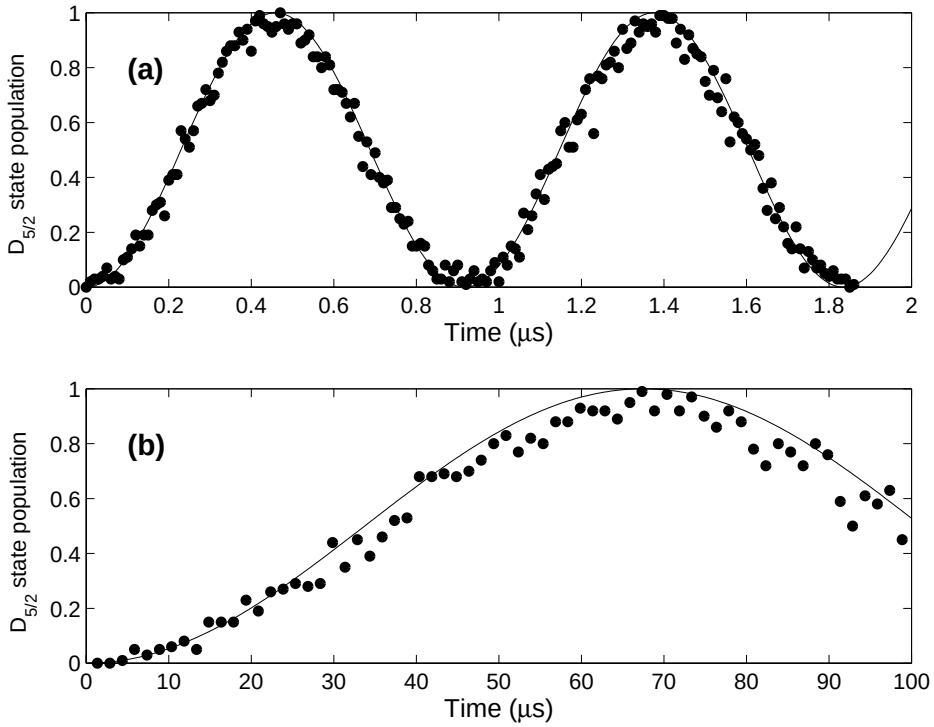

Figure 6.19.: Rabi oscillations on the carrier (a) and on the upper motional sideband of the radial y-mode ($\omega_y = (2\pi)1850$ kHz) (b) after sideband cooling. While the carrier was excited at full light intensity, the intensity was reduced by a factor of 40 for (b) in order to avoid non-resonant excitation on the carrier transition. The Lamb-Dicke factor η_y=0.045 can be deduced from the ratio of the Rabi frequencies and is found to agree with the expected value for an angle of 52°.

complicated evolution of the excited state population $p_D(t)$. An example is shown in fig. 6.20 where the Rabi oscillations appear to be amplitude-modulated. This kind of signal is expected from a distribution where the ion is in the ground state with 90% probability and in the second lowest vibrational state in 10% of the cases[4]. The overall loss of contrast again results from the thermally distributed other oscillator.

6.5.2. Non-resonant excitations

When the $S_{1/2} \leftrightarrow D_{5/2}$ transition is excited on the sideband at high laser power, the transfer efficiency to the excited state is affected by non-resonant excitation of the carrier transition. If the Rabi frequency on the carrier transition is no longer small compared with the trap frequency, a significant amount of the population is transferred to the excited state without any change in the vibrational quantum number. The data shown in fig. 6.21 were

[4]Since the ratio of Rabi frequencies in the two lowest vibrational states is $\Omega_{2,1}/\Omega_{1,0} = \sqrt{2} \approx 3/2$, the second minimum of $p_D(t)$ is less pronounced than the following one.

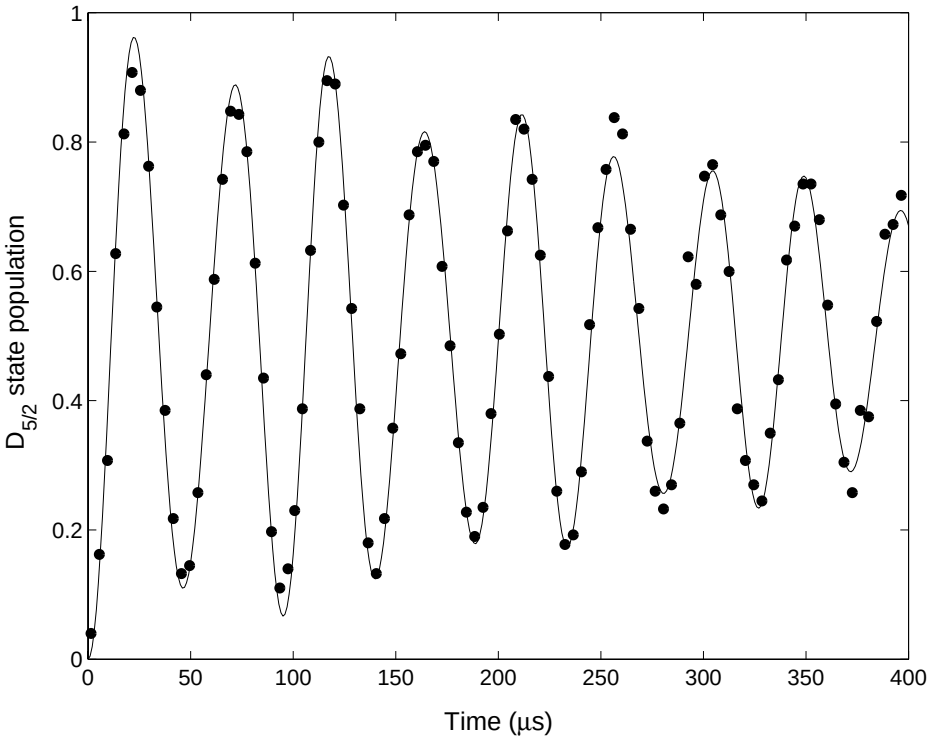

Figure 6.20.: Rabi oscillations on the axial sideband after sideband cooling. The loss of contrast is caused by the thermally distributed radial y-oscillator. The beat signal arises from the difference in Rabi frequencies of the $|n = 0\rangle$ and $|n = 1\rangle$ populations. From the fit, mean vibrational quantum numbers of $\bar{n}_y = 10$ and $\bar{n}_z = 0.1$ are inferred. Each data point represents the average of 400 experiments.

recorded by preparing the ion in the ground state of the y-mode ($\omega_y = (2\pi)$ 1850 kHz) and subsequently exciting the upper motional y-sideband at full laser power resulting in a Rabi frequency $\Omega_{0,0} = (2\pi)$ 1090 kHz on the carrier and $\Omega_{1,0} = (2\pi)$ 48 kHz on the sideband. The laser was red-detuned from the sideband resonance by $\delta_{exp} = (2\pi)$ 250 kHz in order to compensate for light shifts caused by excitation of the carrier transition and of the dipole transitions $D_{5/2} \leftrightarrow P_{3/2}$, $S_{1/2} \leftrightarrow P_{1/2}$ and $S_{1/2} \leftrightarrow P_{3/2}$. The non-resonant carrier excitation is clearly visible on top of the sideband excitation signal. The experimental data can be fitted by numerically solving the Schrödinger equation in the truncated basis of the 4-level system consisting of the $|S_{1/2}, n = 0\rangle$, $|D_{5/2}, n = 0\rangle$, $|S_{1/2}, n = 1\rangle$ and $|D_{5/2}, n = 1\rangle$ states. Three parameters enter the calculation that were independently measured: The Rabi frequency on the carrier transition, the Lamb-Dicke parameter η_y and the trap frequency. The detuning of the exciting laser field is varied for optimum contrast, and a good agreement between the data and the numerical simulation (lower plot: dashed line) is found for a laser detuning $\delta_{th} = (2\pi)$ 375 kHz. The discrepancy of 125 kHz between δ_{th} and the experimentally observed value is attributed to light shifts due to the dipole transitions. Exactly the same difference was noted for sideband excitation at $\delta_{exp} = 0$ kHz at the same laser power. This interpretation

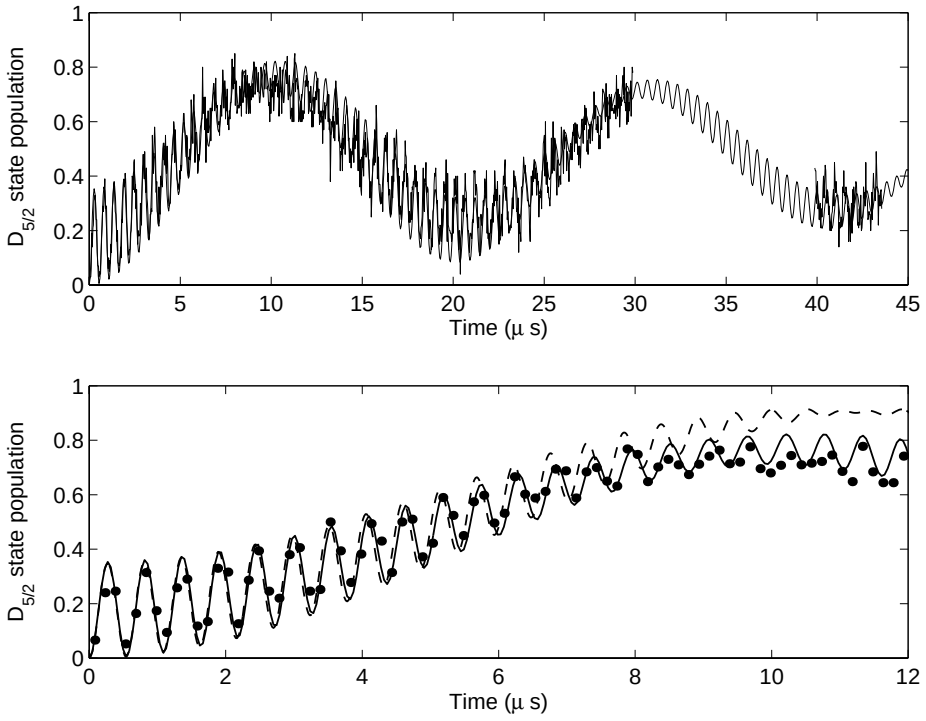

Figure 6.21.: Rabi oscillations on the blue radial-y sideband ($\omega_y = (2\pi)$ 1850 kHz) at full laser excitation power $\Omega = (2\pi)$ 1090 kHz. On top of the Rabi oscillations at $\Omega_{1,0} = (2\pi)$ 48 kHz a small and fast oscillation appears that is caused by non-resonant excitation of the carrier transition. The lower plot shows the beginning of the sideband oscillations. Here, each data point represents 500 individual experiments. See text for a detailed description of the numerical simulations.

is confirmed by a theoretical estimation of the expected light shift due to dipole transitions giving a value of approximately 100 kHz.

Unfortunately, a closer look at the light shift caused by non-resonant $S_{1/2} \leftrightarrow D_{5/2}$ excitation reveals that it is not constant, but depends on the vibrational quantum numbers of the other oscillator modes. The carrier transition strength decreases with increasing axial vibrational number and induces a light shift given by (cf. eq. (3.12))

$$\delta_n^{(z)} = -\frac{\Omega_{n,n}^2}{2\omega_y} \approx -\frac{\Omega^2}{2\omega_y}(1 - 2\eta_z^2 n_z) \ ,$$

(if $\Omega \ll \omega_y$) so that for a thermal distribution the standard deviation of the light shift is given by

$$[\langle(\delta_n^{(z)} - \langle\delta_n^{(z)}\rangle)^2\rangle]^{1/2} \approx \frac{(\eta_z\Omega)^2}{\omega_y}[\langle(n_z - \langle n_z\rangle)^2\rangle]^{1/2} \approx \frac{(\eta_z\Omega)^2}{\omega_y}\bar{n}_z \ . \tag{6.1}$$

The other radial (x) mode influences the transition frequency of the radial (y) mode by a different mechanism. In spite of the small Lamb-Dicke parameter it induces a light shift

because of the near degeneracy of the radial transition frequencies ($\delta_x - \delta_y = (2\pi)\,75$ kHz at $\omega_y = (2\pi)\,1925$ kHz). Therefore, the sideband transition shifts the (y) resonance frequency by

$$\delta_n^{(x)} = \frac{(\eta_x \Omega)^2}{2(\omega_x - \omega_y)} n_x \ ,$$

and the spread of the light shifts is again proportional to the mean occupation number :

$$[\langle (\delta_n^{(x)} - \langle \delta_n^{(x)} \rangle)^2 \rangle]^{1/2} \approx \frac{(\eta_x \Omega)^2}{2(\omega_x - \omega_y)} \langle n_x \rangle \ . \tag{6.2}$$

Each vibrational quantum in the (z) mode shifts the $|S_{1/2}, n_x, 0_y, n_z\rangle \leftrightarrow |D_{5/2}, n_x, 1_y, n_z\rangle$ resonance frequency by $(2\pi)\,1.0$ kHz. Similarly, the (x) mode causes a shift of $(2\pi)\,0.8$ kHz per vibrational quantum if $\eta_x = 0.01$.

To model this situation, the Schrödinger equation is solved for different x-oscillator occupations and the results are averaged over a thermal distribution. The observed experimental data are in fairly good agreement with the numerical simulation (solid line in fig. 6.21) if a 20 kHz spread in light shifts is assumed. Such a spread could result from a mean vibrational quantum number of $\bar{n}_x = 25$ and $\eta_x = 0.01$.

6.5.3. Generation of Fock states

The detrimental effect of light shifts on the contrast of Rabi oscillations can be kept low by exciting the ion on the blue axial sideband after cooling the axial oscillator as well as the radial (y) oscillator to the ground state. This scheme allows recording of high contrast Rabi

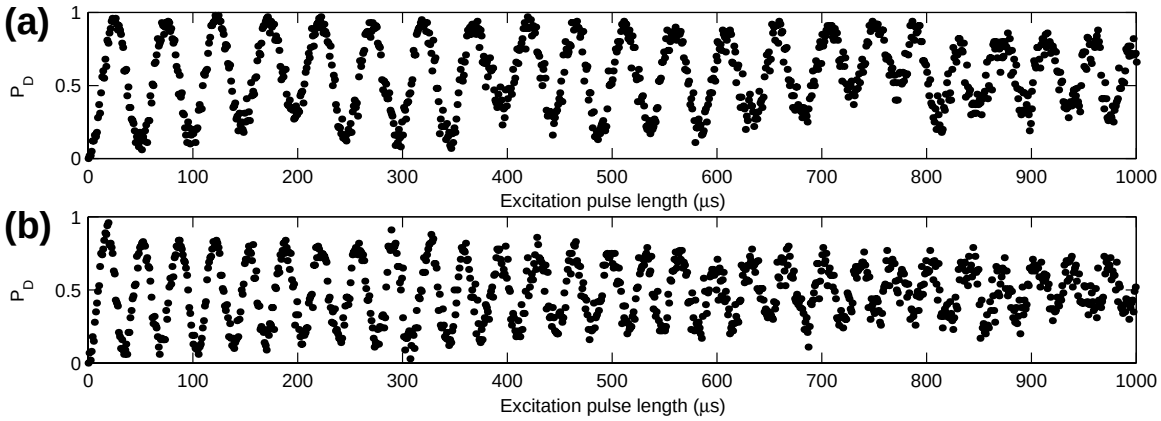

Figure 6.22.: Rabi flopping dynamics of an ion initially prepared in the (a) $|n = 0\rangle$ and (b) $|n = 1\rangle$ Fock state. The ratio of the Rabi frequencies $\Omega_{2,1}/\Omega_{1,0} \approx 1.43$ is close to the expected value of $\sqrt{2}$. See text for the preparation of the initial states.

oscillations. In fig. 6.22 (a), the Rabi flopping behavior is shown where the ion was initially in the $|S_{1/2}, n_z = 0\rangle$ state. This scan was recorded at a trap frequency of $\omega_z = (2\pi)\,1700$

kHz. The lower trace (b) shows the $D_{5/2}$ occupation for a given interaction time τ on the blue sideband transition where the ion was initially prepared in the $|n_z = 1\rangle$ Fock state. For the preparation of the $|S_{1/2}, n_z = 1\rangle$ state, the ion is cooled to the $|S_{1/2}, n_z = 0\rangle$ state before a π - pulse is applied on the axial blue sideband and followed by an optical pumping pulse at 854 nm to transfer the population from $|D_{5/2}, n_z = 1\rangle$ to $|S_{1/2}, n_z = 1\rangle$. The Rabi flopping behavior allows one to analyse the purity of the initial state and its decoherence. For the $|n_z = 0\rangle$ state, Rabi oscillations at $\Omega_{1,0} = (2\pi)\,21$ kHz are observed with high contrast indicating that coherence is maintained for times well above 1 ms. The $|n_z = 1\rangle$ state exhibits Rabi oscillations with a similarly high contrast, now at $\Omega_{2,1} = (2\pi)\,30$ kHz. The ratio of the Rabi frequencies agrees with $\Omega_{2,1}/\Omega_{1,0} = \sqrt{2}$ within 1%. The Fourier transform of the flopping signals yields directly the occupation probabilities for the contributing Fock states [2, 60], and allows one to calculate the purity of the prepared and manipulated states. For the 'vacuum' state $|n_z = 0\rangle$, $p_0 = 0.89(1)$ is obtained with impurities of $p_1 = 0.09(1)$ and $p_{n_z \geq 2} \leq 0.02(1)$. For the Fock state $|n_z = 1\rangle$, the populations are $p_0 = 0.03(1)$, $p_1 = 0.87(1)$, $p_2 = 0.08(2)$ and $p_{n_z \geq 3} \leq 0.02(1)$. The measured fidelity $F = Tr(\rho_{exp}\rho_{ideal}) \approx 0.9$ agrees well with our expectation. Here, ρ_{exp} (ρ_{ideal}) is the density operator describing the achieved (desired) result of the experiment. Note that the Rabi flopping data were taken with less efficient cooling (lower trap frequency), and that the number state occupation from the Fourier analysis is consistent with the temperature determined by sideband measurements.

The contrast of the Rabi flopping decays to 0.5 after about 20 periods. Therefore, it is reasonable to expect that unitary manipulations equivalent to 40 π pulses on the sideband can be executed with a fidelity of 0.5 in the present system. The observed decoherence is consistent with the independently measured values of the laser linewidth, (below 1 kHz), the laser intensity fluctuations (below 3%) and ambient magnetic field fluctuations (line shifts of $\pm$10 kHz at 50 Hz frequency).

6.5.4. Two-ion results

If a two-ion crystal is excited by the laser at 729 nm, the coupling strength of the interaction is normally different for both ions, giving rise to a beat signal in the excited state population. The unequal coupling strengths arise either from different light intensities at the positions of the ions or from a difference in the micromotion amplitudes of the ions. The latter explanation appears to be the more likely cause in our experiment, since the separation of the ions is small compared with the waist of the exciting laser beam. Fig. 6.23 shows the excitation probability as a function of the interaction time if the ions are excited on the carrier of the transition. In the upper trace, the ratio of Rabi frequencies is $\Omega^{(1)}_{0,0}/\Omega^{(2)}_{0,0} \approx 12/11$. The lower trace was recorded 100 minutes after the upper ones and shows a ratio of $\Omega^{(1)}_{0,0}/\Omega^{(2)}_{0,0} \approx 8/7$, indicating that either the position of the laser beam or stray electric fields changed in time.

The Rabi frequency can be made equal on both ions by slightly altering the compensation voltages, thereby equalising the ac-Stark shift experienced by the ions. In fig. 6.24, the axial COM mode of the ions was cooled to the ground state before the ions were excited on the corresponding upper motional sideband. Unfortunately, the contrast of the Rabi oscillations quickly deteriorates and for long interaction times the excited state population appears to approach a value below 1/2, although the detuning had been optimised. Presently, it seems likely that, due to less efficient Doppler cooling, the non-resonant interactions discussed in

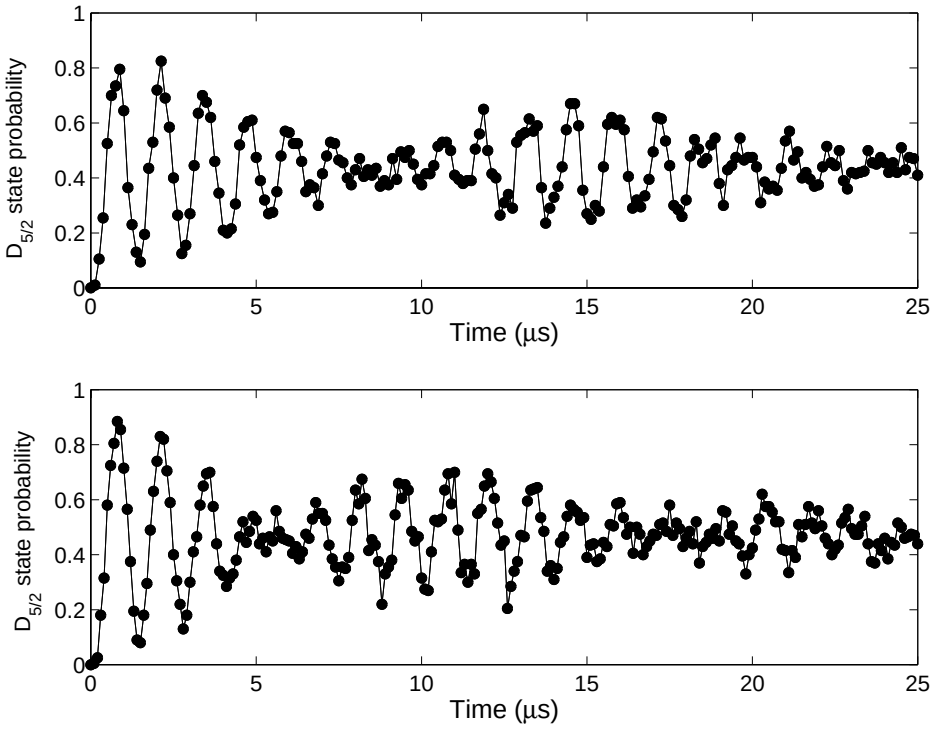

Figure 6.23.: Rabi oscillations of two ions on the carrier transition. The Rabi frequencies are slightly different for both ions, because of either different light intensities at the positions of the ions, or a different modulation index of micromotion. Therefore, a beat signal is seen in the excited state occupation averaged over both ions. The lower trace was recorded 100 minutes after the measurement of the upper trace and shows that the ratio of Rabi frequencies also changed in time. The laser detuning was not optimally chosen. Therefore, the oscillations are not centered around 0.5.

subsection 6.5.2 lead to a stronger degradation of the signal than in the case of a single trapped ion.

6.6. Coherence-limiting processes

This subsection summarises the processes that limit the coherence time to about a millisecond and the maximum number of coherent excitations to approximately 30 in our present experimental setup. The importance of the different mechanisms is discussed below.

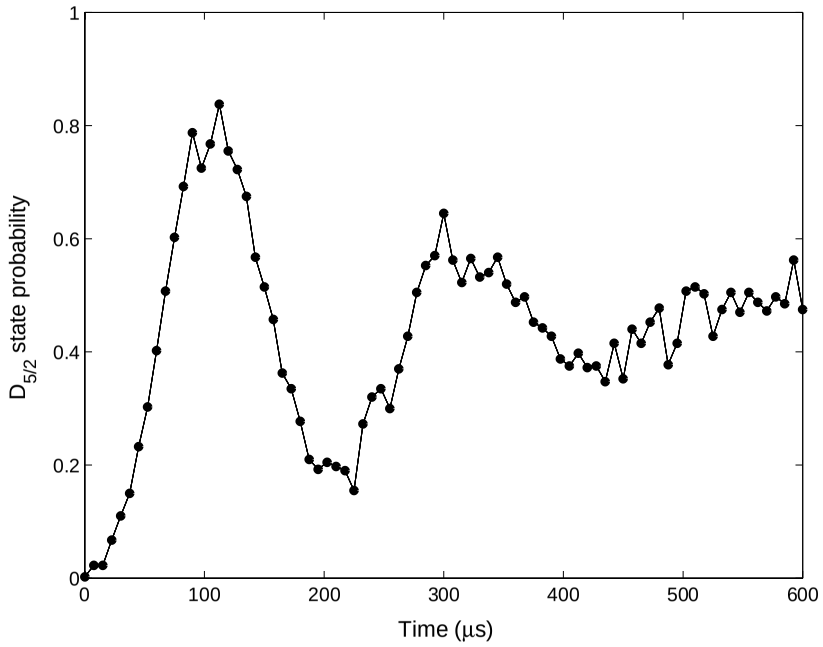

Figure 6.24.: Rabi oscillations of two ions on the upper motional sideband of the axial COM mode after sideband cooling to the ground state.

Fluctuations of the laser intensity

If the Rabi frequency Ω is not constant, but a random variable with standard deviation σ_Ω, then the maximum interaction time T^* is set by the condition $T^* < \pi/\sigma_\Omega$, which is equivalent to $N^* < (\sigma_\Omega/\bar{\Omega})^{-1}/2$, where $N^* = \bar{\Omega}T^*/(2\pi)$ is the maximum number of Rabi oscillations. Fluctuations of the laser intensity I lead to fluctuations of the Rabi frequency, giving $N^* < (\sigma_I/\bar{I})^{-1}$. If more than 30 Rabi oscillations are to be observed, the relative intensity fluctuations σ_I/I have to be smaller than 6%. In the experiments, laser intensity noise occurs mostly at frequencies below 500 Hz so that the Rabi frequency can be assumed to be constant during the laser–ion interaction time but changes randomly from one experiment to the next one. By actively stabilising the laser intensity, its fluctuations can be kept below 5%.

Fluctuations of the magnetic field

Magnetic field fluctuations cause a shift in transition frequencies. As already discussed in subsection 6.1, magnetic field noise mostly occurs at multiples of the power line frequencies. By synchronising the experiment to the phase of the line voltage these contributions can be kept constant. If a suitable phase is chosen, the resonance frequency of the $S_{1/2} \leftrightarrow D_{5/2}$ transition changes by less than 1 kHz within a millisecond. However, there are also other sources of magnetic field noise $\delta B(t)$ that broaden the resonance frequency of the $S_{1/2} \leftrightarrow D_{5/2}$ transition by approximately $\delta_B = 1$ kHz. Since most of the noise occurs at frequencies below

500 Hz, the magnetic field is more or less constant during the excitation pulse, but changes from one realisation of the experiment to the next one. These random detunings do not limit the coherence time in experiments where the coupling strength Ω is significantly higher than δ_B, because the Rabi frequency $X = (\Omega^2 + \delta_B^2)^{1/2} \approx \Omega(1 + \delta_B^2/(2\Omega^2))$ depends only in second order on the detuning δ_B. Therefore, the maximum interaction time is only limited by the condition

$$T^* \ll \left(\frac{2\pi}{\delta_B}\right)\left(\frac{\Omega}{\delta_B}\right) .$$

A more rigid condition holds in experiments where the coupling strength is low or even zero for some time. For example, in the Ramsey resonance experiment described on page 73, the fringe separation is inversely proportional to the interaction time so that fringe contrast washes out as soon as the condition

$$T_{delay} \ll \left(\frac{2\pi}{\delta_B}\right)$$

is violated. Presently, magnetic field fluctuations are not the dominant mechanism that prevents recording of more narrow lines. Otherwise, the minimum linewidth would depend on the Landé factor of the Zeeman component chosen for excitation, which was found not to be the case.

Moreover, it should be possible to reduce magnetic field noise significantly by constructing a μ-metal shield around the vacuum vessel containing the ion trap[5].

Laser linewidth

The laser linewidth γ of the laser at 729 nm limits the coherence time to the inverse of γ. A laser linewidth of better than 100 Hz with respect to the stabilisation cavity was inferred from the error signal of the closed servo loop. Therefore, the laser does not presently limit the coherence time, provided that the frequency stability of the cavity is also less than a kHz[6]. In the future, a second, independent, high-finesse cavity will allow a precise measurement of the laser linewidth.

Unwanted coupling to other atomic levels

If the lasers at 397 and 854 nm are not completely switched off during the quadrupole excitation step, they increase the internal state decoherence rate. For the experiments, less than one photon per 100 ms should be scattered on the $S_{1/2} \leftrightarrow P_{1/2}$ and $D_{5/2} \leftrightarrow P_{3/2}$ transitions.

The quality of the switching at 854 nm can be tested by using the laser at 729 nm to induce quantum jumps at a low rate while the lasers at 397 and 866 nm are switched on. The scattering rate on the $D_{5/2} \leftrightarrow P_{3/2}$ transition is below the threshold defined above if the lengths of the dark periods in the fluorescence are on average longer than 100 ms.

[5] The coils that generate the constant magnetic field have to be placed inside the shield. Care has to be taken that the μ-metal is not saturated by their field.

[6] It was also checked that the transmission of the laser beam through the optical fibre did not significantly broaden the laser linewidth.

The use of two acousto-optical modulators for switching off the light at 397 nm ensures a good suppression of stray light. If the first AOM is switched off (see fig. 4.9), the intensity of the light transmitted through the fibre is reduced by a factor of $5 \cdot 10^5$. The second AOM (cf. fig. 4.8) reduces the power by another factor of $6 \cdot 10^3$ when switched off, so that the overall suppression factor is $3 \cdot 10^9$. In our experiments, the $S_{1/2} \leftrightarrow P_{1/2}$ transition is saturated by 10 μW of light and the photon scattering rate is less than 10^7 photons per 10 μW. Even if 1 mW of blue light was used in the experiments, the stray light level with the AOMs switched off would be below 10^{-12} W so that less than 1 photon per second was scattered on the dipole transition.

Thus, the coherence time is not shortened by these couplings.

Acoustically induced vibrations of the trap electrodes

All coherence limiting processes mentioned so far cannot account for the fact that the narrowest spectral lines observed in the 3D Paul trap have twice the linewidth of the lines observed in the linear trap experiment. However, both experiments differ with respect to trap design. The mechanical setup of the linear trap [85] is undoubtedly more stable than the electrode structure of the 3D trap.

Acoustically induced vibrations of the trap electrodes give rise to two undesired effects. Firstly, they shift the zero-point of the trap potential. Because the trap frequency is much higher than acoustical frequencies, the ion follows this movement adiabatically. However, its rest frame no longer coincides with the rest frame of the laboratory. Secondly, vibrations change the distance between the trap electrodes and consequently alter the trap frequencies.

For a more quantitative analysis, one of the trap electrodes is assumed to vibrate with an amplitude A_0 at a frequency f. The amplitude a_0 of the ionic motion in the direction of the laser beam is proportional to A_0 with $a_0 = sA_0$, $s \leq 1$. For $a(t) = a_0 \cos(2\pi f t)$, the mean velocity spread is given by $\sigma_v = (\langle v(t)^2 \rangle)^{1/2} = \pi f a_0$ so that the first order Doppler effect broadens the line by

$$\sigma_\nu = \sigma_v / \lambda = \frac{\pi f a_0}{\lambda} \, .$$

A linewidth $2\sigma_\nu = 2$ kHz could result from a vibration at 1 kHz with an amplitude $a_0 = 230$ nm.

In order to estimate how much the trap frequency ω is altered, a specific example is considered. The tip electrode separation $2z$ is assumed to change harmonically ($2(z(t) - z_0) = A_0 \cos(2\pi f t)$). Since $\omega \approx q\Omega_{RF}/\sqrt{8}$ and $q \propto 1/(r_0^2 + 2z_0^2)$, the relative change in trap frequency can be expressed as

$$\left| \frac{\Delta\omega}{\omega} \right| = \left| \frac{\Delta q}{q} \right| = \frac{2z_0}{r_0^2 + 2z_0^2} A_0 \, .$$

For a trap frequency $\omega = (2\pi)$ 4 MHz, $r_0 = 0.7$ mm and $z_0 = 0.6$ mm, a vibration amplitude $A_0 = 230$ nm changes the trap frequency by $\Delta\omega = (2\pi)\, 0.5$ kHz. Consequently, the linewidth of the motional sidebands is expected to be broader than the carrier linewidth. Note that the effect becomes more pronounced at higher trap frequencies. For the present setup, the effect is too small to be noticable.

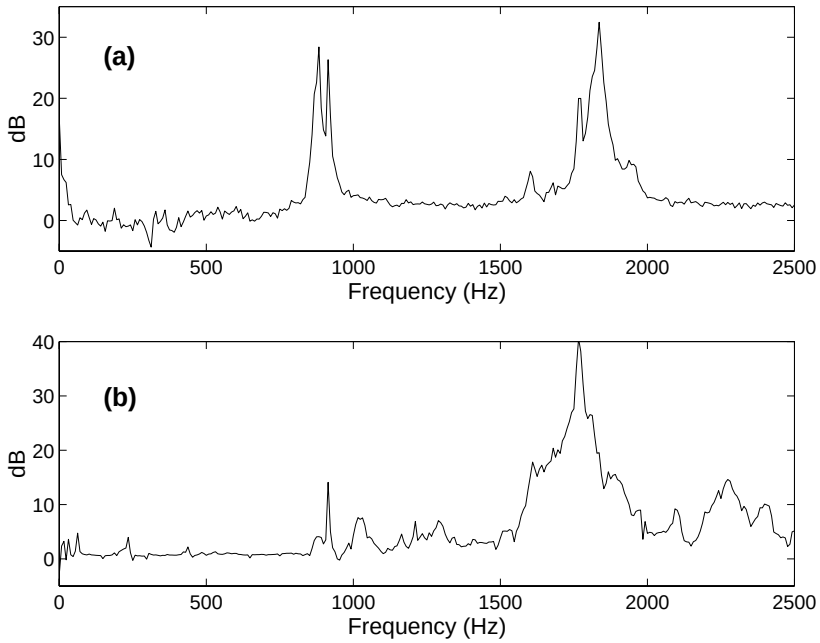

Figure 6.25.: (a) Fourier spectrum of the power back-reflected by the helical resonator. (b) Spectrum of the light intensity of a laser beam focussed to the edge of the ring electrode. Both spectra were recorded with and without additional acoustical excitation of the vacuum vessel. The spectra shown above are the difference spectra of these experiments.

In order to check for vibrations of the trap electrodes, a directional coupler was used to couple out the power back-reflected by the helical resonator. After mixing the signal with the drive frequency Ω_{RF}, a Fourier analysis was performed that showed a narrow resonance at a frequency of 1766 Hz, hinting at a vibration frequency of 883 Hz[7] (see fig. 6.25). Simultaneously, one of the strongly focussed laser beams was misaligned until it started to hit the ring electrode and the transmitted light intensity was monitored. Again, narrow resonances were recorded, the strongest resonance frequencies at 883 Hz and 1836 Hz. The fact that a resonance at 883 Hz is present in both spectra is a strong indication that it is related to vibrations of the trap. However, these experiments do not allow an estimate of the associated vibrational amplitude.

Effects of ion motion

In principle, all decoherence mechanisms discussed so far can be made arbitrarily small, in contrast to effects that are caused by ion motion.

The Rabi frequency depends on the motional state of the ion. If not all of the oscillators are

[7] On resonance of the helical resonator the back reflected power is expected to oscillate at twice the vibration frequency.

cooled to the ground state, a mixture of motional states results and the Rabi frequency will be different for every single experiment. In case of m thermally distributed modes with mean occupancy $\bar{n}_1, \ldots, \bar{n}_m$, the relative fluctuations are given by $\sigma_\Omega/\bar{\Omega} = (\sum_m \eta_m^4 \bar{n}_m(\bar{n}_m + 1))^{1/2}$ [64]. For example, if there is only a single thermally distributed mode that couples to the laser, $\sigma_\Omega/\bar{\Omega} = \eta^2(\bar{n}(\bar{n}+1))^{1/2}$ and the maximum number of Rabi oscillations N^* is limited by $N^* < 1/(2\eta^2\bar{n})$. For $\eta = 0.05$ and $\bar{n} = 10$, $N^* < 20$. It seems to be advantageous to use a tightly confining trap since fluctuations in the coupling strength scale as $\sigma_\Omega/\bar{\Omega} \propto \omega^{-2}$ because of $\eta \propto \omega^{-1/2}$ and $\bar{n} \propto \omega^{-1}$.

Furthermore, as discussed in subsection 6.5.2, the shift of sideband transition frequency caused by differing carrier excitation strengths (Eq. (6.1)) reduces the fidelity of sideband excitation pulses. Again, the effect can be reduced by increasing the trap frequency.

By cooling all motional degrees of freedom to the ground state, the above mentioned effects can be eliminated. While this task is fairly easily accomplished in the case of a single trapped ion, it becomes more and more cumbersome as soon as experiments are extended to two, or even more ions.

Motional heating

Motional decoherence caused by a coupling of the ionic motion to fluctuating external fields presents no obstacle for the experiments described in this thesis. The measured heating rates are orders of magnitude smaller than the observed decoherence rates.

6.7. Improvements of the experimental setup

The experiments described in this chapter can be improved by slightly changing the current setup. Improving the laser sources will enhance the reproducibility of the experiments whereas modifying the trap hopefully leads to an increased coherence time. An extension of the cooling scheme presently employed might help to reduce experimental imperfections.

The above mentioned goals could be achieved by the following measures:

- **Enhanced drift stability of the laser at 397 nm**
  Since the laser at 397 nm needs to have a scanning range of several hundred MHz it is locked to a cavity of variable length which in turn results in the laser having a drift stability inferior to the stability of the other lasers. During the course of the experiments the laser frequency has to be adjusted from time to time in order to maintain good Doppler cooling conditions and a proper discrimination between the $S_{1/2}$ and $D_{5/2}$ states. Because a frequency drift results in a change of the ion's fluorescence rate, the drift compensation could be performed automatically by the computer controlling the experiments. Alternatively, instead of stabilising the laser to the $S_{1/2} \leftrightarrow P_{1/2}$ spectral line of the ion, it could be locked to a stable reference resonator similar to the one used for the laser at 866 nm once experiments on the quadrupole transition are undertaken.

- **Improved drift stability of the Ti:Sa laser at 729 nm**
  Presently, the short-term drift of 5-15 Hz/s of the laser frequency is passively compensated by continuously changing the frequency applied to the double-pass AOM. The

necessary experiments required for measuring the laser frequency and calculating the drift rate could in principle also be automated. Still, it would be better if the drift rate could be reduced by a factor of 5. So far, the origin of the short-term drift is unknown. A change in the ambient temperature of the resonator housing[8] could be coupled to the ULE resonator via blackbody radiation. Also, absorption of laser light coupled into the high-finesse cavity might change the mirror separation. The latter hypothesis could be checked by varying the light power used for the laser stabilisation.

- **Magnetic shielding of the trap**
  Although fluctuations of the magnetic field presently do not seem to limit the maximum coherence time on the quadrupole transition, it is desirable to reduce these fluctuations. Due to the spatial inhomogenity of the magnetic field close to the vacuum vessel containing the trap, it appears to be difficult to actively stabilise the magnetic field at the position of the ion. Therefore, a μ-metal shielding of the trap is required. For practical reasons, the shielding probably has to be put into the vacuum vessel which would in turn require the magnetic field coils to also be installed inside the shielding and the vacuum chamber.

- **More stable mechanical setup of the trap**
  Acoustically induced vibrations of the trap electrodes eventually limit the coherence time. By attaching the trap electrodes to a structure that is mechanically more stable than the wires used in the present setup, it should be possible to reduce the contribution of this source to internal and external state decoherence.

- **Higher trap frequencies**
  The efficiency of Doppler cooling could be improved by performing experiments at higher trap frequencies. The latter could be achieved without changing the stability parameters of the trap by decreasing the overall size of the trap by a factor of 1.5, while simultaneously increasing the RF-drive frequency Ω_{RF} by a similar factor. It appears unlikely that, as a consequence of this modification, the heating rates will rise to an intolerable level.

- **Extended cooling scheme**
  Reducing the mean vibrational quantum number by working at higher trap frequencies will help to reduce unwanted effects of ion motion due to thermally populated modes but it might still not be sufficient, especially in the case of two trapped ions. It appears to be highly desirable to cool all vibrational degrees of freedom to a mean vibrational quantum number close to one, before sideband cooling is used to cool one or several selected modes to the vibrational ground state. A variety of additional cooling steps could possibly improve the cooling results:
  In the present sideband cooling setup, each normal mode to be cooled requires its own frequency generator in order to generate the necessary laser frequency. The number of available frequency generators limits the number of normal modes that can be cooled. Since for the purpose of sideband cooling a frequency source with a frequency stability of

[8] It was observed that the temperature over the laser table increased by as much as 2 °C during the course of the experiments.

several kHz is sufficient, a voltage controlled oscillator (VCO) could be used to generate all the frequencies required for cooling an unlimited number of normal modes by applying a suitable step function to the VCO.
Alternatively, sideband cooling could be done by driving Raman transitions between the $S_{1/2}(m = -1/2)$ and $S_{1/2}(m = +1/2)$ Zeeman ground states. By detuning the laser at 397 nm by a couple of hundred MHz from the $S_{1/2} \leftrightarrow P_{1/2}$ transition, it might be possible to implement a kind of 'dirty' sideband cooling without the need of an additional laser source. This cooling scheme would not allow one to reach the motional ground state, but would aim at cooling several motional modes simultaneously to a sub-Doppler temperature.

7. Cavity quantum electrodynamics with trapped ions

Cavity quantum electrodynamics (cavity QED) [109] describes the radiative properties of atoms which are subject to electro-magnetic fields having boundary conditions other than those of free space. It was realised as early as 1946 that the decay rate of an atomic transition could be altered by modifying the mode density of the electro-magnetic field experienced by the atom [110]. It took more than twenty years before this concept was experimentally verified by measuring the fluorescence decay time of excited dye molecules in a mono-molecular layer which was kept at a known distance from a metal surface [111].

An efficient method of changing the mode density is to place an excited atom in a resonator. If the cavity is not in resonance with the atomic transition and the cavity subtends a large solid angle $\Delta\Omega$ at the atom, thereby preventing it from interacting with a substantial fraction of the modes of free space, then the atomic decay rate is reduced to [112]

$$\gamma_{inh} \approx A(1 - \Delta\Omega/(4\pi)) \ ,$$

where A is the Einstein coefficient for free-space decay. The first demonstration of *atomic* inhibited spontaneous emission was done with Rydberg atoms in a cavity and showed a twentyfold increase in the lifetime of the Rydberg state [113].[1] On the other hand, if the cavity is in resonance with the atomic transition, the decay rate is increased by a factor [110]

$$f = 3Q\lambda^3/(4\pi^2 V) \gg 1 \ ,$$

provided that the quality factor of the cavity $Q = \omega/(2\kappa)$ is high enough and the cavity volume V is small. Enhancement of spontaneous emission was first observed in microwave transitions [115], due to their long transition wavelengths. For optical transitions, the cavity mirrors need to have high reflectivity and the cavity volume has to be very small [116].[2] Enhanced spontaneous emission is accompanied by a change in the spatial emission characteristics. For large enhancement factors, the photons are coupled mainly into the cavity mode and emitted into free space via decay of the cavity field. An entirely new class of phenomena occurs if the coupling g between the atom and the cavity mode becomes larger than both the cavity decay rate κ, and the atomic decay rate γ into modes other than the cavity mode. In this case, the atom is likely to re-absorb a photon previously emitted into the cavity [118]. The resonant exchange of energy gives rise to effects like quantum Rabi oscillations [2], vacuum Rabi splitting [119, 120] and sub-natural linewidth averaging [121].

[1] It had been shown before that the radiative decay of the cyclotron motion of a single electron in a Penning trap (which forms a microwave cavity) was reduced compared to the free-space decay rate [114].

[2] Before mirrors with ultra-high reflectivity became available, enhanced spontaneous emission on an optical transition could be demonstrated by using the mode degeneracy in a confocal resonator [117].

7.1. Theory: Atom–cavity interaction

The dynamics of an atom resonantly interacting with a cavity mode is governed by the coupling constant g between atom and field and by the dissipative coupling rates γ, κ of the atom and the cavity field to the environment (see fig. 7.1). Here, it is assumed that the atomic decay rate γ does not differ considerably from its free-space value. The master equation describing the interaction is given by [122]

$$\dot{\rho} = \frac{1}{i\hbar}[H,\rho] + L\rho\,, \text{ where} \tag{7.1}$$

$$H = i\hbar g(\sigma_- a^\dagger - \sigma_+ a) \tag{7.2}$$

$$L\rho = \gamma_\perp(2\sigma_-\rho\sigma_+ - \sigma_+\sigma_-\rho - \rho\sigma_+\sigma_-) + \kappa(2a\rho a^\dagger - a^\dagger a\rho - \rho a^\dagger a)\,. \tag{7.3}$$

$a^\dagger$, a are the creation and annihilation operators for the cavity field, σ_+, σ_- and σ_z Pauli pseudospin operators for the atom.

The equation (7.2) was derived by Jaynes and Cummings [63] for a system without

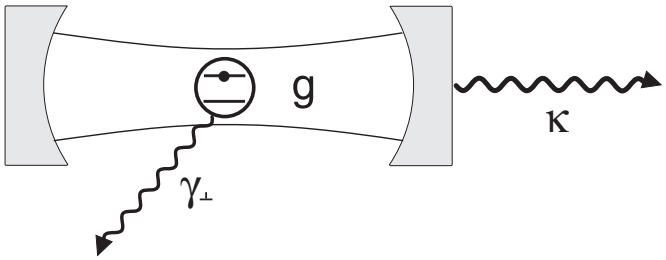

Figure 7.1.: Model system consisting of a two-level atom resonantly coupled to a mode of a cavity with the coupling constant g. κ is the decay rate of the cavity field, γ characterises the atomic decay.

dissipation. The Hamiltonian (7.2) is equivalent to the Hamiltonian (3.15) that describes the excitation of a trapped two-level ion on the lower motional sideband. Equation (7.1) can be solved in the three-state basis $|+\rangle|0\rangle$, $|-\rangle|1\rangle$, $|-\rangle|0\rangle$, where $|+\rangle$ and $|-\rangle$ are the upper and lower atomic states and $|1\rangle$ and $|0\rangle$ are the one-photon and zero-photon Fock states of the field, by transforming it into a set of coupled equations for operator expectation values [122]. For $\langle a\rangle$ and $\langle\sigma_-\rangle$ one obtains

$$\langle\dot{a}\rangle = g\langle\sigma_-\rangle - \kappa\langle a\rangle \tag{7.4}$$

$$\langle\dot{\sigma}_-\rangle = -g\langle a\rangle - \gamma_\perp\langle\sigma_-\rangle\,. \tag{7.5}$$

The eigenvalues

$$\lambda_\pm = -\frac{\kappa+\gamma_\perp}{2} \pm \sqrt{\left(\frac{\kappa-\gamma_\perp}{2}\right)^2 - g^2} \tag{7.6}$$

of eqs. (7.4, 7.5) govern the time evolution of $\langle a \rangle$ and $\langle \sigma_- \rangle$. For weak coupling ($g \ll |\kappa - \gamma_\perp|$), λ_- corresponds to the decay of the cavity field while λ_+ is related to the decay of the atomic polarisation. Two interesting regimes exist:

- *Bad cavity regime* : $\gamma_\perp \ll g^2/\kappa \ll \kappa$
  The eigenvalues take the form

$$\lambda_+ = -\left(\gamma_\perp + \frac{g^2}{\kappa}\right) = \gamma_\perp(1+2C) \tag{7.7}$$

$$\lambda_- = -\left(\kappa - \frac{g^2}{\kappa}\right) , \tag{7.8}$$

  where the *cooperativity parameter* $C = g^2/(2\kappa\gamma_\perp)$ [123] has been used to express the atomic decay rate. Thus, the decay rate of the excited state is notably shortened in the bad cavity limit ($C \gg 1$) compared to its free-space value $\gamma_\parallel$:

$$\gamma_\parallel \longrightarrow \gamma_\parallel(1+2C)$$

  This is the regime where the atom decays predominantly by emitting a photon into the cavity, so that a quasi one-dimensional spontaneous emission pattern arises. The atom–cavity system behaves like a 'one-dimensional atom' [124].

- *Strong coupling regime* : $g \gg \kappa, \gamma_\perp$
  In this regime the eigenvalues are given by

$$\lambda_\pm = -\frac{\kappa+\gamma_\perp}{2} \pm i\frac{\Omega}{2} ,$$

  where the Rabi frequency $\Omega = [4g^2 - (\kappa - \gamma_\perp)^2]^{1/2} \gg (\kappa + \gamma_\perp)$ describes the oscillatory exchange of energy between the cavity field and the atom. In case that $\gamma_\perp \gg \kappa$, the excited state of the atom decays at the reduced rate $\gamma_\perp$ (instead of $2\gamma_\perp$) since half of the excitation is hidden in the cavity field.

Two types of systems have been used to carry out beautiful experiments in the strong coupling regime. On the one hand, experiments have been performed by generating an atomic beam of long-lived Rydberg atoms and sending it through a microwave resonator which is resonant with a transition to another Rydberg state (see for example [2, 125]). On the other hand, experiments were done by sending a slow atomic beam of Cesium [120], Rubidium [126] or Barium [127][3] atoms through an optical high-finesse resonator with a small mode volume.

Still, both realisations of Jaynes-Cummings dynamics suffer from drawbacks. The interaction time is limited to the atomic transit time through the resonator. The coupling $g(\mathbf{r})$ between atom and field is position-dependent and varies in the optical domain on a sub-μm scale. For experiments done with microwave fields, it is not possible to detect the field directly. Therefore, it appears tempting to imagine coupling a *trapped* atom to a mode of an optical high-finesse resonator. One way to accomplish this task is to use a charged atom trapped in an ion trap. Thereby it should be possible to localise the particle on a sub-wavelength scale

[3] Admittedly, in the Ba experiment, the transit time broadening was larger than the coupling constant g.

and to achieve practically indefinite interaction times. However, it quickly becomes clear that reaching the strong coupling regime is exceedingly difficult since it requires building an ion trap around a miniature high-finesse resonator. How to realise the more moderate aim of doing experiments in the bad cavity limit is discussed in the following section.

7.2. Experiment: Design considerations

The difficulty of achieving strong coupling conditions arises from the fact that it is hard to satisfy the condition $g \gg \gamma_\perp$ in case of a dipole transition, while it is difficult to achieve $g \gg \kappa$ in case of a quadrupole transition. This can be understood by noting that the coupling constant g depends linearly on the relevant atomic multipole moment, while the atomic decay rate $\gamma_\perp$ depends quadratically on it. If $g \gg \gamma_\perp$ is to hold on a dipole transition, it requires a cavity with small mode volume V because $g \propto V^{-1/2}$. For experiments performed on optical dipole transitions in the strong coupling regime [120, 126, 128], cavity lengths vary between 10 and several 100 μm. The tasks of constructing an ion trap around such a resonator, or placing it between the mirrors, appear to be equally challenging.

Therefore, one might consider using a quadrupole transition instead, since $g \gg \gamma_\perp$ can be easily satisfied. As far as the strong coupling regime is concerned, this only shifts the difficulties to satisfying the other inequality $g \gg \kappa$. However, experiments become possible in the bad cavity regime as will be shown below.

The calculation of the coupling constant g between the atom and the cavity mode proceeds analogously to the computation of the Rabi frequency in subsection 3.4.3. For an atom at position $\mathbf{r}_0$ interacting with the radiation field $\mathbf{E_T}(\mathbf{r}_0)$ via an electric quadrupole coupling, the Hamiltonian takes the form [59][4]

$$H_{EQ} = \tfrac{1}{2} e(\hat{\mathbf{r}}\nabla)(\hat{\mathbf{r}}\mathbf{E_T}(\mathbf{r}_0)) \; . \tag{7.9}$$

A standing wave in a cavity is described in the paraxial approximation [129] by setting

$$\mathbf{E_T}(\mathbf{r}) = i\boldsymbol{\epsilon}\phi(\mathbf{r})\cos(\mathbf{kr})(ae^{-i\omega t} - a^\dagger e^{i\omega t}) \; , \tag{7.10}$$

where $\boldsymbol{\epsilon}$ describes the polarisation of the field mode and $\phi(\mathbf{r})$ the transverse mode structure. For a Gaussian TEM_{00} mode with waist w_0 in a cavity of length L the transverse profile is given by

$$\phi(\mathbf{r}) = \phi_0 \exp(-\tfrac{\rho^2}{{w_0}^2}) \; .$$

ρ gives the distance from the centre of the cavity mode. The normalisation constant ϕ_0 is determined by the requirement that the mode energy of an n-photon Fock state is

$$\int dV \epsilon_0 \langle n|\mathbf{E}_T\mathbf{E}_T|n\rangle = \hbar\omega(n + \tfrac{1}{2}) \; .$$

[4] The symbol $\hat{\mathbf{r}}$ is used to distinguish the quantum mechanical position operator $\hat{\mathbf{r}}$ of the electron with respect to the atom from the position vector $\mathbf{r}$ describing the atomic position.

One obtains

$$\begin{aligned}\int dV \epsilon_0 \langle n|\mathbf{E}_T\mathbf{E}_T|n\rangle &= \epsilon_0\langle n|aa^\dagger + a^\dagger a|n\rangle {\phi_0}^2 \int dV \cos^2(kz)\exp(-\tfrac{2\rho^2}{{w_0}^2}) \\ &= \epsilon_0(2n+1){\phi_0}^2 L\pi {w_0}^2/4\,,\end{aligned}$$

so that

$$\phi_0 = \sqrt{\frac{2\hbar\omega}{\epsilon_0 L\pi {w_0}^2}}\,.$$

By inserting eq. (7.10) into eq. (7.9) the interaction Hamiltonian is written as

$$H_{EQ} = -ie\phi_0 \sin(\mathbf{kr})(\hat{\mathbf{r}}\boldsymbol{\epsilon})(\hat{\mathbf{r}}\mathbf{k})(ae^{i\omega t} - a^\dagger e^{i\omega t})\,.$$

For a two-level system with lower level $|g\rangle$ and upper level $|e\rangle$, H_{EQ} is put into the form of eq. (7.2) by writing

$$H_{EQ} = i\hbar g(|g\rangle\langle e| + |e\rangle\langle g|)(ae^{i\omega t} - a^\dagger e^{-i\omega t}) \tag{7.11}$$

$$g = \left(\frac{\omega e^2}{2\epsilon_0\hbar\pi {w_0}^2 L}\right)^{1/2} k\langle g|(\hat{\mathbf{r}}\boldsymbol{\epsilon})(\hat{\mathbf{r}}\mathbf{n})|e\rangle \sin(\mathbf{kr})\,, \tag{7.12}$$

with $\mathbf{k} = k\mathbf{n}$ and $|\mathbf{n}| = 1$ and performing the rotating-wave approximation. In order to connect g to measurable quantities, one uses the Wigner-Eckart theorem to separate the geometry-dependent part of the interaction from the irreducible matrix element [130] and expresses the latter by the atomic decay rate (cf. eqs. (3.26) and (3.27)). For the $S_{1/2} \leftrightarrow D_{5/2}$ quadrupole transition of Ca^+ one obtains

$$g = \left[\frac{5c\lambda^2}{2\pi^2\gamma_\perp L {w_0}^2}\right]^{1/2}\gamma_\perp \tag{7.13}$$

for optimum coupling (i.e. in the anti-node of the standing wave and $\boldsymbol{\epsilon}$, $\mathbf{k}$, $\mathbf{B}$ mutually orthogonal to each other). Except for a factor of proportionality, equation (7.13) holds for all atomic transitions. The term in squared brackets compares the atomic radiative volume $V_a \propto \lambda^2 c/\gamma_\perp$ [131] to the cavity mode volume $V_m \propto {w_0}^2 L$.[5] The equation shows further that the only atomic parameter having an influence on the cooperativity $C = g^2/(2\kappa\gamma_\perp)$ is the transition wavelength.

Moreover, the cooperativity parameter is also independent of the cavity length L. By stating the cavity decay rate

$$\kappa = \frac{c\pi}{2LF} \tag{7.14}$$

in terms of the cavity finesse $F = \pi\sqrt{R}/(1-R)$ [129], where R is the reflectivity of the cavity mirrors, the cooperativity parameter is written as

$$C = \frac{5F}{2\pi^3}\left(\frac{\lambda}{w_0}\right)^2\,. \tag{7.15}$$

[5] Thus, the condition $g \approx \gamma_\perp$ is equivalent to $V_a \approx V_m \iff L \approx \frac{c}{\gamma_\perp}\left(\frac{\lambda}{w_0}\right)^2$.

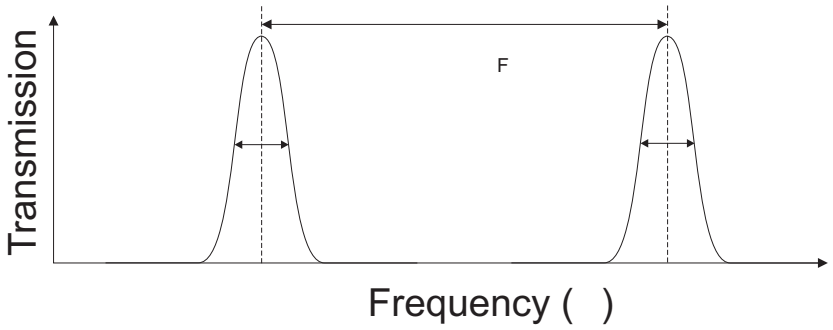

Figure 7.2.: Cavity response as a function of frequency. The frequency width $\delta\omega$ of the transmission maxima is related to the free spectral range $\nu_F = c/(2L)$ and the cavity finesse F by the formula $\delta\omega = 2\pi\nu_F/F$.

Clearly, a high finesse and a small cavity waist w_0 is needed to strongly enhance spontaneous emission. In order to observe this effect, the cavity field frequency ω has to be kept in resonance with the atomic transition frequency. The width of the cavity resonances $\delta\omega$ equals the decay rate of the cavity field intensity so that

$$\delta\omega = 2\kappa = \frac{\pi c}{FL} .$$

For the experiment outlined in the next section, the cavity decay rate κ is small compared with the trap frequency ω_{tr}. Under these conditions, the atomic decay is enhanced only on the carrier transition. (By tuning the cavity to a sideband of the transition, the atom could be similarly caused to emit predominantly on the particular sideband resonant with the cavity. However, the cooperativity parameter would be diminished by a factor of $\eta^2\bar{n}$ in case of the first lower motional sideband and by $\eta^2(\bar{n}+1)$ on the upper motional sideband). If the ion motion is taken into account, the coupling constant g is reduced on the carrier transition by a factor of $1-\eta^2\bar{n}$ for every oscillator mode. For an ion in a state with mean motional quantum number $\bar{n}$, the cooperativity parameter decreases from its value C_0 for an ion at rest to

$$C_0 \to C = C_0(1-2\eta^2\bar{n}) .$$

Thus, the ion has to be cooled to the Lamb-Dicke regime. For similar reasons, the ion's micromotion should be compensated to a degree that the excitation strength on a micromotional sideband is small compared with the carrier.

Finally, the stability of the cavity has to be considered. Both cavity mirrors need to be adjustable with respect to the position of the ion in order to satisfy the resonance condition, as well as the condition for maximum atom-field coupling. Mounting the mirrors on piezoelectric ceramics allows one to move them by applying voltages to the piezos. Fluctuations δU of the piezo voltage U will shift the mirror by an amount[6] δl. The resonator is shifted out

[6]Here, only voltage fluctuations are considered that occur at frequencies below the cut-off frequency set by the electro-mechanical properties of the piezo-mirror system.

of resonance if δl exceeds δl^{max}, defined by

$$\frac{\delta l^{max}}{\lambda/2} = \frac{\delta\omega}{2\pi\nu_F} = \frac{1}{F} ,$$

where $\nu_F = c/(2L)$ is the free spectral range of the resonator. Therefore, the stability of the piezo voltages has to be better than

$$\frac{\delta U}{U} = \frac{\delta l^{max}}{\lambda/2} = \frac{1}{F} ,$$

where U scans the resonator by a free spectral range (see fig. 7.2). Variations of the resonator length also result from changes of the resonator temperature. Given the thermal expansion coefficient α_{th}, the maximum allowable temperature change is

$$\alpha_{th}\delta T^{max} = \frac{\delta l}{L} = \frac{\lambda}{2FL}$$

This formula seems to suggest that cavities of short length L are superior. However, the thermal expansion coefficient of piezo ceramics ($\propto 10^{-5}K^{-1}$) is typically an order of magnitude larger than the thermal coefficient of a low-expansion material like fused silica that could be used as a cavity spacer material. The thermal properties of the cavity are therefore less influenced by the mirror separation L than by the lengths of the piezo crystals.

7.3. Experimental setup and preliminary results

The experiments described below were carried out prior to most of the measurements presented in chapters 5 and 6, and did not lead to the desired results. After a description of the general setup, a report on the experimental problems encountered is given. How to succeed in detecting enhanced spontaneous emission, with an improved setup that is currently being assembled, is described in the next section.

A symmetric resonator is formed by mirrors having a radius of curvature $R_c = 12$ mm. The waist w_0 of the fundamental resonator mode is given by [129]

$$w_0 = (\lambda/\pi)^{1/2} \left(\frac{L}{2} \left(R_c - \frac{L}{2} \right) \right)^{1/4} .$$

For a mirror separation L=20.5 mm and a wavelength $\lambda = 729$ nm, the waist is $w_0 = 31$ μm. Although the atom field coupling, which increases proportionally to ${w_0}^{-1}$, could be made larger by increasing the mirror separation while keeping the mirror curvature fixed, it cannot be increased without bound because the resonator becomes more and more difficult to align. The cavity mode is formed along a line which connects the centres of curvature of the two mirrors. The more the resonator approaches the limiting case of a concentric resonator, the closer these centres move towards each other. Even a small misalignment of the mirrors then causes a large tilt of the cavity axis. Also, the spot size of the cavity mode on the mirrors becomes larger and larger. The mirrors[7] were specified to have a reflectivity of better than

[7] Research Electro-Optics, Boulder, USA.

$R = 0.99997$, corresponding to a cavity finesse $F > 100000$. Measurements of the cavity decay time (see below) revealed that the finesse was actually even much higher. For the measured value $F = 180000$, the cavity decay rate is $\kappa = (2\pi)\ 20$ kHz and an atom field coupling $g = (2\pi)\ 160$ Hz results according to eq. (7.13). Together with the atomic decay

coupling constant	g	=	$(2\pi)\ 160$	Hz
atomic decay rate	$\gamma_\perp$	=	$(2\pi)\ 0.08$	Hz
cavity decay rate	κ	=	$(2\pi)\ 20$	kHz
cooperativity	C	=	8	
trap frequency	ω_{tr}	=	$(2\pi)\ 1-4$	MHz

Table 7.1.: Important experimental parameters

rate $\gamma_\perp = (2\pi)\ 0.08$ Hz on the $S_{1/2} \leftrightarrow D_{5/2}$ transition, the rates g, κ satisfy the criteria for the bad cavity regime and result in a cooperativity parameter $C = 8$, so that a seventeen-fold enhancement (see eq. (7.7)) of the spontaneous decay rate of the $D_{5/2}$ level can be expected if the cavity is in resonance with the quadrupole transition.

The mechanical setup of the resonator is shown in fig. 7.3. A spacer machined out of

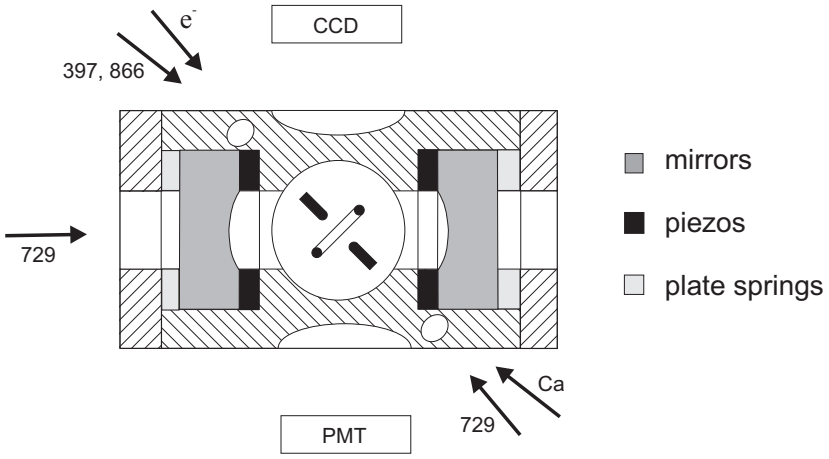

Figure 7.3.: Schematic drawing of the cavity mount. The cavity spacer is a cylindrical piece of fused silica of length 28 mm and diameter 20 mm, with a hole drilled along its symmetry axis. Two larger, blind holes along this axis provide space for the piezo ceramics, cavity mirrors and plate springs. The piezos push the mirrors outwards while the plate springs provide a restoring force. Further drillings allow one to position the ion trap between the mirrors and to collect the ion's fluorescence. Four smaller drillings are needed for sending a Ca beam and an electron beam, as well as different lasers, to the trap. The trap is not drawn to scale with respect to the resonator.

fused silica[8] defines the cavity length. In contrast to the resonator that is rigidly attached to the vacuum vessel, the ion trap is mounted on an electric feedthrough connected to the vacuum vessel by a flexible coupling. Thus, the trap can be positioned in the waist of the resonator from outside the vacuum with the help of adjustment screws. A more detailed description of the mechanical setup is contained in [132]. Both mirrors can be moved with respect to the spacer by ring shaped stacks of piezo ceramics[9], plate springs provide a restoring force. Piezo stacks combine the advantage of high electro-mechanical coupling with compact size. By applying a voltage of 310 V the mirrors are shifted by half a wavelength [132]. The finesse of the cavity was determined by measuring the decay time of the cavity field. For this purpose, the laser at 729 nm was coupled into the resonator and scanned over the resonance of the cavity. As soon as the light intensity transmitted through the cavity exceeded a preset threshold, the laser beam was rapidly switched off, by means of an acousto-optical modulator, so that the decay of the cavity field could be measured by a photodiode (see [132]). For the fundamental TEM_{00} resonator mode, a photon lifetime $\tau = 3.9$ μs was measured, corresponding to a cavity finesse $F = 1.80(5) \cdot 10^5$. Similar measurements for the transverse cavity modes showed that the finesse depended on the particular mode being used. The highest finesse (F=260000) was measured for the TEM_{10} mode while higher-order TEM_{nm} transverse modes ($4 \leq |n| + |m| \leq 8$) had finesse values in the range of 60000-120000 [132]. These variations probably reflect local variations of the mirror reflectivity.

Experimental difficulties encountered

The experimental setup described above proved to be inadequate for observing any cavity QED effects, and experiments towards this aim were abandoned for the present due to the problems listed below:

- **Piezo voltages**
  The piezo voltages of up to 400 V needed for tuning the cavity not only shifted the cavity mirrors but also the ion. Although the piezos were inserted into the cavity spacer with the grounded sides pointing towards the trap in order to screen the electric field generated by the high voltage applied to the other side, the electric field at the position of the ion was big enough to shift the trapped ions by as much as $10-20$ μm, equivalent to changes in the electric field strength of $60-120$ V/m.

- **Compensation of micromotion**
  Contrary to the measurements presented in chapters 5 and 6, the 'static' electric fields at the position of the ion were time-dependent (even if no voltages were applied to the piezos). When keeping the voltages U_{K1}, U_{K2} of the compensation electrodes in the plane of the ring constant, the voltage applied to one of the tips of the trap had to be changed by more than 0.5 V over the course of an hour in order to compensate the micromotion in one direction. It is likely that these changes in the stray electric field are caused by fluctuating charges which are present on the non-conductive parts of the

[8] The spacers were machined in the workshops of the Max-Planck Institut für biophysikalische Chemie, Göttingen, and by Swarovski, Wattens.
[9] HPSt 500/10-5/2, Pickelmann.

cavity spacer (and the mirrors ?). Originally, we had hoped to prevent this effect by coating most of the spacer with a conducting graphite solution[10].

- **Ion storage time**
  The storage time of single Ca^+ ions was typically shorter than 40 minutes, which was probably due to a too high background gas pressure caused by insufficient bakeout of the apparatus. Since the piezo stacks were specified to be bakeable only up to a temperature of 120°C, the apparatus was never heated to temperatures exceeding 110°C, in contrast with the baking procedure ($T_{max} \approx 290°$ C) used for the experiments described in chapters 5 and 6.

- **Drift of the cavity resonance**
  Finally, the resonance frequency of the cavity typically drifted by 2-5 MHz/min, the drift rate increasing ten-fold if the Ca oven or the RF-drive were turned on. Clearly, cavity QED experiments are only possible if the resonator is continuously locked to a frequency stable laser that is not resonant with the $S_{1/2} \leftrightarrow D_{5/2}$ transition.

7.4. Improved setup

The severe limitations imposed by the deleterious effects described above can hopefully be overcome with an improved experimental setup:

- By building a Faraday cage around the ion trap, it should be possible to reduce changes of the static electric field caused by the piezo voltages, or by charges on insulating surfaces, to a tolerable level.

- If the positions of piezos and springs (see fig. 7.3) are interchanged, less compact piezos can be used instead of piezo stacks. Piezo tubes having a Curie temperature of 350°C are available[11] and can be baked out at 200°C. Furthermore, this modification has the additional advantage of an increased separation between piezos and trap.

- The length of the cavity can be kept constant by stabilising the resonator to a diode laser operated at a wavelength of 780 nm which is itself stabilised to the high-finesse resonator of the Ti:Sapphire laser at 729 nm. This stabilisation unit is currently being assembled and tested.

How to detect enhanced spontaneous emission from the $D_{5/2}$ level

In the prospective experiment a single Ca^+ ion will be cooled into the Lamb-Dicke regime (or even to the motional ground state) and prepared either in the $|D_{5/2}, m = +5/2\rangle$ or the $|D_{5/2}, m = -5/2\rangle$ level, which only decay to the $S_{1/2}$ level via a single transition. Lifetime measurements of the excited state, with the cavity on and off resonance with the atomic transition, can be done by means of the electron shelving technique. However, contrary to measurements of the lifetime in free space [82, 133], the fluorescence of the ion cannot be

[10] Aquadag, Acheson Industries.
[11] PIC155, PI Ceramic GmbH

monitored continuously by the laser at 397 nm, because driving the $S_{1/2} \leftrightarrow P_{1/2}$ transition with saturating power would broaden the $S_{1/2} \leftrightarrow D_{5/2}$ transition beyond the width of the cavity resonance. Instead, the laser at 397 nm has to be switched on only after a certain time t^* so that the probability p_{t^*} of the particle still being in the $D_{5/2}$ level after time t^* can be determined by repeating this experiment over and over again. By choosing 100 ms $< t^* <$ 500 ms, it should be possible to detect deviations of the decay rate from its value in free space.

8. Summary and conclusions

The work presented here started with the setup of a new ion trap apparatus, capable of trapping single or few Ca^+ ions. The trap has been shown to reliably store a single ion in the centre of the quadrupole potential over many hours. The quantum state of the ion can be read out with high detection efficiency by means of the electron shelving technique. By Doppler cooling, the ion is localised within a few 10 nm and thus placed in the Lamb-Dicke regime. Furthermore, it has been shown that it is possible to utilise the $S_{1/2} \leftrightarrow D_{5/2}$ quadrupole transition for the purpose of sideband cooling and by this means prepare the ion in a pure quantum state. Starting from the motional ground state of the ion, the feasibility of coherently manipulating the ion's quantum state has been investigated. The internal state decoherence time was found to be of the order of a millisecond, thus allowing quantum state manipulations equivalent to more than forty π-pulses on the first motional sideband. In contrast to previous experiments, motional heating was found to be negligibly small and did not present a limitation to the experiments. First steps towards extending the work to two ions have been successfully undertaken.

While the main purpose of the experiments described in chapter 6 was to investigate the $S_{1/2} \leftrightarrow D_{5/2}$ level pair as a qubit candidate, one of the next goals is certainly to generate an entangled state of two ions. This could be achieved in two different ways. On the one hand, it may be possible to create an entangled state in the present trap by a bichromatic excitation of the ions, with light whose frequencies are near-resonant with the upper and lower motional sideband of the $S_{1/2} \leftrightarrow D_{5/2}$ transition [134–136]. One of the advantages of this particular scheme is that there is no need to individually address the ions, so that the scheme can be applied to ions trapped in a tightly confining trap.

On the other hand, laser addressing of individual ions trapped in a linear ion trap has been demonstrated by our group [44]. Therefore, one immediate goal for the future is to transfer the experimental techniques of chapter 6 to the linear trap and to combine it with the individual addressing of ions in order to create entanglement between ions and to demonstrate a quantum gate.

It might turn out that for a successful demonstration of a quantum gate nearly all motional degrees of freedom have to be cooled to the ground state or at least to mixed states with mean vibrational quantum numbers below the Doppler limit. For this purpose, one has to investigate whether it is feasible to cool all motional degrees of two or more ions by sideband cooling on the $S_{1/2} \leftrightarrow D_{5/2}$ transition or whether new pre-cooling stages have to be used (cf. page 100).

As for the cavity QED experiments, there have been no experimental results so far. The aim of coupling the $S_{1/2} \leftrightarrow D_{5/2}$ quadrupole transition of a Ca^+ ion to the mode of a high-finesse resonator proved to be technically much more involved than expected, and led to the development of an improved experimental setup which is currently being assembled.

With this apparatus, the immediate goal, certainly, is to detect enhanced spontaneous emission (cf. page 112). It might also be possible to detect the photons emitted into the cavity directly and to demonstrate a single photon source. Eventually, a linear trap might be used to trap and couple several ions to the cavity mode in order to observe cooperative effects like super-fluorescence [137].

A. Appendix

A.1. Time evolution of a thermal distribution on the carrier transition

When excited on the carrier transition, an arbitrary state of motion evolves in time and yields an excited state population given by

$$\begin{aligned} \rho_{DD}(t) &= \sum_{n=0}^{\infty} p_n \sin^2(\Omega_{n,n} t) \\ &= \frac{1}{2}(1 - \sum_{n=0}^{\infty} p_n \cos(2\Omega_{n,n} t)) \ , \end{aligned} \tag{A.1}$$

where the Rabi frequency

$$\Omega_{n,n} = \Omega_0 L_n(\eta^2)$$

is proportional to the Laguerre polynomial $L_n(\eta^2) = 1 - \eta^2 n + \frac{1}{4}\eta^4 n(n-1) + \mathcal{O}(\eta^6)$ [138]. p_n is the occupation probability of state $|n\rangle$. For a thermal state distribution this probability is given by [59]

$$p_n = \frac{1}{\bar{n}+1}\left(\frac{\bar{n}}{\bar{n}+1}\right)^n =: \frac{1}{\bar{n}+1} x^n \ .$$

Eq. (A.1) is appropriate for the motion of a particle in a one-dimensional potential. Numerically, the summation can be performed quickly in this case, but the calculation becomes much more time consuming if the Rabi frequency depends on several motional modes. Therefore, an approximate solution to the problem is desired. First, an approximate solution is derived for the one-dimensional case that can subsequently be used to treat the case of multiple modes.

After expanding the Rabi frequency to first order in η^2, the summation in eq. (A.1) can be performed analytically. This approximation is valid as long as $t \ll T^*$, where T^* is defined by

$$2\Omega_0 T^* (\bar{n}\eta^2/2)^2 = 1 \ ,$$

the time interval being equivalent to $N^* = 1/(\pi \bar{n}^2 \eta^4)$ Rabi oscillations. For example, $N^* = 32$ if $\eta = 0.1$ and $\bar{n} = 10$. Then the excited state population is given by

$$\begin{aligned} \rho_{DD}(t) &= \frac{1}{2}(1 - \mathrm{Re}\ Q(t)) \text{ with} \\ Q(t) &= \frac{1}{\bar{n}+1} \sum_n x^n \exp(i2\Omega_0 t(1-\eta^2 n)) \\ &= \frac{1}{\bar{n}+1} \frac{\exp(i2\Omega_0 t)}{1 - x\exp(-i2\Omega_0 t\eta^2)} \ , \end{aligned} \tag{A.2}$$

so that

$$\rho_{DD}(t) = \frac{1}{2}\left(1 - \frac{1}{\bar{n}+1}\frac{\cos(2\Omega_0 t)(1 - x\cos(2\Omega_0 t\eta^2)) + x\sin(2\Omega_0 t)\sin(2\Omega_0 t\eta^2)}{1 + x^2 - 2x\cos(2\Omega_0 t\eta^2)}\right) , \quad \text{(A.3)}$$

where $x = \bar{n}/(\bar{n}+1)$. Fig. A.1 shows that the resulting function faithfully reproduces the exact

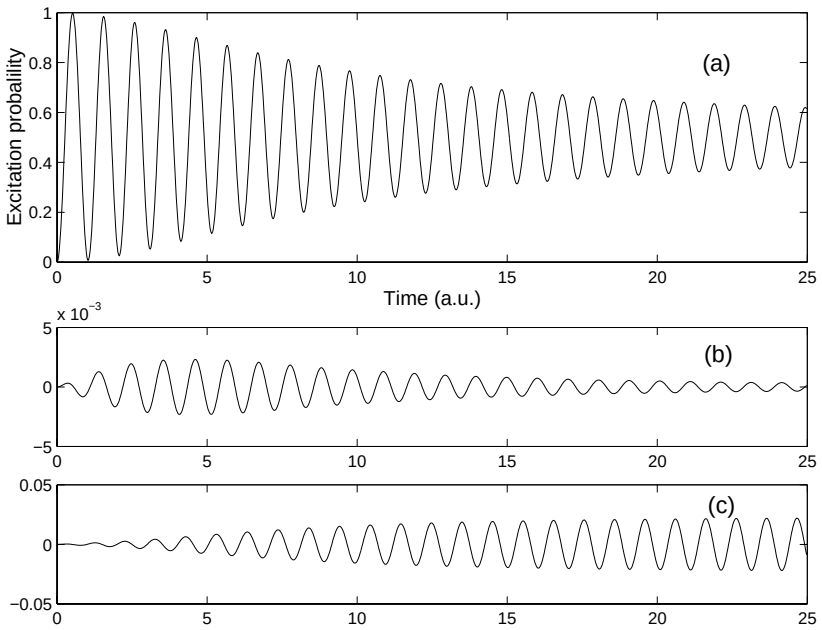

Figure A.1.: Time evolution of a thermal state with $\bar{n} = 10$ on the carrier transition when $\eta = 0.1$. (a) shows the exact solution, (b) and (c) are the differences between the exact solution and the approximations given by eq. (A.3) and (A.5).

result. A further simplification is achieved by approximating $\exp(-i2\Omega_0 t\eta^2) \approx 1 - i2\Omega_0 t\eta^2$ in eq. (A.2) so that $Q(t)$ can now be written as

$$Q(t) = \frac{e^{i2\Omega_0 t}}{1 + i2\Omega_0 t(\eta^2\bar{n})} . \quad \text{(A.4)}$$

For the excited state population, one obtains

$$\rho_{DD}(t) = \frac{1}{2}\left(1 - \frac{\cos(2\Omega_0 t) + (2\Omega t\eta^2\bar{n})\sin(2\Omega_0 t)}{1 + (2\Omega t\eta^2\bar{n})^2}\right) . \quad \text{(A.5)}$$

The approximation is easily extended to the case of several normal modes, all being in a thermal state. Now, the Rabi frequency on the carrier transition depends on all motional quantum numbers $n_1, \ldots, n_m$, and can be written as

$$\Omega_{n_1 \ldots n_m, n_1 \ldots n_m} = \Omega_0 \prod_{j=1}^{m} L_{n_j}({\eta_j}^2) \approx \Omega_0 \prod_{j=1}^{m} (1 - {\eta_j}^2 n_j) .$$

if only terms up to first order in ${\eta_j}^2$ are retained. For the distribution $p(n_1, \ldots, n_N) = \prod_{k=1}^{N} p_k$, where p_k describes the distribution of the kth mode, one obtains by a similar calculation

$$\begin{aligned} Q(t) &= e^{i2\Omega_0 t} \prod_{k=1}^{N} \frac{1}{1 + i2\Omega_0 t(\eta_k^2 \bar{n}_k)} \\ &\approx e^{i2\Omega_0 t} \frac{1}{1 + i2\Omega_0 t \sum_k (\eta_k^2 \bar{n}_k)} \,. \end{aligned}$$

Thus, the final result has the same functional form as eq. (A.5) if the replacement $\eta^2 \bar{n} \to \sum_k (\eta_k^2 \bar{n}_k)$ is made.

A.2. Efficiency of internal state discrimination

The internal state of the ion ($S_{1/2}$ versus $D_{5/2}$) is detected with high efficiency by application of the electron shelving technique. In the following subsection, the efficiency of the detection process is discussed in more detail.

A.2.1. Discrimination between two levels with infinite lifetime

A simple model can be drawn up if the decay of the metastable $D_{5/2}$ level is disregarded. The number of counts detected by the photomultiplier within a time interval τ is a random variable, and will be called s if the ion is in the fluorescing $S_{1/2}$ state, and n if it is in the non-fluorescing $D_{5/2}$ state. A non-zero value of n accounts for stray light that can never be completely avoided in the experiments. The random variables s, n have a Poissonian distribution [139] since only a small fraction of the atomic fluorescence is detected by the photomultiplier tube. Therefore, $\mathrm{Var}(s) = \bar{s}$ and likewise $\mathrm{Var}(n) = \bar{n}$ where $\bar{s}$, $\bar{n}$ denote the mean values of s and n, respectively.

State discrimination is performed by defining a threshold value σ with $\bar{n} < \sigma < \bar{s}$. If the number of counts exceeds σ, the ion is assumed to be in the $S_{1/2}$ state. There are two possible kinds of errors. An error will be called *of type 1*, if the number of counts is larger than σ although the particle is in the 'dark' $D_{5/2}$ state. Conversely, an error *of type 2*, occurs if the number of counts is equal to or below σ, the ion being in the 'bright' $S_{1/2}$ state. A resonable criterion for setting the threshold σ is given by demanding that the likelihood of errors of first and second type is equal:[1]

$$p(n > \sigma) = p(s \leq \sigma) \tag{A.6}$$

If the detection interval τ is sufficiently long, the distributions of n and s are approximately Gaussian (see fig. A.2) so that eq. (A.6) is equivalent to the condition

$$\frac{\sigma - \bar{n}}{\sqrt{\bar{n}}} = \frac{\bar{s} - \sigma}{\sqrt{\bar{s}}} \,, \tag{A.7}$$

[1] This is not the only conceivable criterion. If, for example, the mean quantum number $\langle n \rangle$ of a state with $\bar{n} \ll 1$ is to be determined by absorption measurements on the lower and upper sidebands, then errors of type 1 distort the outcome of the measurement much more than errors of type 2. Thus, it may be advisable to reduce errors of type 1 at the expense of a higher 'type 2'-error rate.

which gives

$$\sigma = \sqrt{\bar{s}\bar{n}}\,. \tag{A.8}$$

Explicitly, the error probability is given by

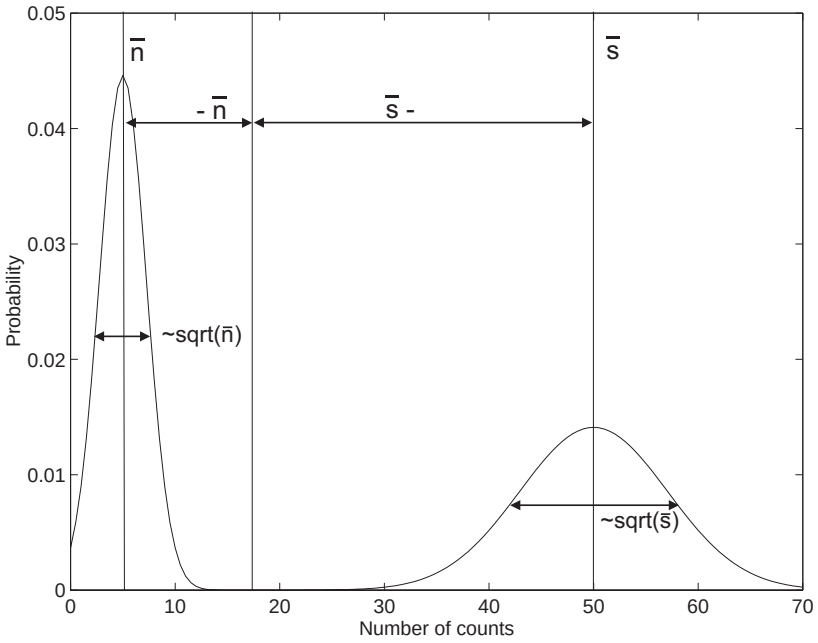

Figure A.2.: A bimodal distribution results if the ion is in a superposition of the $S_{1/2}$ and the $D_{5/2}$ level. In the figure, the distribution is approximated by two Gaussian distributions with $\sigma_n = \sqrt{\bar{n}}$ and $\sigma_s = \sqrt{\bar{s}}$.

$$p(s \leq \sigma) = \frac{1}{2}\left(1 - \mathrm{erf}\left(\frac{\bar{s} - \sigma}{\sqrt{2\bar{s}}}\right)\right)\,, \tag{A.9}$$

where the error function

$$\mathrm{erf}(x) = \frac{1}{\sqrt{2\pi}}\int_{-x}^{x} \exp(-x^2)dx$$

has been used. The error probability can be made arbitrarily small (see fig. A.3) by increasing the length of the detection interval τ since

$$\frac{\bar{s} - \sigma}{\sqrt{\bar{s}}} = \sqrt{\bar{s}}\left(1 - \left(\frac{\bar{s}}{\bar{n}}\right)^{-1/2}\right)\,.$$

If, for example, 50 counts are detected on average in the fluorescing state and the signal to background ratio is 10, then the error probability is made smaller than 10^{-6} by choosing the threshold value $\sigma = \sqrt{(50 \cdot 5)} \approx 16$.

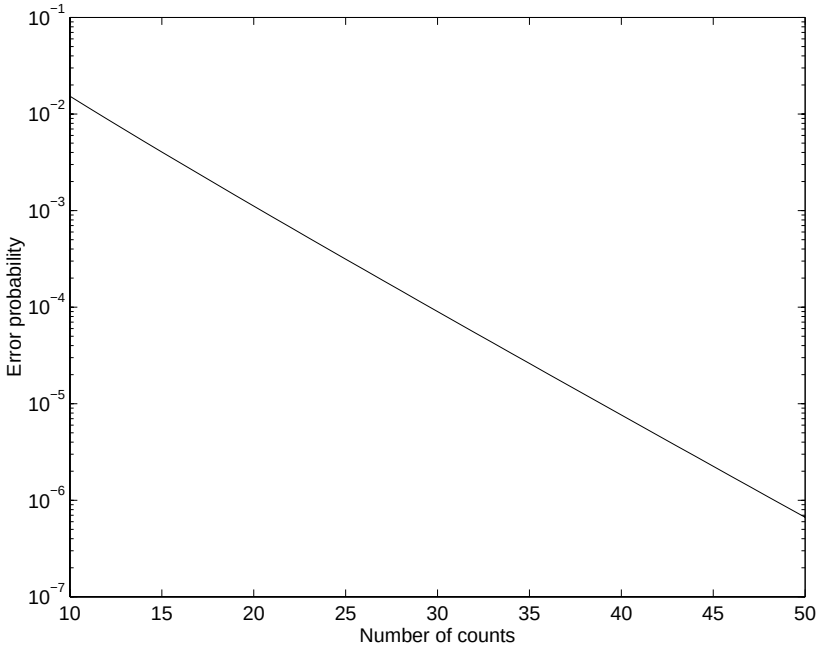

Figure A.3.: The probability of erroneously mistaking one atomic state for the other as calculated from eq. (A.9) decreases rapidly with rising number of counts. The curve has been calculated for a signal to background ratio of 10.

A.2.2. Finite lifetime of the metastable state

The finite lifetime T of the $D_{5/2}$ level imposes a limit on the minimum error probability if the ion is initially in the $D_{5/2}$ level. The probability of the ion having decayed to the $S_{1/2}$ level after a time t is $W(t) = 1 - \exp(-t/T)$. The probability density of the decay occurring at time t^* is given by $w(t^*) = -dW/dt^* = (1/T)\exp(-t^*/T)$, and can be approximated by $w(t^*) \approx 1/T$ for times t^* that are short compared with the lifetime of the $D_{5/2}$ state. Thus, the distribution of counts n (with the ion initially in the $D_{5/2}$ level) is no longer Gaussian, but acquires a long ranging tail towards higher count values (see fig. A.4). It is mainly this tail that will cause errors of type 1. The probability $p(n > \sigma)$ of detecting the ion in the $S_{1/2}$ level, although it was actually in the $D_{5/2}$ level, can be determined by calculating the conditional probability $p(n > \sigma|t)$ that the number of counts n exceeds the threshold σ, provided that the decay to the $S_{1/2}$ level happened at time t, by multiplying this probability with $w(t)$ and integrating over the date of decay:

$$p(n > \sigma) = \int_0^\tau w(t) p(n > \sigma|t)\, dt + p(n_\infty > \sigma) \int_\tau^\infty w(t)\, dt\ , \tag{A.10}$$

where n_∞ denotes the number of counts within $[0, \tau]$ if the lifetime of the $D_{5/2}$ level was infinite. The first part of the right hand side of eq. (A.10) is comprised of events where the decay occurred during the detection time, the second contains the events where the decay

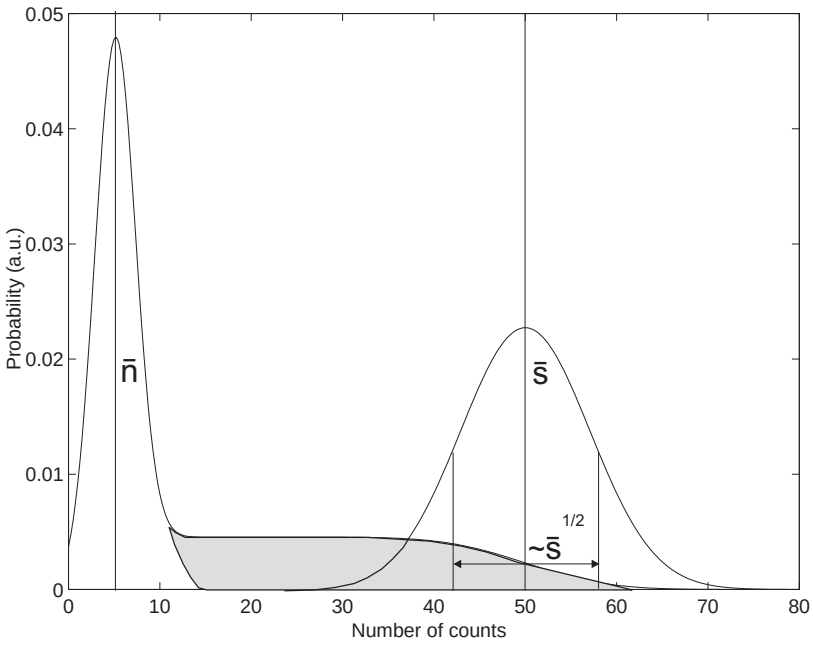

Figure A.4.: Distribution of count numbers if the ion was in the $D_{5/2}$ or the $S_{1/2}$ level at the beginning of the detection interval. The shaded area indicates high count numbers with the ion in the $D_{5/2}$ level that arise from events where the metastable state decays during the detection interval τ. The proportion of these events has been strongly exaggerated in the schematic drawing.

occurred only afterwards. For $\tau \ll T$

$$p(n > \sigma) \approx \frac{1}{T} \int_0^\tau p(n > \sigma|t)\, dt + (1 - \frac{\tau}{T}) p(n_\infty > \sigma)\ . \tag{A.11}$$

For the calculation of $p(n > \sigma|t)$ it is useful to introduce the number of counts n_t if the decay takes place at time $t < \tau$ by writing

$$n_t = n_\infty \frac{t}{\tau} + s \frac{\tau - t}{\tau}\ .$$

n_t has a Gaussian distribution with mean value $\bar{n}_t = \bar{n}_\infty \frac{t}{\tau} + \bar{s} \frac{\tau - t}{\tau}$ since it is the sum of two variables with Gaussian distribution [139]. Although the exact shape of $p(n > \sigma|t) = p(n_t > \sigma)$ as a function of σ can be expressed by using the error function, it suffices for the calculation of eq. (A.11) to replace n and s by their mean values and to approximate $p(n > \sigma|t)$ in this way by

$$p(n > \sigma|t) = \begin{cases} 1 & : \quad t < t_\sigma \\ 0 & : \quad t \geq t_\sigma \end{cases} \quad \text{with } t_\sigma = \tau \frac{\bar{s} - \sigma}{\bar{s} - \bar{n}_\infty}\ .$$

as long as $\bar{s} - \sigma \gg \bar{s}^{1/2}$. Then, eq. (A.11) is simplified to

$$p(n > \sigma) \approx \frac{\tau}{T} \frac{\bar{s} - \sigma}{\bar{s} - \bar{n}_\infty} + p(n_\infty > \sigma) \; . \tag{A.12}$$

The significance of this equation becomes clearer when the scattering rates R_s, R_n for the

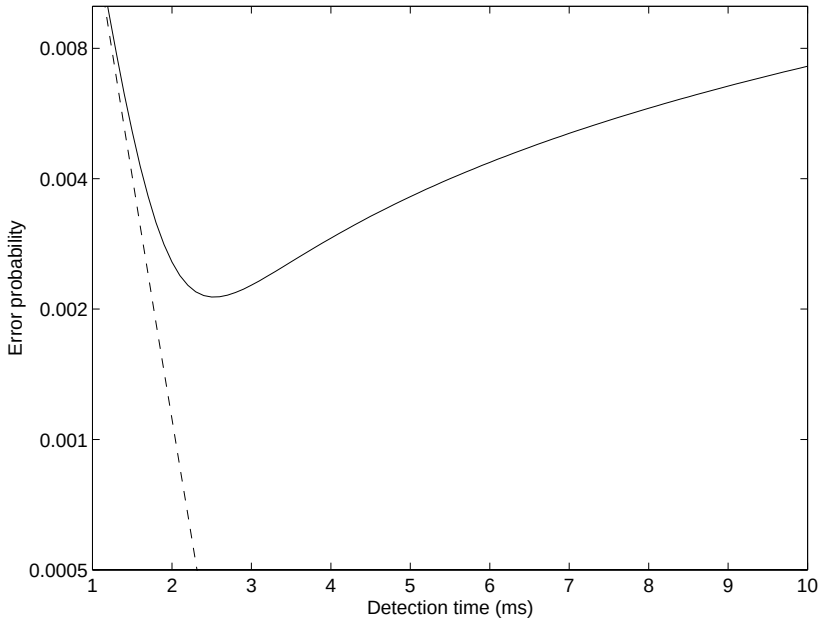

Figure A.5.: Error rates predicted by eq. (A.9) (dashed line) and eq. (A.12) (solid line) if the threshold is chosen to be $\sigma = \sqrt{\bar{s}\bar{n}_\infty}$. The error rates are calculated for a lifetime of the upper state $T = 1.045$ s, a count rate $R = 10$ kHz, and a signal to background ratio of 10. See also fig. A.6.

fluorescing and non-fluorescing state are used to express the number of counts as $\bar{s} = R_s\tau$ and $\bar{n}_\infty = R_n\tau$. When combined with the condition $\bar{s} - \sigma \gg \sqrt{\bar{s}}$, eq. (A.12) imposes a limit on the mimimal error rate

$$p(n > \sigma) \gg \frac{\tau}{T} \frac{\sqrt{\bar{s}}}{\bar{s} - \bar{n}_\infty} = \frac{{R_s}^{1/2}}{T(R_s - R_n)} \sqrt{\tau} + p(n_\infty > \sigma) \tag{A.13}$$

and shows that the type-1 error probability can no longer be decreased without bound by choosing longer and longer detection times τ. However, the dependence on τ is rather weak so that choosing a threshold $\sigma = \sqrt{\bar{s}\bar{n}_\infty}$ instead of the optimum threshold value will not result in a significantly higher error rate. The probability $p(s \leq \sigma)$ of errors of type 2 is the same as in subsection A.2.1.

In order to illustrate the achievable detection efficiency, the situation is analysed for a set of typical parameters. For the ion in the fluorescing state, a count rate $R_s = 10$ kHz is easily achieved as well as a signal to background ratio $R_s/R_n = 10$. In fig. A.5, the eqs. (A.9) and (A.12) are plotted for detection times ranging between 2 and 10 ms and $\sigma = \sqrt{\bar{s}\bar{n}_\infty}$.

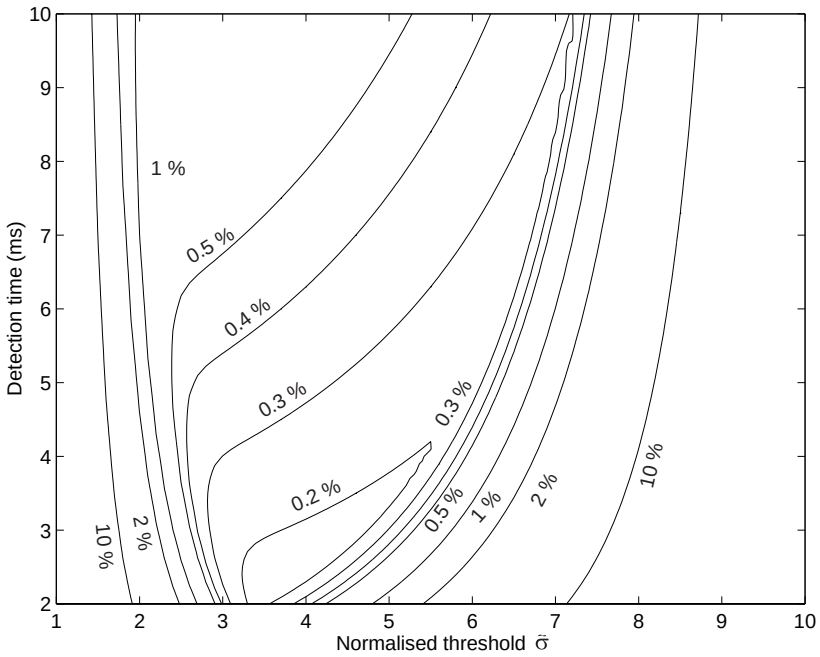

Figure A.6.: Contour plot of the maximum error probability. The error probabilities $p_{type\ 1}$, $p_{type\ 2}$ for errors of the first and second kind are calculated as a function of the threshold σ and the detection time τ. The contour plot shows $\max(p_{type\ 1}, p_{type\ 2})$ plotted against τ, and the normalised threshold $\tilde{\sigma} = \sigma/(R_n\tau)$, for the parameters $T = 1.045$ s, $R_s = 10$ kHz, $R_s/R_n = 10$. The minimum error probability 0.15% is obtained for a detection time close to 3 ms.

Error rates well below 10^{-2} can be achieved for these parameters. Under these conditions, the optimum detection time τ is close to 3 ms. A more complete picture is obtained by calculating the error probabilities $p(n > \sigma)$ (eq.(A.12)) and $p(s < \sigma)$ for errors of the first and second kind as a function of the detection time τ and the threshold σ. Fig. A.6 shows the larger of the two probabilities as a function of τ and σ. The plot exhibits a minimum at the point ($\tau \approx 2.5$ ms, $\tilde{\sigma} = \sigma/(R_n\tau) \approx 3.5$), corresponding to an error probability of 0.15% for errors of the first and second kind. If the intensity of the laser at 397 nm is not stabilised, its fluctuations will broaden the distributions of s, n and shift the optimum detection time towards a slightly longer value.

Bibliography

[1] J. A. Wheeler and W. H. Zurek (editors). *Quantum Theory and Measurement*. Princeton Univ. Pr. (1983).

[2] M. Brune, F. Schmidt-Kaler, A. Maali, J. Dreyer, E. Hagley, J. M. Raimond, and S. Haroche. *Quantum Rabi oscillations: A direct test of field quantization in a cavity*. Phys. Rev. Lett. **76**(11), 1800 (1996).

[3] S. Schiller, G. Breitenbach, S. F. Pereira, T. Müller, and J. Mlynek. *Quantum statistics of the squeezed vacuum by measurement of the density matrix in the number state representation*. Phys. Rev. Lett. **77**(14), 2933 (1996).

[4] T. C. Weinacht, J. Ahn, and P. H. Bucksbaum. *Controlling the shape of a quantum wavefunction*. Nature **397**, 233 (1999).

[5] N. H. Bonadeo, J. Erland, D. Gammon, D. Park, D. S. Katzer, and D. G. Steel. *Coherent optical control of the quantum state of a single quantum dot*. Science **282**, 1473 (1998).

[6] *Special issue: Quantum state preparation and measurement*. J. Mod. Opt. **44**(11/12), 2021 (1997).

[7] A. Einstein, B. Podolsky, and N. Rosen. *Can quantum-mechanical description of physical reality be considered complete ?* Phys. Rev. **47**, 777 (1935).

[8] N. Bohr. *Can quantum-mechanical description of physical reality be considered complete ?* Phys. Rev. **48**, 696 (1935).

[9] S. J. Freedman and J. F. Clauser. *Experimental test of local hidden-variable theories*. Phys. Rev. Lett. **28**(14), 938 (1972).

[10] Q. A. Turchette, C. S. Wood, B. E. King, C. J. Myatt, D. Leibfried, W. M. Itano, C. Monroe, and D. J. Wineland. *Deterministic entanglement of two trapped ions*. Phys. Rev. Lett. **81**(17), 3631 (1998).

[11] C. A. Sackett, D. Kielpinski, B. E. King, C. Langer, V. Meyer, C. J. Myatt, M. Rowe, Q. A. Turchette, W. M. Itano, D. J. Wineland, and C. Monroe. *Entanglement of four particles*. To appear in Nature (2000).

[12] E. Hagley, X. Maitre, G. Nogues, C. Wunderlich, M. Brune, J.M. Raimond, and S. Haroche. *Generation of Einstein-Podolsky-Rosen pairs of atoms*. Phys. Rev. Lett. **79**, 1 (1997).

[13] M. Brune, E. Hagley, J. Dreyer, X. Maître, A. Maali, C. Wunderlich, J.M. Raimond, and S. Haroche. *Observing the progressive decoherence of the meter in a quantum measurement.* Phys. Rev. Lett. **77**, 4887 (1996).

[14] J. F. Poyatos, J. I. Cirac, and P. Zoller. *Quantum reservoir engineering with laser cooled trapped ions.* Phys. Rev. Lett **77**(23), 4728 (1996).

[15] C. J. Myatt, B. E. King, Q. A. Turchette, C. A. Sackett, D. Kielpinski, W. M. Itano, C. Monroe, and D. J. Wineland. *Decoherence of quantum superpositions through coupling to engineered reservoirs.* Nature **403**, 269 (2000).

[16] J. S. Bell. Physics **1**, 195 (1965).

[17] D. M. Greenberger, A. M. Horne, A. Shimony, and A. Zeilinger. *Bell's theorem without inequalities.* Am. J. Phys. **58**, 1131 (1990).

[18] G. Weihs, T. Jennewein, C. Simon, H. Weinfurter, and A. Zeilinger. *Violation of Bell's inequality under strict Einstein locality conditions.* Phys. Rev. Lett. **81**(23), 5039 (1998).

[19] W. M. Itano, J. C. Bergquist, J. J. Bollinger, J. M. Gilligan, D. J. Heinzen, F. L. Moore, M. G. Raizen, and D. J. Wineland. *Quantum projection noise: Population fluctuations in two-level systems.* Phys. Rev. A **47**, 3554 (1993).

[20] J. J. Bollinger, W. M. Itano, D. J. Wineland, and D. J. Heinzen. *Optimal frequency measurements with maximally correlated states.* Phys. Rev. A **54**, R4649 (1996).

[21] A. Steane. *Quantum computing.* Rep. Prog. Phys. **61**, 117 (1998).

[22] P. Shor. *Polynomial-time algorithms for prime factorization and discrete logarithms on a quantum computer.* quant-ph/9508027 (1995).

[23] L. K. Grover. *Quantum mechanics helps in searching for a needle in a haystack.* Phys. Rev. Lett. **79**(2), 325 (1997).

[24] D. P. DiVincenzo. *Two-bit gates are universal for quantum computation.* Phys. Rev. A **51**, 1015 (1995).

[25] T. Sleator and H. Weinfurter. *Realizable universal quantum logic gates.* Phys. Rev. Lett. **74**(20), 4087 (1995).

[26] S. Lloyd. *Almost any quantum logic gate is universal.* Phys. Rev. Lett. **75**(2), 346 (1995).

[27] A. Barenco. *A universal two-bit gate for quantum computation.* Proc. R. Soc. Lond. A **449**, 679 (1995).

[28] D. Deutsch, A. Barenco, and A. Ekert. *Universality in quantum computation.* Proc. R. Soc. Lond. A **449**, 1937 (1995).

[29] P. Knight. *Quantum information processing without entanglement.* Science **287**, 441 (2000).

[30] J. C. Ahn, T. C. Weinacht, and P. H. Bucksbaum. *Information storage and retrieval through quantum phase.* Science **287**, 463 (2000).

[31] C. H. Bennent. *Quantum information and computation.* Phys. Today **48**(10), 24 (1995).

[32] S. J. van Enk, J. I. Cirac, and P. Zoller. *Ideal quantum communication over noisy channels: a quantum optical implementation.* Phys. Rev. Lett. **78**(22), 4293 (1997).

[33] J. I. Cirac, P. Zoller, H. J. Kimble, and H. Mabuchi. *Quantum state transfer and entanglement distribution among distant nodes in a quantum network.* Phys. Rev. Lett. **78**(16), 3221 (1997).

[34] C. Monroe, D. M. Meekhof, B. E. King, W. M. Itano, and D. J. Wineland. *Demonstration of a universal quantum logic gate.* Phys. Rev. Lett. **75**(25), 4714 (1995).

[35] Q. A. Turchette, C. J. Hood, W. Lange, H. Mabuchi, and H. J. Kimble. *Measurement of conditional phase shifts for quantum logic.* Phys. Rev. Lett. **75**(25), 4710 (1995).

[36] A. Rauschenbeutel, G. Nogues, S. Osnaghi, P. Bertet, M. Brune, J. M. Raimond, and S. Haroche. *Coherent operation of a tunable quantum phase gate in cavity QED.* Phys. Rev. Lett. **83**(24), 5166 (1999).

[37] D. G. Cory, A. F. Fahmy, and T. F. Havel. *Nuclear magnetic resonance spectroscopy: an experimentally accessible paradigm for quantum computing.* In *Proceedings of the 4th workshop on physics and computation*, edited by T. Toffoli, M. Biafore, and J. Leão, page 87. New England Complex Systems Institute (1996).

[38] N. A. Gershenfeld and I. L. Chuang. *Bulk spin-resonance quantum computation.* Science **275**, 350 (1997).

[39] W. Dür, J. I. Cirac, and R. Tarrach. *Separability and distillability of multiparticle quantum systems.* Phys. Rev. Lett. **83**(17), 3562 (1999).

[40] S. L. Braunstein, C. M. Caves, R. Jozsa, N. Linden, S. Popescu, and R. Schack. *Separability of very noisy mixed states and implications for NMR quantum computing.* Phys. Rev. Lett. **83**(5), 1054 (1999).

[41] J. I. Cirac and P. Zoller. *Quantum computation with cold trapped ions.* Phys. Rev. Lett. **74**(20), 4091 (1995).

[42] J. D. Prestage, G. J. Dick, and L. Maleki. *New ion trap for frequency standard applications.* J. Appl. Phys. **66**(3), 1013 (1989).

[43] D. Leibfried, D. M. Meekhof, C. Monroe, B. E. King, W. M. Itano, and D. J. Wineland. *Experimental preparation and measurement of quantum states of motion of a trapped atom.* J. Mod. Opt. **44**(11/12), 2485 (1997).

[44] H. C. Nägerl, D. Leibfried, H. Rohde, G. Thalhammer, J. Eschner, F. Schmidt-Kaler, and R. Blatt. *Laser addressing of individual ions in a linear ion trap.* Phys. Rev. A **60**(1), 145 (1999).

[45] T. Pellizari, S. A. Gardiner, J. I. Cirac, and P. Zoller. *Decoherence, continuous observation, and quantum computing: a cavity QED model.* Phys. Rev. Lett. **75**(21), 3788 (1995).

[46] W. Paul. *Quadrupole mass filter.* Z. Naturforsch. **A8**, 448 (1953).

[47] H. Shelton and R. F. Wuerker. *Electrodynamic containment of charged particles.* Bull. Am. Phys. Soc. Ser. **2**, 375 (1957).

[48] W. Paul, O. Osberghaus, and E. Fischer. *Ein Ionenkäfig.* Forschungsberichte des Wirtschafts- und Verkehrsministeriums Nordrhein-Westfalen 415, Westfälischer Verlag (1958).

[49] A. de Marchi (editor). *Frequency standards and metrology.* Springer Verlag (1989).

[50] P. K. Ghosh. *Ion traps.* Clarendon Press (1995).

[51] M. Combescure. *A quantum particle in a quadrupole radiofrequency trap.* Ann. Inst. Henri Poincaré **44**(3), 293 (1986).

[52] L. S. Brown. *Quantum motion in a Paul trap.* Phys. Rev. Lett. (1991).

[53] D. Berkeland, J. D. Miller, J. C. Bergquist, W. M. Itano, and D. J. Wineland. *Minimization of ion micromotion in a Paul trap.* J. Appl. Phys. **83**, 5025 (1998).

[54] R. F. Wuerker, H. Shelton, and R. V. Langmuir. *Electrodynamic containment of charged particles.* J. Appl. Phys. **30**, 342 (1959).

[55] D. J. Wineland, J. C. Bergquist, W. M. Itano, J. J. Bollinger, and C. H. Manney. *Atomic ion coulomb clusters in an ion trap.* Phys. Rev. Lett **59**, 2953 (1987).

[56] F. Diedrich, E. Peik, J. M. Chen, W. Quint, and H. Walther. *Observation of a phase transition of stored laser-cooled ions.* Phys. Rev. Lett. **59**, 2931 (1987).

[57] D. F. V. James. *Quantum dynamics of cold trapped ions with application to quantum computation.* Appl. Phys. B **66**, 181 (1998).

[58] C. A. Blockley, D. F. Walls, and H. Risken. *Quantum collapses and revivals in a quantized trap.* Europhys. Lett. **17**, 509 (1992).

[59] R. Loudon. *The quantum theory of light.* Oxford University Press, second edition (1983).

[60] D. M. Meekhof, C. Monroe, B. E. King, W. M. Itano, and D. J. Wineland. *Generation of nonclassical motional states of a trapped atom.* Phys. Rev. Lett. **76**, 1796 (1996).

[61] K. E. Cahill and R. J. Glauber. *Ordered expansions in boson operators.* Phys. Rev. **177**, 1857 (1969).

[62] A. Galindo and P. Pascual. *Quantum mechanics I.* Springer-Verlag (1990).

[63] E. T. Jaynes and F. W. Cummings. Proc. IEEE **51**, 89 (1963).

[64] D. J. Wineland, C. Monroe, W. M. Itano, D. Leibfried, B. E. King, and D. M. Meekhof. *Experimental issues in coherent quantum-state manipulation of trapped atomic ions*. J. Res. Natl. Inst. Stand. Technol. **103**, 259 (1998).

[65] C. Monroe, D. M. Meekhof, B. E. King, S. R. Jefferts, W. M. Itano, D. J. Wineland, and P. Gould. *Resolved-sideband Raman cooling of a bound atom to the 3D zero-point energy*. Phys. Rev. Lett **75**, 4011 (1995).

[66] D. Stevens, J. Brochard, and A. M. Steane. *Simple experimental methods for trapped-ion quantum processors*. Phys. Rev. A **58**(4), 2750 (1998).

[67] T. W. Hänsch and A. L. Schawlow. *Cooling of gases by laser radiation*. Opt. Comm. **13**(1), 68 (1975).

[68] D. J. Wineland and H. G. Dehmelt. Bull. Am. Soc. **20**, 637 (1975).

[69] C. Cohen-Tannoudji. *Atomic motion in laser light*. In *Fundamental systems in quantum optics*, Les Houches, Session LIII. Elsevier Science Publishers (1990).

[70] S. Stenholm. *The semiclassical theory of laser cooling*. Rev. Mod. Phys. **58**(3), 699 (1986).

[71] H. Risken. *The Fokker-Planck equation : Methods of solution and applications*, volume 18 of *Springer series in synergetics*. Springer, second edition (1989).

[72] G. Morigi, J. I. Cirac, M. Lewenstein, and P. Zoller. *Ground state laser cooling beyond the Lamb-Dicke limit*. Europhys. Lett. **23**(1), 1 (1997).

[73] D. J. Wineland and W. M. Itano. *Laser cooling of atoms*. Phys. Rev. A **20**(4), 1521 (1979).

[74] J. I. Cirac, R. Blatt, P. Zoller, and W. D. Phillips. *Laser cooling of trapped ions in a standing wave*. Phys. Rev. A **46**(5), 2668 (1992).

[75] F. Diedrich, J. C. Bergquist, W. M. Itano, and D. J. Wineland. *Laser cooling to the zero-point energy of motion*. Phys. Rev. Lett. **62**(4), 403 (1989).

[76] I. Marzoli, J. I. Cirac, R. Blatt, and P. Zoller. *Laser cooling of trapped three-level ions: Designing two-level systems for sideband cooling*. Phys. Rev. A **49**(4), 2771 (1994).

[77] S. E. Hamann, D. L. Haycock, P.H. Pax, I. H. Deutsch, and P. S. Jessen. *Resolved-sideband Raman cooling to the ground state of an optical lattice*. Phys. Rev. Lett. **80**(19), 4149 (1998).

[78] H. Perrin, A. Kuhn, I. Bouchoule, and C. Salomon. *Sideband cooling of neutral atoms in a far-detuned optical lattice*. Europhys. Lett. **42**(4), 395 (1998).

[79] V. Vuletić, C. Chin, A. J. Kerman, and S. Chu. *Degenerate Raman cooling of trapped cesium atoms at very high atomic densities*. Phys. Rev. Lett. **81**(26), 5768 (1998).

[80] E. Peik, J. Abel, Th. Becker, J. von Zanthier, and H. Walther. *Sideband cooling of ions in radiofrequency traps*. Phys. Rev. A **60**(1), 439 (1999).

[81] S. A. Gardiner, J. I. Cirac, and P. Zoller. *Nonclassical states and measurement of general motional observables of a trapped ion*. Phys. Rev. A **55**(3), 1683 (1997).

[82] M. Block, P. Seibert, O. Rehm, and G. Werth. *$3D_{5/2}$ lifetime in laser cooled Ca^+: Influence of cooling laser power*. Eur. Phys. J. D **7**(3), 461 (1999).

[83] C. Cohen-Tannoudji, B. Diu, and F. Laloë. *Quantum mechanics*, volume 2. John Wiley & sons (1977).

[84] S. Liaw. *Ab initio calculations of the lifetimes of 4p and 3d levels of Ca^+*. Phys. Rev. A **51**(3), R1723 (1995).

[85] H. C. Nägerl. *Ion strings for quantum computation*. Ph.D. thesis, Universität Innsbruck (1998).

[86] W. W. Macalpine and R. O. Schildknecht. *Coaxial resonators with helical inner conductor*. Proc. IRE **47**, 2099 (1959).

[87] 'Besser jetzt als später'. *R. Blatt*. Private communication (1996).

[88] G. C. Bjorklund. *Frequency-modulation spectroscopy: a new method for measuring weak absorptions and dispersions*. Opt. Lett. **5**(1), 15 (1980).

[89] R. W. Drever, J. L. Hall, F. V. Kowalski, J. Hough, G. M. Ford, A. Munley, and H. Ward. *Laser phase and frequency stabilization using an optical resonator*. Appl. Phys. B **31**, 97 (1983).

[90] T. W. Hänsch and B. Couillaud. *Laser frequency stabilization by polarization spectroscopy of a reflecting reference cavity*. Opt. Comm. **35**(3), 441 (1980).

[91] W. Bechter. *Frequenzstabilisierung eines Diodenlasers bei 866 nm zur Spektroskopie an Ca^+ Ionen*. Diplomarbeit, Universität Innsbruck (1998).

[92] G. Thalhammer. *Frequenzstabilierung von Diodenlasern bei 850, 854 und 866 nm mit Linienbreiten im Kilohertz-Bereich*. Diplomarbeit, Universität Innsbruck (1999).

[93] C. E. Wieman and L. Hollberg. *Using diode lasers for atomic physics*. Rev. Sci. Instr. **62**, 1 (1991).

[94] L. Ricci, M. Weidemüller, T. Esslinger, A. Hemmerich, C. Zimmermann, V. Vuletic, W. König, and T. W. Hänsch. *A compact grating-stabilized diode laser system for atomic physics*. Opt. Comm. **117**, 541 (1995).

[95] G. Blasbichler. *λ-Meter mit 10^{-7} Genauigkeit*. Diplomarbeit, Universität Innsbruck (2000).

[96] H. G. Dehmelt. *Radiofrequency spectroscopy of stored ions I: Storage*. Advan. At. Mol. Phys. **3**, 53 (1967).

[97] T. E. Gudjons. *Laserpräparierte $^{40}Ca^{+}$ Ionen in einer Paul-Falle für Präzisionsspektroskopie: Nichtlineare Dynamik, Laserkühlen und 'electron shelving'.* Ph.D. thesis, Universität Mainz (1996).

[98] L. D. Landau and E. M. Lifschitz. *Mechanik.* Akademie-Verlag Berlin (1962).

[99] R. G. DeVoe, J. Hoffnagle, and R. G. Brewer. *Role of laser damping in trapped ion crystals.* Phys. Rev. A **39**(9), 4362 (1989).

[100] R. Blümel, C. Kappler, W. Quint, and H. Walther. *Chaos and order of laser-cooled ions in a Paul trap.* Phys. Rev. A **40**(2), 808 (1989).

[101] H. Oberst. *Resonance fluorescence of single barium atoms.* Diplomarbeit, Universität Innsbruck (1999).

[102] N. F. Ramsey. *Molecular beams.* Clarendon, second edition (1989).

[103] Q. A. Turchette, D. Kielpinski, B. E. King, D. Leibfried, D. M. Meekhof, C. J. Myatt, M. A. Rowe, C. A. Sackett, C. S. Wood, W. M. Itano, C. Monroe, and D. J. Wineland. *Heating of trapped ions from the quantum ground state.* quant-ph/0002040 (2000).

[104] B. Appasamy, I. Siemers, J. Eschner, R. Blatt, W. Neuhauser, and P. E. Toschek. *Quantized infrared-optical triple resonance on a single cold barium ion.* Appl. Phys. B **60**, 473 (1995).

[105] S. K. Lamoreaux. *Thermalization of trapped ions: A quantum perturbation approach.* Phys. Rev. A **56**(6), 4970 (1997).

[106] D. F. V. James. *Theory of heating of the quantum ground state of trapped ions.* Phys. Rev. Lett. **81**(2), 317 (1998).

[107] S. Schneider and G. J. Milburn. *Decoherence and fidelity in ion traps with fluctuating trap parameters.* Phys. Rev. A **59**(5), 3766 (1999).

[108] C. Henkel and M. Wilkens. *Heating of trapped atoms near thermal surfaces.* Europhys. Lett. **47**(4), 414 (1999).

[109] P. R. Berman. *Cavity quantum electrodynamics.* Advances in atomic, molecular and optical physics, supplement 2. Academic Press (1994).

[110] E. M. Purcell. *Spontaneous emission probabilities at radio frequencies.* Phys. Rev. **69**, 681 (1946).

[111] K. H. Drexhage. *Variation of the fluorescence decay time of a molecule in front of a mirror.* Berichte der Bunsengesellschaft für physikalische Chemie **72**(2), 329 (1968).

[112] P. Stehle. *Atomic radiation in a cavity.* Phys. Rev. A **2**(1), 102 (1970).

[113] R. G. Hulet, E. S. Hilfer, and D. Kleppner. *Inhibited spontaneous emission by a Rydberg atom.* Phys. Rev. Lett. **55**(20), 2137 (1985).

[114] G. Gabrielse. *Observation of inhibited spontaneous emission.* Phys. Rev. Lett. **55**(1), 67 (1985).

[115] P. Goy, J. M. Raymond, M. Gross, and S. Haroche. *Observation of cavity-enhanced single-atom spontaneous emission.* Phys. Rev. Lett. **50**(24), 1903 (1983).

[116] F. De Martini, G. Innocenti, G. R. Jacobovitz, and P. Martini. *Anomalous spontaneous emission time in a microscopic optical cavity.* Phys. Rev. Lett. **59**(26), 2955 (1987).

[117] D. J. Heinzen, J. J. Childs, J. E. Thomas, and M. S. Feld. *Enhanced and inhibited visible spontaneous emission by atoms in a confocal resonator.* Phys. Rev. Lett. **58**(13), 1320 (1987).

[118] D. Meschede, H. Walther, and G. Müller. *One-atom maser.* Phys. Rev. Lett. **54**(6), 551 (1985).

[119] J. J. Sanchez-Mondragon, N. B. Narozhny, and J. H. Ebery. *Theory of spontaneous-emission line shape in an ideal cavity.* Phys. Rev. Lett. **51**(7), 482 (1983).

[120] R. J. Thompson, G. Rempe, and H. J. Kimble. *Observation of normal-mode splitting for an atom in an optical cavity.* Phys. Rev. Lett. **68**(8), 1132 (1992).

[121] M. G. Raizen, R. J. Thompson, R. J. Brecha, H. J. Kimble, and H. J. Carmichael. *Normal-mode splitting and linewidth averaging for two-state atoms in an optical cavity.* Phys. Rev. Lett. **63**(3), 240 (1989).

[122] H. J. Carmichael, R. J. Brecha, M. G. Raizen, H. J. Kimble, and P. R. Rice. *Subnatural linewidth averaging for coupled atomic and cavity-mode oscillators.* Phys. Rev. A **40**(10), 5515 (1989).

[123] L. A. Lugiato. *Theory of optical bistability.* Prog. Opt. **21**, 71 (1984).

[124] Q. A. Turchette, R. J. Thompson, and H. J. Kimble. *One-dimensional atoms.* Appl. Phys. B **60**, 1 (1995).

[125] G. Rempe, H. Walther, and N. Klein. *Observation of quantum collapse and revival in a one-atom maser.* Phys. Rev. Lett. **58**(4), 353 (1987).

[126] P. Münstermann, T. Fischer, P. Maunz, P. W. H. Pinske, and G. Rempe. *Dynamics of single-atom motion observed in a high-finesse cavity.* Phys. Rev. Lett. **82**(19), 3791 (1999).

[127] K. An, J. J. Childs, R. R. Dasari, and M. S. Feld. *Microlaser: A laser with one atom in an optical resonator.* Phys. Rev. Lett. **73**(25), 3375 (1994).

[128] C. J. Hood, M. S. Chapman, T. W. Lynn, and H. J. Kimble. *Real-time cavity QED with single atoms.* Phys. Rev. Lett. **80**(19), 4157 (1990).

[129] B. E. A. Saleh and M. C. Teich. *Fundamentals of photonics.* John Wiley & sons (1991).

[130] R. D. Cowan. *The theory of atomic structure and spectra*. University of California Press (1981).

[131] H. J. Kimble. *Structure and dynamics in cavity quantum electrodynamics*. In *Cavity quantum electrodynamics*, edited by P. R. Berman. Academic Press (1994).

[132] T. Zeiger. *Charakterisierung eines Hochfinesseresonators und Spektroskopie an einem Ca^+ Ion*. Diplomarbeit, Universität Innsbruck (1999).

[133] S. Urabe, M. Watanabe, H. Imajo, and H. Hayasaka. *Laser cooling of trapped Ca^+ and measurement of the $3^2D_{5/2}$ state lifetime*. Opt. Lett. **17**(16), 1140 (1992).

[134] A. Sørensen and K. Mølmer. *Quantum computation with ions in thermal motion*. Phys. Rev. Lett. **82**(9), 1971 (1999).

[135] K. Mølmer and A. Sørensen. *Multiparticle entanglement of hot trapped ions*. Phys. Rev. Lett. **82**(9), 1835 (1999).

[136] A. Sørensen and K. Mølmer. *Entanglement and quantum computation with ions in thermal motion*. quant-ph/0002024 (2000).

[137] R. Bonifacio and L. A. Lugiato. *Cooperative radiation processes in two-level atoms: Superfluorescence*. Phys. Rev. A **11**(5), 1507 (1976).

[138] I. S. Gradshteyn and I. M. Ryzhik. *Table of integrals, series and products*. Acad. Press, fifth edition (1994).

[139] U. Krengel. *Einführung in die Wahrscheinlichkeitstheorie und Statistik*. Vieweg Verlag, third edition (1991).

Die in dieser Arbeit beschriebenen Experimente sind Teil einer gemeinschaftlichen Anstrengung vieler, die mit ihrem Einsatz und ihrer Geduld nicht nur zum Gelingen dieser Arbeit beigetragen, sondern sie vielmehr erst möglich gemacht haben. Ihnen allen will ich an dieser Stelle Dank sagen.

An erster Stelle möchte ich mich bei Rainer Blatt herzlich dafür bedanken, daß er mir durch die Aufnahme in seine Arbeitsgruppe und durch die Themenstellung ermöglichte, in einem anregenden Arbeitsumfeld an einem interessanten Thema zu arbeiten. Sein Interesse und sein unbeirrbarer Optimismus haben mich in allen Phasen meiner Arbeit begleitet. Überdies gebührt ihm mein Dank für seine Kulanz, mich eine Dissertation verfertigen zu lassen, in der das Wort *Dunkelresonanz* erst in der Danksagung Erwähnung findet.

Den Einstieg in die experimentelle Arbeit im Labor hat mir Ferdinand erleichtert, von dem ich in den folgenden Jahren viel habe lernen können. Die in dieser Arbeit beschriebenen Experimente profitierten sehr von der Pionierrolle Hanns-Christophs, der mit seiner Arbeit an der linearen Falle wichtige Voraussetzungen für alle wesentlichen Teile der Ionenfallen--Experimente geschaffen hat. Lange Meßabende habe ich mit Thomas, Ferdi, Didi und Andreas verbracht, deren Aufmerksamkeit in Momenten, in denen mir die Augen zufielen, größere Pannen vermeiden half. Harald hat sich um die Frequenzstabilisierung des Ti:Sa-Lasers zur Quadrupolanregung verdient gemacht, Wolfgang und Gregor die Diodenlaser aufgebaut. Achim verdanke ich nützliche Hinweise zum Ionenfallenbau, Matthias eine Erweiterung meiner Kenntnisse des richtigen Gebrauchs von Werkzeugen.

In der mechanischen Werkstatt haben Stefan und Toni haben viele windige technische Zeichnungen und hochfliegende Konstruktionspläne in reale und funktionsfähige Werkstücke umgewandelt. Herrn Sauermann vom MPI für biophysikalische Chemie in Göttingen und den Mitarbeitern der Firma Swarovski in Wattens danke ich für die Bearbeitung der Quarzabstandshalter für die Resonatorexperimente.

In Jürgen fand ich stets einen geduldigen und aufmerksamen Gesprächspartner, wenn es um die Diskussion physikalischer Probleme ging. Didi und Paul haben durch gründliches Korrekturlesen mir geholfen, die Anzahl fachlicher und sprachlicher Fehler in dieser Arbeit zu verringern.

Auch für Nichtfachliches will ich mich bedanken. Christoph und Hanns-Christoph haben mich davon überzeugt, daß es möglich ist, mit Mitgliedern der eigenen Arbeitsgruppe eine Wohnung zu teilen, ohne daran irre zu werden. Die Instituts-Kochgruppe hat mich mittags mit Essen wie auch Gesprächsstoff versorgt und vor dem Gang in die Mensa bewahrt. Andi, Stephan und Didi haben meine Kenntnisse des schwäbischen Idioms bereichert. Georges und Harald haben geholfen, mich davon zu überzeugen, einen Skikurs zu belegen, und mich anschließend oft begleitet. Ebenso danke ich allen anderen, die ihre Freizeit mit mir geteilt haben. Und schließlich will ich all jenen danken, die mir verzeihen, hier nicht vertreten zu sein, obwohl sie fühlen, darauf ein Anrecht zu haben.